Computational Atomic Physics for Kilonova Ejecta and Astrophysical Plasmas

by

Zahra Taghadomi

(Under the Direction of Phillip C Stancil)

Abstract

Most estimates of chemical composition come from the quantitative analysis and interpretation of spectra, frequently of emitting plasmas that are at extremely low density by laboratory standards. Spectral simulations of these plasmas must rely on a vast database of basic atomic and molecular cross sections and transition rates.

Studying the spectral lines from astrophysical plasmas is more challenging in environments like kilonova ejecta where heavy elements are being produced through the rapid neutron capture process or r-process. Since properties of the emission are largely affected by opacities of the ejected material, enhancements in the available r-process data is important for neutron star merger modeling. However, given the complexity of the electronic structure of these heavy elements, considerable efforts are still needed to converge to a reliable set of atomic structure data. The aim of this work is to alleviate this situation for low charge state elements in the Os-like and Re-like isoelectronic sequence using the general-purpose relativistic atomic structure packages (GRASP^0 and GRASP2K).

Also, kilonovae derive their energy from radioactive decay, including γ-rays, and γ-ray opacity highly depends on photoionization. In this regard, the AUTOSTRUCTURE code was used to compute the photoionization cross section for heavy elements like Tungsten ions.

Finally, we studied methods to generate a reliable dielectronic recombination (DR) database which is one of the most important processes in astrophysical plasmas. AUTOSTRUCTURE was adopted to compute DR rates for Li-like and Be-like Oxygen.

Index words: [atomic data, astrophysical plasmas, neutron star merger]

Computational Atomic Physics for Kilonova Ejecta and Astrophysical Plasmas

by

Zahra Taghadomi

M.S., University of Shiraz, Iran, 2018

A Dissertation Submitted to the Graduate Faculty of the
University of Georgia in Partial Fulfillment of the Requirements for the Degree.

Doctor of Philosophy

Athens, Georgia

2023

Computational Atomic Physics for Kilonova Ejecta and Astrophysical Plasmas

by

Zahra Taghadomi

Major Professor: Phillip C Stancil

Committee: Henning Meyer

Robin Shelton

Electronic Version Approved:

Ron Walcott
Dean of the Graduate School
The University of Georgia
May 2023

Dedication

I would like to dedicate this work to those whose dreams do not turn to reality, not due to the lack of dedication on their part, but merely as a result of their socioeconomic status.

Acknowledgments

I am extremely grateful to my major professor Phillip Stancil for the incredible amount of time he has spent mentoring me during all my graduate work. He has taught me so much about being a researcher and enjoying science.

I am also grateful to my committee members: Dr. Henning Meyer, and Dr. Robin Shelton for their continued guidance and help to improve and correct this dissertation. My dissertation research would not have been possible without their participants. I am grateful that they were willing to share their time and experiences.

Finally, yet importantly, I would like to acknowledge funding agencies, National Aeronautics and Space Administration (NASA) and National Science Foundation (NSF), for financially supporting this research project.

Contents

List of Figures

List of Tables

Chapter 1

Introduction

1.1 Atomic astrophysics and spectroscopy

Astronomy is driven by observing spectra emerging from ground-based and space-based telescopes. Spectroscopy is the science of light–matter interaction and explains all that we see from the universe except neutrinos, cosmic rays, and gravitational waves. Atomic astrophysics forms the link that connects astronomy with fundamental physics at atomic and molecular levels. The trace of astrophysical spectroscopy goes back to the early nineteenth century to the discovery of dark lines in the solar spectrum by Wollaston in 1802 and Fraunhofer in 1815.

In spite of the practical works and analysis, a quantitative understanding of spectroscopy had to await the quantum theory of the atom. Schrödinger's success in finding the right equation that would reproduce the observed hydrogenic energy levels according to the Bohr model and the Rydberg formula was the crucial development.

The lightest and most abundant element in the universe is hydrogen. Whereas the lines of hydrogen are well-known, lines of more complicated species require more detailed knowledge. The reason is that atomic physics gets complicated as one moves on to non-hydrogenic systems, starting with helium. Strict rules, most notably the Pauli exclusion principle, govern the formation of atomic states. But their application is not straightforward, and the full algebraic scheme must be followed, in order to derive and understand which states are allowed by nature to exist, and which are not.

Physical properties of elements refer to spectroscopic and atomic processes, such as energy level structure, radiative transitions, excitations, ionization and more. Also, the physical properties of elements can be recognized through interaction of radiation with matter on the atomic scale. This interaction can be referred as physical phenomena which highly depend on environmental properties, mainly the temperature and density of the medium. The astrophysical environments are diverse, hence it is necessary to consider the physical properties of atoms or ions together with medium parameters.

In the era of multi-messenger astronomy, astronomical sources act as astrophysical laboratories for atomic physics. Ionized materials in astrophysical plasmas constitute over 99% of the observed baryonic matter in the universe, and all information on observable matter is derived from spectroscopy. The observ-

able matter spans a huge range in density–temperature parameter space. The formation of the spectrum from an astrophysical plasma depends on atomic processes that emit or absorb radiation. The astrophysical plasma is composed of electrons, protons and elements in various ionization stages. Also, there is often an external radiation field, for example, from another star or galactic nucleus, interacting with the plasma. A variety of atomic interactions, mainly between the electrons and ions or photon and ions, determine the observed spectral features. In atomic astrophysics we study the qualitative and quantitative nature of the microscopic atomic interactions and the observed spectra. The radiative and collisional interactions depend on the density, temperature and radiation source.

1.2 Atomic processes

Spectral analysis is often complicated and it is difficult to determine physical effects individually. Therefore, various theoretical approximations employed to interpret astrophysical observations. In order to determine when and to what extent a given effect or process will affect spectral lines under expected or specified physical conditions, it is essential to understand atomic processes and the underlying quantum mechanical treatment.

For example, at low temperatures and densities we may expect only the low-lying atomic levels to be excited, which often give rise to infrared (IR) and optical forbidden emission lines. However, if an ultraviolet (UV) radiation field be present at the background, low-lying levels may be excited to higher levels by absorbing UV which would appear not only in the UV but also contribute to the intensities of the IR/optical lines. Therefore, the intensities of observed forbidden lines may involve a contribution from allowed transitions via multiple level cascades. That, in turn, requires a more extensive atomic model with all relevant excited levels.

Fundamental atomic parameters associated with atomic processes are mostly computed theoretically. The task of computational astrophysics is to compute the fundamental quantities, such as cross sections for ionization, recombination and scattering, and transition probabilities for radiative transitions.

The general idea behind the computation is forming an interaction Hamiltonian, H_{int}, that describes the atomic process. Then by representing the initial and final state of the system, ψ_i and ψ_f, the transition matrix can be obtained

$$\langle \psi_i | H_{int} | \psi_f \rangle . \tag{1.1}$$

For any electronic transition, we normally use a way where the ground state wavefunction and excited state wavefunction are together with the so-called " transition dipole moment ". The intensity of a spectral line depends on these three quantities. A moment is a property of the atom or molecule. It can be expanded as multipole moment series. For the electric moment, dipole is the first term, quadrupole the second and weaker term, etc. There is also a magnetic moment which is weaker than the electric moment, and the first term is the magnetic dipole moment. Some selection rules forbid electric dipole radiation, but allow magnetic dipole radiation.

1.3 Origin of elements and fingerprints of heavy element synthesis in the universe

Although the general picture of element formation is well understood, the source of about half of the heaviest elements in the universe has been a mystery for a long time. C, N, O, ..., Mg, ... are produced in low-mass stars and expelled into the interstellar medium (ISM) after they travel off the main sequence. Somewhat heavier elements, up to the iron-peak species, were produced in the explosive ejecta of supernovae. Numerous observations and robust nucleosynthesis models confirm this scenario (Grimmett et al., 2018; Nomoto et al., 2006). However, for heavier elements that require a rapid neutron capture (r-process) mechanism, the details of their production mechanism are an area of active study.

It was postulated by Cameron, 1957 that the merger of binary neutron stars would result in a neutron-rich ejecta that could produce these heavy elements. One of the early nucleosynthesis models which predicted the yields of such events was given by Freiburghaus et al., 1999.

As was announced on October 16, 2017 by the LIGO/Virgo collaboration, the merger of two neutron stars were detected for the first time by their gravitational wave (GW) signatures (LIGO Scientific Collaboration and Virgo Collaboration et al. 2017). Within hours, optical emission was detected from the same region and more than 60 telescopes observed the electromagnetic counterpart EM170817 for weeks until its optical and infrared (IR) emission decayed (Tanvir et al., 2017).

The ejected material from neutron star mergers (NSMs), or "kilonova", is a good candidate for optical and near infrared follow-up observations, which would allow us to study heavy elements production through the rapid neutron capture process or r-process. In principle, analysis of the light curves and spectra of these radioactive transients could be used to quantify the mass and chemical composition of the kilonova. Since almost nothing is known about the optical properties of such material, the largest uncertainty in the understanding would be opacity of the ejecta.

1.4 Outline of this work

This work will attempt to improve the fundamental atomic parameters relevant to heavy elements. The emphasis will be on generating a reliable atomic database, such as energy levels, transition probabilities, photoionization cross sections, and dielectronic recombination rates that are suitable for experimental or spectral analysis.

Chapter 2 introduces the atomic physics behind the models and computational approaches used in this thesis. The atomic processes, thermodynamic conditions, quantum theory behind the atomic structure calculations, and the programs which can be used for calculations will be discussed.

Chapter 3 and chapter 4 show the results of calculated energy levels, transition probabilities of Os isoelectronic sequence as well as their LTE spectra and expansion opacity.

Chapter 5 is the discussion on photoionization cross section of Tungsten ions, W I, W II, W III, and W IV.

Chapter 6 explains the dielectronic recombination rates for the Li-like and Be-like Oxygen. The focus will be on the low temperature region where the rate coefficients are extremely sensitive to the location and strength of near-threshold resonances.

Finally, in chapter 7 the work will be summarized and future work for improving the calculations will be outlined.

Chapter 2

Theory and methods

The interaction between ions and other particles often results in the emission of electromagnetic radiation. Besides the physical conditions of the astrophysical medium, such as temperature, density, and abundances of elements, the spectrum depends on a variety of atom-photon interactions. It is crucial to determine when a specific process or a physical condition will affect the spectral lines.

This chapter provides a necessary background for the collisional processes and the underlying physics. First, individual atomic processes are described , hence we can understand their overall role in astrophysical plasmas. Then we look into opacity and that plays an important role in the transmission of radiation and the evolution of the kilonova ejecta. Then, the theory behind the calculations and their computational approaches will be discussed.

2.1 Collisional and radiative atomic processes

Some important atomic processes in an astrophysical plasma include:

- Electron-ion collisions
- Photoionization
- Electron–ion recombination

2.1.1 Electron-ion collisions

In a plasma with free electrons and positive ions, collisions between the electrons and ions may result in excitation, ionization, or recombination. Figure 2.1 shows a free electron collides with bound electron in an ion. The bound electron in state i can be excited to the discrete higher bound states j ($E < 0$),

$$e_1 + X_i^{+n} \rightarrow e_1^{'} + X_j^{+n}, \tag{2.1}$$

or ionized,

$$e_1 + X^{+n} \rightarrow e_1^{'} + e_2 + X^{+(n+1)}. \tag{2.2}$$

Here, e_1 is the free electron, $e_1^{'}$ is the scattered electron, and e_2 is the ejected electron.

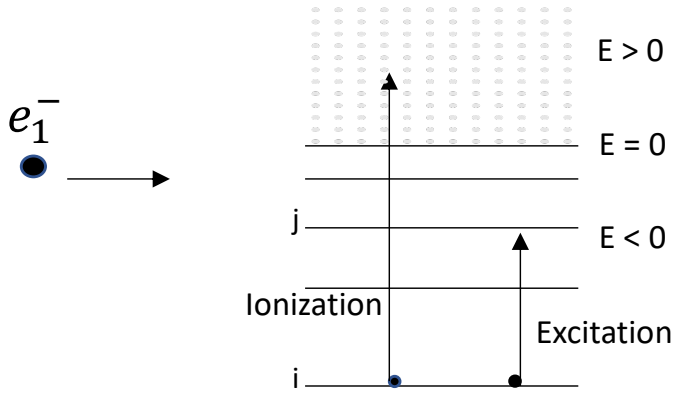

Figure 2.1: Excitation of bound states and ionization into the continuum.

Collision of an electron with an ion leads to "*elastic scattering*" or "*inelastic scattering*".Unlike the latter process, in the former process the energy would not be exchanged. Hence, we are interested in the *inelastic scattering* where the exchange of energy between the electron and the ion results in excitation or de-excitation.

In "*electron impact excitation*" (EIE), Eq. 2.1, the excited electron would decay by emitting a photon $h\nu$. Although "*electron impact ionization*" (EII), Eq. 2.2, may not emit any photon at first sight, but it is a three-body process. Right-hand side of Eq. 2.2 has two free electrons with different energies, and can be followed by various pathways that may cause resonances, like:

$$e_1 + X^{+n} \rightarrow e_1^{'} + e_2 + [X^{+(n+1)}]^* \rightarrow e_1^{'} + e_2 + X^{+(n+1)} + h\nu, \tag{2.3}$$

or

$$e_1 + X^{+n} \rightarrow e_1^{'} + e_2 + [X^{+(n+1)}]^* \rightarrow e_1^{'} + e_2 + e_3 + X^{+(n+2)}. \tag{2.4}$$

The first process, 2.3, is called "*excitation autoionization*", and the second one, 2.4, is "*resonant excitation double autoionization*".

There are many other intermediate processes that lead to EII, these are called the Auger processes. When an incident electron, as shown in Figure 2.2, ionizes an inner shell electron from an ion, the inner shell becomes vacant. Sometimes an upper outer shell electron cascades down to fill the vacancy which follows by emitting a photon, Figure 2.2 a. However, the emitted energy can be transferred to an outer shell electron and eject another electron (Auger electron) from the ion, Figure 2.2 b.

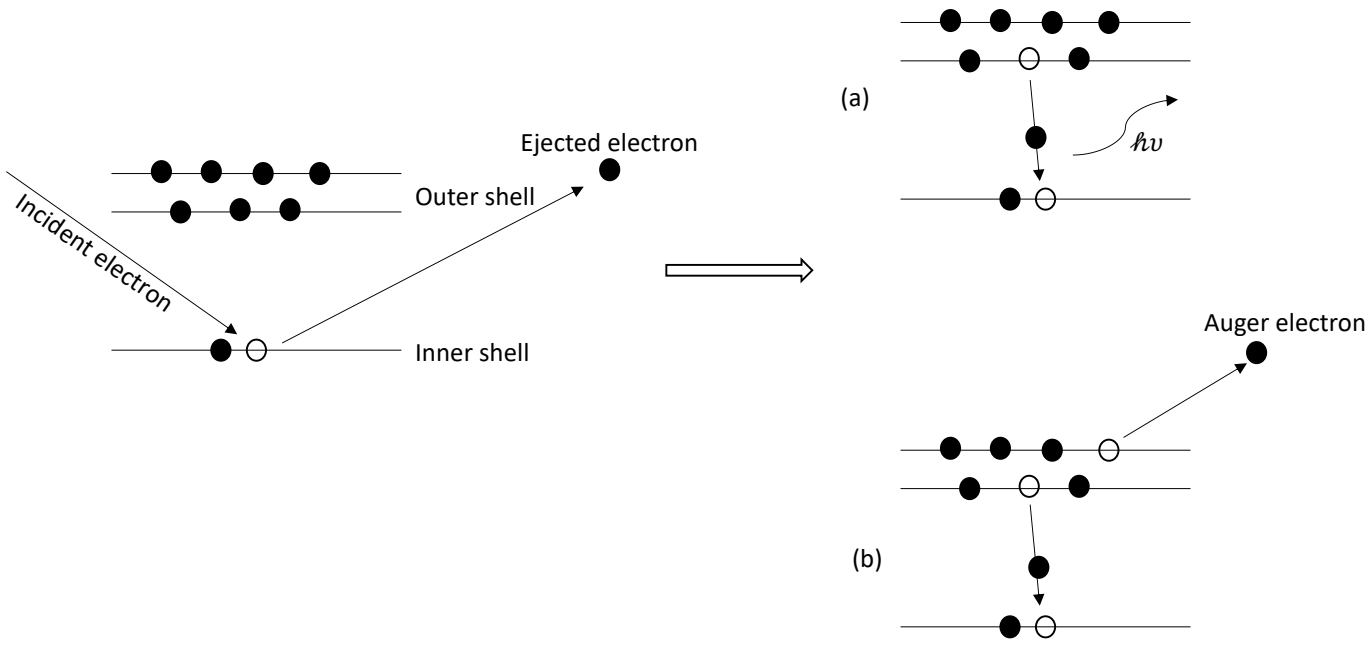

Figure 2.2: Auger process

2.1.2 Photoionization

Most of the astrophysical environments are ionized plasma. The two main sources of ionization are *"electron impact ionization"* that we discussed in the previous section, and *"photoionization"*(PI). When a photon of energy $h\nu$ interacts with an atom or ion, sufficient energy would be transmitted to the atom or ion to eject an electron from a bound state to the continuum one:

$$X + h\nu \rightarrow X^{+} + e(\varepsilon). \tag{2.5}$$

The ejected electron, $e(\varepsilon)$, is called the *"photoelectron"* and has the energy of $\varepsilon = h\nu - E_{IP}$, the difference between incident photon and ionization potential of the atom or ion.

2.1.3 Electron–ion recombination

In the physical content recombination is the inverse of photoionization.

$$X^{+} + e(\varepsilon) \rightarrow X + h\nu. \tag{2.6}$$

A free electron in the continuum state combine with an ion that leads to a photon emission, the recombined ion becomes one charge less than the recombining ion. This process is specifically called *"radiative recombination"* (RR), where the electron is captured into a bound state and the photon is simultaneously

emitted.

In fact, the probability of the autoionization during the recombination process is strong. In general, there are two pathways:

$$X^{+n} + e \rightarrow (X^{+n-1})^{**} \rightarrow \begin{cases} e + X^{+n} & (Autoionization) \\ X^{+n-1} + h\nu & (Recombination) \end{cases} \tag{2.7}$$

Where $(X^{+n-1})^{**}$ represent doubly excited states of the recombined ion. The recombination through this process is called "*dielectronic recombination*" (DR). As the initially free electron becomes captured, the available energy is carried away by the promotion of a bound electron to another bound state. In the second step, the doubly excited ion can be either autoionized by releasing an electron and decaying into the continuum, or emitting a photon and forming a bound state (DR).

Both radiative and dielectronic recombination are important capture processes in highly ionized astrophysical plasma. RR and DR are dominant in different energy or temperature regimes, for example, unlike high-temperature plasmas, in low-temperature plasmas free electrons have low energies that may not be sufficient to excite any double excited autoionizing states. In this case, the dominant process would be RR.

2.2 Opacity

The condition in the kilonova depends on the "total amount of radioactive energy", "decay channels that dominate the energy production", and "efficiency of radioactive decay products". Thermalization of the kilonova mostly comes from radioactive decay products that depends on mass and velocity of the ejecta, magnetic field, and radioactivity. The detailed calculation of the kilonova and its light curve can be found in the literature (Barnes et al., 2016; Kasen et al., 2013).

However, most of these processes are highly affected by how easily photons and elementary particles can pass through the material in any given layer and time. Here, the ability of radiation to pass through material, or opacity, becomes important which depends on the chemical composition, the temperature, and the density of the structure.

The primary mechanisms which account for the opacity are:

- Photon scattering
- Free-free scattering (or bremsstrahlung)
- Bound-bound transitions
- Bound-free transitions (photoionisation)

2.2.1 Photon scattering

When a photon or an electromagnetic wave hit a charged particle, like an electron, causes an oscillating motion of the charge that generates radiation. This process is known as "*scattering*". There are two mechanisms where light is scattered by charged particles, "*Compton scattering*" and "*Thomson Scattering*".

Compton scattering is the inelastic scattering of a photon when interact with a charged particle such as an electron. Whereas, Thomson scattering is a type of elastic scattering of electromagnetic radiation in the presence of a free-charged particle. If the photon energy is comparable to the electron rest energy ($\sim m_e c^2$), Compton scattering should be considered. On the other hand, when the photon energy is much lower then electron rest energy ($\ll m_e c^2$), Thomson scattering becomes important.

In the case of a kilonova, the energy of photon is relatively high that can be compared to the electron rest energy, so Compton scattering would be considered in our work.

2.2.2 Free-free scattering

When an electron moves through an electromagnetic field, it experiences an acceleration and radiates photons. In the case of free-free or Bremsstrahlung, the electron passes through the Coulomb field of a positive ion. As the electron is accelerated during its approach to the ion it radiates photons, and then the radiated photon can be absorbed by the ion:

$$e(\varepsilon) + X_1^+ + h\nu \rightarrow X_2^+ + e(\varepsilon'), \tag{2.8}$$

where 1 and 2 indicates the initial and final states of the ion X^+, and $e(\varepsilon')$ is the scattered electron with different energy.

2.2.3 Bound-bound transitions

This process happens when an electron moves from a bound state to another bound state in an ion or atom by absorbing or emitting a photon:

$$X_1^+ + h\nu_{12} \leftrightarrow X_2^+. \tag{2.9}$$

1 and 2 refers to lower and upper state of the ion X^+.

2.2.4 Bound-free transitions

The bound–free transition or photoionization occurs when the photon is sufficiently energetic to ionize an electron from a bound to a continuum state of an ion:

$$X^+ + h\nu \rightarrow X^{+2} + e(\varepsilon), \qquad h\nu = E_{IP} + \varepsilon. \tag{2.10}$$

E_{IP} is the ionization potential of X^+, and ε is the energy carried away by the ejected electron.

The opacity of a medium is related to both plasma properties such as density and temperature, and atomic properties of the ions or atoms in the plasma like atomic number and energy levels. Considering all the macroscopic and the microscopic parameters of the plasma, the opacity at a single frequency, κ_ν, can be defined as (Pradhan & Nahar, 2011):

$$\kappa_\nu(cm^2 g^{-1}) = \frac{n_A \sigma_\nu}{\rho_A}, \tag{2.11}$$

where $n_A(cm^{-3})$ is the atomic level population, $\sigma_\nu(cm^2)$ the cross section, and $\rho_A(gcm^{-3})$ is the mass density. Having the mass density as $\rho_A = m_A n_A$:

$$\kappa_\nu = \frac{\sigma_\nu}{m_A}, \tag{2.12}$$

and $m_A(g)$ is the atomic mass.

The temperatures, densities and particle energies must be precisely measurable to obtain meaningful results for physical parameters of interest. Fundamental atomic parameters associated with atomic processes are mostly computed theoretically. Our treatment is aimed at a theoretical description of atomic processes. The task is to compute fundamental quantities, such as cross sections for ionization, recombination and scattering, and transition probabilities for radiative transitions.

Another crucial factor is the ionization state of the ions in the plasma at any temperature. In other word, we need to know the electron population in each state of the ions. These concepts lead to a discussion of "*thermodynamic equilibrium*".

2.3 Thermodynamic equilibrium

2.3.1 Non-LTE

Regardless of thermodynamic equilibrium, statistical equilibrium can be assumed in calculating the level populations. It means level populations reach equilibrium on a timescale shorter than the ejecta expansion timescale. To calculate the level populations we must solve the equation of statistical equilibrium. The full form of the statistical equilibrium equation for non-LTE can be written as (Rybicki & Lightman, 1991):

$$\sum_{j>i}[n_j A_{ji} + (n_j B_{ji} - n_i B_{ij})J_{ji}] - \sum_{j<i}[n_i A_{ij} + (n_i B_{ij} - n_j B_{ji})J_{ij}] + \sum_{j\neq i}[n_j C_{ji} - n_i C_{ij}] = 0, \tag{2.13}$$

where n_i is the fractional occupation number at each level that can be described by occupation number density, N_i:

$$n_i = \frac{N_i}{N}, \qquad N = \sum_i N_i. \tag{2.14}$$

A_{ij} is the "*Einstein A-coefficient, or spontaneous radiative decay rate*" in the dimension of s^{-1}. In other words, $1/A_{ij}$ gives the average time, in seconds, that an atom or ion can stay in state i before radiatively decaying to state j. B_{ji} is the "*Einstein B-coefficient for absorption*" which is related to the Einstein A-coefficient by the relation:

$$A_{ij} = \frac{2h\nu_{ij}^3}{c^2} B_{ij}. \tag{2.15}$$

C_{ij} is the rate by which an atom or ion in state i is collisionally changed to state j

$$C_{ij} = N_i K_{ij}(T), \tag{2.16}$$

where $K_{ij}(T)$ is the collision coefficient.

Lastly, j_{ij} in Eq. 2.13 is the "*emissivity due to spontaneous radiative decay*" defined as

$$J_{ij} = \frac{h\nu_{ij}}{4\pi} N_i A_{ij}, \tag{2.17}$$

As one can see, the computation of the level populations in non-LTE is quite complicated and time consuming. It would be notable to consider the conditions and limitations for LTE.

2.3.2 LTE

Local thermodynamic means that all thermodynamic properties of a small volume of matter are the same as their thermodynamic equilibrium values corresponding to the temperature.

If the free electrons are in thermodynamic equilibrium with themselves, then the free-electron energy distribution, $F(E, T_e)$, is given by the Maxwell-Boltzmann distribution at an electron temperature (T_e):

$$F(E, T_e) = \frac{2\ \sqrt{E}}{\sqrt{\pi}\ (kT_e)^{3/2}}\, e^{-E/kT_e}. \tag{2.18}$$

Similarly, if the photons are in thermodynamic equilibrium with themselves, then the energy density distribution is given by the Planck distribution at a radiation temperature T_r:

$$B_\nu(T_r) = \frac{2h\nu^3}{c^2}\ \frac{1}{e^{h\nu/kT_r} - 1}. \tag{2.19}$$

k is the Boltzmann constant, h is the Plank constant, and c is the speed of light.

The fractional occupation number, Eq. 2.14, can then be written as (Osterbrock & Ferland, 2006):

$$n_i = \frac{1}{Z(T_e)} g_i \, e^{-E_i/kT_e} \tag{2.20}$$

It is called "*Boltzmann's Equation*" where $g_i = 2j_i + 1$ is the "statistical weight", and $Z(T)$ is the "normalization constant" or "partition function" of this equation

$$Z(T_e) = \sum_i g_i \, e^{-E_i/kT_e}. \tag{2.21}$$

Excitation in an atom or ion can be caused by collision or radiation. LTE can only exist if the radiation processes can be neglected and the collision is dominant in the plasma. It means that the radiant energy absorbed by an ion is distributed across other ions by collisions before it is radiated by emission. Therefore, a sufficiently high density plasma is required.

For a given temperature, one can define the *critical number density*, n_c, as the density above which the collisions are so frequent, that they keep the populations close to their LTE values (Griem, 1963).

2.4 Atomic Structure Calculations

Atomic structure refers to the organization of electrons in various shells and subshells. Theoretically it means the determinations of electron energies and wavefunctions of bound states of all electrons in the atom, ion or atomic system.

The simplest atomic system belongs to the hydrogen atom, the most abundant element in the universe. The dynamic state of an atom or ion is described by the Schrödinger equation, where the *Hamiltonian* of the system is needed. The one-electron Hamiltonian, like the hydrogen atom, has only one potential term, the electron–nucleus Coulomb attraction potential. For a multi-electron atomic system, electron–electron correlation interactions should be considered in the Hamiltonian. The multi-electron Hamiltonian in atomic units can be written as:

$$H = \sum_{i=1}^{N} [\frac{-1}{2} \nabla_i^2 - \frac{Z}{r_i}] + \sum_{i \neq j} \frac{1}{r_{ij}} \tag{2.22}$$

The first in the Hamiltonian is the electron kinetic energy, the second term is the electron-nucleus potential energy, and the third term accounts for the two-electron Coulomb interaction.

Beyond the single electron case, there is no exact solution to the Schrödinger equation due to the complexity in determining the energies and wavefunctions arising from electron–electron interaction. Hence, an approximate treatment is needed. The most common treatment is the generalization of the Schrödinger equation into the Hartree–Fock equations.

2.4.1 Hartree–Fock method

The Hartree–Fock (HF) method is an approximation approach to obtain total wavefunctions for many-electron systems. This method is based on the variational principle, that starts with a trial wavefunction. The trial function is constructed with adjustable parameters that can be varied to improve the wavefunction. The best values will give the minimum energy

$$\delta < \psi|H|\psi >= 0 \tag{2.23}$$

with the solution of $E = E_{min}$. In addition to optimizing the parameters in the trial function, certain boundary conditions and requirements in atomic calculations must be satisfied.

In the case of $N = 1$, the Hydrogen atom, Eq. 2.22 would be:

$$H = \frac{-1}{2}\nabla^2 - \frac{1}{r} \tag{2.24}$$

where ∇^2 in standard spherical coordinates is

$$\nabla^2 = \frac{1}{r^2}\frac{\partial}{\partial r}(r^2\frac{\partial}{\partial r}) + \frac{1}{r^2\sin\theta}\frac{\partial}{\partial\theta}(\sin\theta\frac{\partial}{\partial\theta}) + \frac{1}{r^2\sin^2\theta}(\frac{\partial^2}{\partial\phi^2}). \tag{2.25}$$

The wavefunction can be separated into radial and spherical function:

$$\Psi(r,\theta,\phi) = R(r)\,Y(\theta,\phi) \tag{2.26}$$

where $R(r)$ is the radial function and $Y(\theta,\phi)$ is the spherical function. Substitution into Eq. 2.24 gives radial and angular equations which lead to "*Laguerre polynomials*" for as a radial equation solution and "*spherical harmonics*" as the angular equation (Shankar, 1994b)

$$\Psi(r,\theta,\phi) = \frac{1}{r}\,P(nl;r)\,Y_{lm_l}(\theta,\phi) \tag{2.27}$$

where $P(nl;r)$ is Laguerre polynomials with *n quantum number* and *l angular quantum number* , and $Y(\theta,\phi)$ is spherical harmonics with m_l *magnetic angular quantum number*. Considering the spin function leads to:

$$\Psi(r,\theta,\phi,\sigma) = P_{nl}\,Y_{l,m_l}\,\chi_{m_s} \tag{2.28}$$

with $m_s = \pm 1/2$.

As a result, the one electron functions can be specified entirely in terms of the four quantum numbers, $\{n\ l\ m_l\ m_s\}$, such functions are called *"spin–orbitals"*.

Assuming an atom to be an N-electron system, $\Psi_{n_i l_i m_{l_i} m_{s_i}}$ is a spin–orbital for the ith electron. In the *"self–consistent"* field method, where an electron moving in the potential of the nucleus and all the $N-1$ electrons, the solution of the Schrödinger equation can be written as (Fischer, 1977):

$$\Psi_{n,l,m_l,m_s}(r,\theta,\phi,\sigma) = (\psi_{n_1,l_1,m_{l_1},m_{s_1}})(\psi_{n_2,l_2,m_{l_2},m_{s_2}})...(\psi_{n_N,l_N,m_{l_N},m_{s_N}}) = \prod_{i=1}^{N} \psi_{n_i l_i m_{l_i} m_{s_i}}. \qquad (2.29)$$

But a simple product form of the total wavefunction would not satisfy the antisymmetry conditions, which grants inter- change of electronic coordinates.

According to the general antisymmetry postulate, the wavefunction must change sign upon interchange of the coordinates of any two electrons, both their spatial or spin coordinates. The mathematical form of a two-particle antisymmetric wavefunction can be written as (Shankar, 1994c):

$$\Psi(\mathbf{r}_1,\mathbf{r}_2) = \frac{1}{\sqrt{2}}[\psi_1(\mathbf{r}_1)\psi_2(\mathbf{r}_2) - \psi_1(\mathbf{r}_2)\psi_2(\mathbf{r}_1)] = \frac{1}{\sqrt{2}} \begin{bmatrix} \psi_1(\mathbf{r}_1) & \psi_1(\mathbf{r}_2) \\ \psi_2(\mathbf{r}_1) & \psi_2(\mathbf{r}_2) \end{bmatrix}. \qquad (2.30)$$

Extending Eq. 2.30 to N-electron system, the wavefunction for the system would be:

$$\Psi = \frac{1}{\sqrt{N!}} \begin{bmatrix} \psi_1(\mathbf{r}_1) & \psi_1(\mathbf{r}_2) & ... & \psi_1(\mathbf{r}_N) \\ \psi_2(\mathbf{r}_1) & \psi_2(\mathbf{r}_2) & ... & \psi_2(\mathbf{r}_N) \\ ... & ... & ... & ... \\ \psi_N(\mathbf{r}_1) & \psi_N(\mathbf{r}_2) & ... & \psi_N(\mathbf{r}_N) \end{bmatrix}, \qquad (2.31)$$

which is called the *"Slater determinant"*.

The Slater determinant, Eq. 2.31, provides qualitative description of orbitals of atoms with more than a single electron. However, the repulsive interactions among the electrons of an atom, as the third term in Eq. 2.22, need to be considered. That is the aim of the self-consistent method, which is the iterative algorithm employed to solve the Hartree–Fock equations. In the computational approaches it will be discussed in detail.

Considering Eq. 2.22 for two electrons system, the Hamiltonian would be:

$$H_{(N=2)} = [\frac{-1}{2}\nabla_1^2 - \frac{Z}{r_1}] + [\frac{-1}{2}\nabla_2^2 - \frac{Z}{r_2}] + \frac{1}{r_{12}} = h_1 + h_2 + h_{12} \qquad (2.32)$$

The first two terms indicate the Hamiltonian for the electron atom, and the third term is the electron-electron interaction. Using Eq. 2.30 as the wavefunction of two-electron system, the energy of the system

will be:

$$E = \langle \Psi(\mathbf{r}_1, \mathbf{r}_2) | H_{(N=2)} | \Psi(\mathbf{r}_1, \mathbf{r}_2) \rangle \,, \tag{2.33}$$

and applying rules defined in Szabo and Ostlund, 2012,

$$\begin{aligned} E = & \langle \psi_1(\mathbf{r}_1) | h_1 | \psi_1(\mathbf{r}_1) \rangle + \langle \psi_2(\mathbf{r}_2) | h_2 | \psi_2(\mathbf{r}_2) \rangle \\ & + \frac{1}{2} \langle \psi_1(\mathbf{r}_1)\psi_2(\mathbf{r}_2) | \, h_{12} \, | \psi_1(\mathbf{r}_1)\psi_2(\mathbf{r}_2) \rangle \\ & \quad - \langle \psi_1(\mathbf{r}_1)\psi_2(\mathbf{r}_2) | \, h_{12} \, | \psi_2(\mathbf{r}_1)\psi_1(\mathbf{r}_2) \rangle \end{aligned} \tag{2.34}$$

The first two terms represent the expectation value of the one-electron system. The third term is called the *direct term* or *Coulomb term*, which defines the Coulomb interaction between two electrons. And the last term is the *exchange term* results from exchange-correlation between electrons with parallel spins that comes from anti-symmetrizing the wavefunction.

Considering Eq. 2.22 as an N-electron Hamiltonian:

$$\begin{aligned} H &= \sum_{i=1}^{N} [\frac{-1}{2} \nabla_i^2 - \frac{Z}{r_i}] + \sum_{i \neq j} \frac{1}{r_{ij}} = \sum_{i=1}^{N} h_i + \sum_{i \neq j} r_{ij}^{-1} \\ &= h_1 + h_2 + ... h_N + r_{12}^{-1} + r_{13}^{-1} + ... + r_{23}^{-1} + r_{24}^{-1} + ... + r_{N-1,N}^{-1}, \end{aligned} \tag{2.35}$$

and extending the Eq. 2.34 to an N-electron system, and using Szabo and Ostlund, 2012 rules, the expression of energy would be:

$$\begin{aligned} E = & \sum_{m=1}^{N} \int d\mathbf{r}_m \; \psi_m^*(\mathbf{r}_m) h_m \psi_m(\mathbf{r}_m) \\ & + \frac{1}{2} \sum_{m=1}^{N} \sum_{n \neq m}^{N} \int d\mathbf{r}_m d\mathbf{r}_n \; \psi_m^*(\mathbf{r}_m) \psi_n^*(\mathbf{r}_n) r_{mn}^{-1} [\psi_m(\mathbf{r}_m)\psi_n(\mathbf{r}_n) - \psi_m(\mathbf{r}_n)\psi_n(\mathbf{r}_m)] \end{aligned} \tag{2.36}$$

As it is just discussed, the N-electron wavefunction for different states of an atom can be represented by an Slater determinant, Eq. 2.31. However, this determinant can only be used for the ground state. There are N electron and M spin orbitals in an atom ($M > N$), and each electron can occupy any of these M spin orbitals. Therefore, the number of all the possible combinations is:

$$\binom{M}{N} = \frac{M!}{N!(M-N)!} \tag{2.37}$$

Also, this number shows how many Slater determinants are needed to create wavefunctions for the N-electron atom.

As an example, for a two-electron system, like the Helium atom, we can have:

$$\Psi_0(\mathbf{r}_1,\mathbf{r}_2) = \frac{1}{\sqrt{2}} \begin{bmatrix} \psi_{1s_{+1/2}}(\mathbf{r}_1) & \psi_{1s_{+1/2}}(\mathbf{r}_2) \\ \psi_{1s_{-1/2}}(\mathbf{r}_1) & \psi_{1s_{-1/2}}(\mathbf{r}_2) \end{bmatrix}, \tag{2.38}$$

and

$$\Psi_1(\mathbf{r}_1,\mathbf{r}_2) = \frac{1}{\sqrt{2}} \begin{bmatrix} \psi_{1s_{+1/2}}(\mathbf{r}_1) & \psi_{1s_{+1/2}}(\mathbf{r}_2) \\ \psi_{2s_{+1/2}}(\mathbf{r}_1) & \psi_{2s_{+1/2}}(\mathbf{r}_2) \end{bmatrix}. \tag{2.39}$$

By using more than one configuration and putting electrons in different orbitals, spatial correlations in the electron motion can be taken into account. This procedure is called *Configuration Interaction (CI)*.

Considering Eq. 2.38 and 2.39, the wavefunction of the system can be written as:

$$\Phi(\mathbf{r}_1,\mathbf{r}_2) = c_0\Psi_0(\mathbf{r}_1,\mathbf{r}_2) + c_1\Psi_1(\mathbf{r}_1,\mathbf{r}_2) \tag{2.40}$$

where c_1 and c_2 are coefficients. Here, ground and the single excited determinants are only considered. But, an infinite number of determinants of doubly, triply, and higher excited determinants exist. Thus, all the infinite set of determinants, $\{\Psi_i\} = \{\Psi_0, \Psi_1, \Psi_2, ...\}$ is considered as a complete set of basis.

This concept can be extended to any N-electron system, and the exact energies of the ground and excited states of the system are the eigenvalues of the Hamiltonian matrix formed from the complete set $\{\Psi_i\}$. CI will be considered in some detail in the computational approaches. Within the context of the Hartree–Fock formulation, the consideration of more than one configuration or CI is known as the *multi-configuration Hartree–Fock (MCHF)* approximation.

The many-electron Hamiltonian would be much easier to handle without the repulsive electron–electron Coulomb term. The simplest treatment for N-electron atoms can be obtained analogy with hydrogen atom. One of the approximations using this analogy is the "*Central-field approximation*".

2.4.2 Central-field approximation

In the *central-field approximation*, it is assumed that each electron is in the field of the nucleus and the other $N-1$ electrons, and an "*effective potential*" is formed.

The Eq. 2.22 consists of a radial and non-radial part. The central-field approximation involves neglecting the non-radial part and keeping the radial part which is assumed to be dominant. Whereas Hartree–Fock method accounts the electron–electron interaction explicitly.

The effective potential $U(r)$ combines the radial electron–nuclear term, Ze^2/r_i, with an averaged electron–electron term. The approximate N -electron Hamiltonian then becomes (Pradhan & Nahar, 2011):

$$H = -\sum_{i=1}^{N} \frac{\hbar^2}{2m}\nabla_i^2 + U(r), \tag{2.41}$$

where

$$U(r) = -\sum_{i=1}^{N} \frac{e^2 Z}{r_i} + \Big\langle \sum_{i \neq j}^{N} \frac{e^2}{r_{ij}} \Big\rangle \tag{2.42}$$

is the *central-field potential*. $U(r)$ contains the electron–nuclear term that increases in magnitude with Z. Therefore, accuracy of the central-field approximation for a given number of electrons improves with increasing Z number of an ion, or along an isoelectronic sequence.

The Schrödinger equation for this Hamiltonian differs slightly from the equation for Hydrogen atom. In order to get the correct equation, $1/r$ in Eq. 2.24 should be replaced by $U(r)$. Since the central-field potential, $U(r)$, consists only of the radial part, the radial part of the wavefunction will be changed. As a result, the spherical part of the wavefunction will remain the same as Hydrogen atom, Eq. 2.27, with the same orbital angular momentum states.

The wavefunction can be computed by knowing $U(r)$, but the boundary conditions need to be applied. The boundary conditions on $U(r)$ are:

$$U(r) \sim \begin{cases} -\frac{Z}{r} & if \;\; r \to 0 \\ \\ -\frac{Z-N+1}{r} & if \;\; r \to \infty \end{cases} \tag{2.43}$$

Considering the Eq. 2.43 boundary conditions there are several ways to choose the central potential $U(r)$. Particularly useful procedures are the "*Thomas–Fermi–Dirac– Amaldi*" (TFDA) and "*Hartree potential*" (HF).

Thomas–Fermi–Dirac– Amaldi

In the TFDA central potential, it is assumed that the charge distribution is spherically symmetric. It means the negative charge of the electrons is distributed continuously and spherically symmetrically around the positive charge of the nucleus. There are cells in phase space of volume h^3, where h is Planck's constant ($h = 4.110^{-5}$ eV.Hz^{-1}). Each of the cells can be occupied with two electrons, one with spin up and the other with spin down. So, the spatial density of electrons is:

$$\rho = \frac{2(4/3\pi p_F^3)}{h^3} \tag{2.44}$$

where p_F is the *Fermi momentum*, the maximum momentum occupied in phase space. Based on the boundary conditions and quantum statistics, the TFDA potential was written as (Eissner & Nussbaumer, 1969):

$$U(r) = -\frac{Z}{r}\phi(x) \tag{2.45}$$

where $\phi(x)$ is the solution to the "the Poisson equation" connecting charge density and potential,

$$\phi(x) = e^{-Zr/2} + \lambda_{nl}(1 - e^{-Zr/2}), \quad x = \frac{r}{\mu} \tag{2.46}$$

and μ is a constant:

$$\mu = 0.8853\ (\frac{N}{N-1})^{2/3}\ Z^{-1/3}. \tag{2.47}$$

Having the central potential $U(r)$, it is possible to compute the radial part of the wave equation for one-electron orbitals $P_{nl}(r)$

$$[\frac{d^2}{dr^2} - \frac{l(l+1)}{r^2} + 2U(r) + \varepsilon_{nl}]\ P_{nl}(r) = 0. \tag{2.48}$$

P_{nl} is obtained numerically from Eq. 2.48 as $r \to 0$ and $r \to \infty$.

Hartree potential

As it has been discussed in the Hartree–Fock method, the Hartree assumption was that the nucleus together with the electrons formed a spherically symmetric field. And the total wavefunction was the product of the single electron wavefunction as given in Eq. 2.29. Hence the total charge density at position $\mathbf{r}$ due to all electrons except i is (Fischer, 1977):

$$\rho(\mathbf{r}) = -e \sum_{i \neq j} |\psi_j(\mathbf{r}_j)|^2 \tag{2.49}$$

This charge density creates an mean potential that can be calculated using the Poisson equation:

$$\nabla^2 U(r) = -\frac{\mathbf{r}}{\varepsilon_0}. \tag{2.50}$$

The solution in atomic units to this equation will be:

$$U(r) = -\sum_{i \neq j} \int \frac{|\psi_j(\mathbf{r'}_j)|^2}{|\mathbf{r}_i - \mathbf{r'}_j|} d\mathbf{r'}_j. \tag{2.51}$$

Then having $U(r)$, a numerical approach is needed to solve Eq. 2.48. Using the calculated P_{nl}, the wavefunction for each electron can be improved, by performing the calculations for Eq. 2.49 - Eq. 2.51 until it converges. That is the aim of the self-consistent iterative Hartree scheme.

In earlier sections the non-relativistic Hamiltonian, Eq. 2.22, was considered. In a relativistic approach the particle velocities are involved. From the Bohr model, The energy of the n-th level for any atom is described as $m_e v^2/2 \sim Z/r_e$. So, as the atomic number Z increases along the periodic table, the velocity of the inner-shell electrons also increases. For elements $Z > 10$ the velocity of an electron in the first orbit is already a good fraction of the the speed of light c. As a result, for heavy elements the relativistic effects in the Hamiltonian needs to be considered.

2.4.3 Dirac equation

The Dirac equation is a generalization of Schrödinger's equation, in a relativistic setting. It combines quantum mechanics with the theory of Special relativity. The time-independent Dirac Hamiltonian for a free particle with the relativistic motion was described as (Shankar, 1994a):

$$H_{Dirac} = \alpha \cdot \mathbf{p}\, c + \beta mc^2 \tag{2.52}$$

where α and β are 4×4 matrices defined as:

$$\alpha_x = \begin{pmatrix} 0 & 0 & 0 & 1 \\ 0 & 0 & 1 & 0 \\ 0 & 1 & 0 & 0 \\ 1 & 0 & 0 & 0 \end{pmatrix}, \ \alpha_y = \begin{pmatrix} 0 & 0 & 0 & -i \\ 0 & 0 & i & 0 \\ 0 & i & 0 & 0 \\ i & 0 & 0 & 0 \end{pmatrix}, \ \alpha_z = \begin{pmatrix} 0 & 0 & 1 & 0 \\ 0 & 0 & 0 & 1 \\ 1 & 0 & 0 & 0 \\ 0 & 1 & 0 & 0 \end{pmatrix} \tag{2.53}$$

and

$$\beta = \begin{pmatrix} 1 & 0 & 0 & 0 \\ 0 & 1 & 0 & 0 \\ 0 & 0 & -1 & 0 \\ 0 & 0 & 0 & -1 \end{pmatrix}. \tag{2.54}$$

In the presence of an external electromagnetic field The free-particle Dirac Hamiltonian may be modified to:

$$H = \alpha \cdot (c\mathbf{p} - q\mathbf{A}) + \beta mc^2 + q\phi \tag{2.55}$$

where $\mathbf{A}$ and ϕ are vector and scalar potentials related by the Lorentz force.

In the Dirac Hamiltonian Eq. 2.52, two-electron effects are not included. In order to include two or more electrons, several approximations have been introduced.

Breit–Pauli approximation

The Breit–Pauli approximation describes two or more electrons interacting electromagnetically to first order in perturbation theory. The nucleus of an atom is treated as a point source of an external field for the electrons. For N particles, the Breit–Pauli Hamiltonian can be written as (Dyall & Fægri Jr, 2007):

$$\begin{aligned} H_{BP} &= H_{NR} + H_{mass} + H_{Dar} + H_{so} \\ &\quad + \frac{1}{2} \sum_{i \neq j}^{N} [g_{ij}(so') + g_{ij}(ss') + g_{ij}(css') + g_{ij}(d) + g_{ij}(oo')]. \end{aligned} \tag{2.56}$$

H_{NR} is the non-relativistic Hamiltonian Eq. 2.22, H_{mass} is related to the energy of a mass particle (here an electron) that has relativistic velocity, $E^2 = c^2[m^2v^2 + m_0^2c^2]$,

$$H_{mass} = -\frac{\alpha^2}{8}\sum_i^N p_i^4. \tag{2.57}$$

H_{Dar} is the Darwin interaction term which is due to one electron reacting to the magnetic field generated by the other electrons. For a point nucleus it can be written as:

$$H_{Dar} = -\frac{\alpha^2}{8}\sum_i^N \nabla^2(\frac{Z}{r_i}), \tag{2.58}$$

and H_{so} is the spin-orbit interaction term

$$H_{so} = -\frac{\alpha^2}{2}\sum_i^N \frac{Z}{r_i^3} l(i)\cdot s(i). \tag{2.59}$$

The other terms include all magnetic effects among the electrons,

$$g_{ij}(so') = -2\alpha^2\big[(\frac{\mathbf{r}_{ij}}{r_{ij}^3}\times\mathbf{p}_i)\cdot(\mathbf{s}_i + 2\mathbf{s}_j)\big] \tag{2.60}$$

is the spin–other-orbit coupling, it defines the electron i with momentum $\mathbf{p}_i$ is orbiting the electron j. The spin–spin coupling term is:

$$g_{ij}(ss') = 4\alpha^2\big[\frac{\mathbf{s}_i\cdot\mathbf{s}_j}{r_{ij}^3} - \frac{3(\mathbf{s}_i\cdot\mathbf{r}_{ij})\cdot(\mathbf{s}_j\cdot\mathbf{r}_{ij})}{r_{ij}^5}\big]. \tag{2.61}$$

While

$$g_{ij}(d) = -\alpha^2\nabla_i^2(\frac{1}{r_{ij}}) \tag{2.62}$$

represent the electron in the electric field of another electron, and

$$g_{ij}(oo') = -\frac{2\alpha^2}{r_{ij}}\big(\mathbf{p}_i\cdot\mathbf{p}_j + \frac{(\mathbf{r}_{ij}\cdot\mathbf{p}_i)(\mathbf{r}_{ij}\cdot\mathbf{p}_j)}{r_{ij}^3}\big) \tag{2.63}$$

is the orbit–orbit interaction term.

The Breit–Pauli Hamiltonian is a 'low-Z' approximation that is valid when the expansion parameter satisfies $\alpha^2 Z \ll 1$. The main problem as moving to higher Z is that the one-body mass–velocity and Darwin terms become too large to be treated as a perturbation (Cowan & Griffin, 1976). The *Dirac–Fock approximation* is more accurate when dealing with higher atomic number Z.

Dirac–Fock approximation

In this approximation instead of considering the relativistic terms as a perturbation, a fully relativistic treatment is employed. The Hamiltonian in this approximation is written as:

$$H_{DF} = \sum_{i=1}^{N} H_D(i) + \sum_{i \neq j}^{N} \frac{1}{|\mathbf{r}_i - \mathbf{r}_j|}, \tag{2.64}$$

the first term

$$H_D = c\alpha \cdot \mathbf{p} + (\beta - 1)c^2 - \frac{Z}{r} \tag{2.65}$$

is the one-body contribution for an electron due to kinetic energy and interaction with the electric charge of the nucleus.

Comparing Eq. 2.64 and Eq. 2.35 it can be seen that Eq. 2.64 is the relativistic version of the Hartree–Fock equations Eq. 2.35. Hence, They can be solved in a similar manner for more accurate energies and wavefunctions.

Although the basic theoretical rules and background of atomic structure calculations have been discussed, a complete understanding is based on actual computations. In the next section all the packages and computational approaches employed in this work will be explained in detail.

2.5 Computational Approaches

For the discussed theoretical methods and approximations, several codes have been designed for large calculations. Some of them are only designed for atomic and ionic structures, however the other codes are capable of calculating both atomic structures and processes like photoionization and dielectronic recombination.

For the purpose of our work, we applied GRASP^0, GRASP2K, and AUTOSTRUCTURE. The first two packages are mostly used for atomic and ionic structures, while the AUTOSTRUCTURE code is employed for atomic processes.

2.5.1 GRASP^0 and GRASP2K

A general-purpose relativistic atomic structure program (GRASP), is a code for calculating atomic energy levels, orbitals, and radiative transition data within the relativistic formalism. The GRASP^0 package is based on the Oxford multiconfiguration Dirac–Fock (MCDF) (Grant et al., 1980) and higher order corrections (Mackenzie et al., 1980) codes published in 1980. The GRASP2K package (Jönsson, Gaigalas, & Bieroń, 2013) is a later iteration of GRASP^0 and based on the fully relativistic multiconfiguration

Dirac–Hartree–Fock (MCDHF) method.

Solution to the one-electron Dirac equation in a spherically symmetric potential is given as

$$\psi_{n\kappa m} = \frac{1}{r}\begin{pmatrix} P_{n\kappa}(r)\ \chi_{\kappa m}(\theta,\phi) \\ iQ_{n\kappa}(r)\ \chi_{-\kappa m}(\theta,\phi). \end{pmatrix} \tag{2.66}$$

$P_{n\kappa}(r)$ and $Q_{n\kappa}(r)$ are the large and small component radial wavefunctions, respectively. $\chi_{\kappa m}(\theta,\phi)$ is the two-component spinor. Spherical spinors are eigenfunctions of $\sigma\cdot\mathbf{L}$ with σ are the Pauli matrices and $\mathbf{L}$ as the orbital angular momentum. Introducing the operator

$$K = -1 - \sigma\cdot\mathbf{L}, \tag{2.67}$$

the eigenvalue equation for K would be κ,

$$K\,\chi_{\kappa m}(\theta,\phi) = \kappa\,\chi_{\kappa m}(\theta,\phi). \tag{2.68}$$

Having $s = \pm 1/2$ and the angular momentum j as $j = l \pm 1/2$, the two-component spherical spinors are represented as:

$$\chi_{l+1/2\ l\ m}(\theta,\phi) = \begin{pmatrix} \sqrt{\frac{l+m+1/2}{2l+1}}Y_{l\ m-1/2}(\theta,\phi) \\ \sqrt{\frac{l-m+1/2}{2l+1}}Y_{l\ m+1/2}(\theta,\phi) \end{pmatrix}, \tag{2.69}$$

$$\chi_{l-1/2\ l\ m}(\theta,\phi) = \begin{pmatrix} -\sqrt{\frac{l-m+1/2}{2l+1}}Y_{l\ m-1/2}(\theta,\phi) \\ \sqrt{\frac{l+m+1/2}{2l+1}}Y_{l\ m+1/2}(\theta,\phi) \end{pmatrix}. \tag{2.70}$$

From the discussion above, $\kappa = -l-1$ for $j = l+1/2$ and $\kappa = l$ for $j = l-1/2$.

The radial components $P_{n\kappa}(r)$ and $Q_{n\kappa}(r)$ satisfy the equations

$$\Big(\frac{d}{dr} + \frac{\kappa}{r}\Big)P_{n\kappa}(r) + \Big(2c + \frac{V-\varepsilon_{n\kappa}}{c}\Big)Q_{n\kappa}(r) = 0, \tag{2.71}$$

$$\Big(\frac{d}{dr} - \frac{\kappa}{r}\Big)Q_{n\kappa}(r) - \Big(\frac{V-\varepsilon_{n\kappa}}{c}\Big)P_{n\kappa}(r) = 0. \tag{2.72}$$

Here V is the potential and $\varepsilon_{n\kappa}$ is the energy of the state n with κ number. In the non-relativistic limit, $c\to\infty$, $(V-\varepsilon)/c \ll 2c$, it is obtained that:

$$P''_{n\kappa}(r) - \frac{\kappa(\kappa+1)}{r^2}P_{n\kappa}(r) + 2(V-\varepsilon_{n\kappa}) = 0 \tag{2.73}$$

and

$$Q_{n\kappa}(r) \simeq -\frac{1}{2c}\Big(P'_{n\kappa}(r) + \frac{\kappa P_{n\kappa}(r)}{r}\Big). \tag{2.74}$$

Therefore, as $c \to \infty$, $P_{n\kappa}(r)r$ goes over into the non-relativistic radial wave function with $\kappa(\kappa+1) = l(l+1)$ while $Q_{n\kappa}(r)$ tends to zero (V. Burke & Grant, 1967).

Given Eq. 2.66 as the configuration state function (CSF), the wavefunction for an N-electron atomic state is approximated by an atomic state function (ASF) which is a linear combination of CSFs of the one-electron system

$$\Psi(\pi J) = \sum_{i=1}^{n_c} c_i \psi_i(n\kappa m), \tag{2.75}$$

where i runs over all the CSFs ($i = 1, \ldots, n_c$), c_i is the mixing coefficient, π represents the parity of the ASF, and J is the final angular momentum quantum number.

The Dirac Hamiltonian for an N-electron atom, Eq. 2.64, and the CSFs are the main concepts in the MCDF calculations. For better understanding of how the codes work, each step of the program will be explained.

Aspects of processing

The theory underlying both the GRASP^0 and GRASP2K calculations is similar except some improvements in the code that is going to be discussed at the end of the section.

Generating lists of CSFs The computation starts with generating lists of CSFs, after receiving the nuclear data. A list of CSFs begins with defining the core orbital which are fully occupied and need not be part of the CSFs, and the remaining orbitals specify the list of CSFs. Then, the CSFs are arranged into symmetry blocks including the configuration, J quantum number of each subshell, and the total J quantum number.

At the end of the computations, it is possible that J-J coupling at this point be transformed into L-S-J coupling of CSFs basis.

Providing initial estimates of the radial wave functions At this step, the program estimates the radial components of the wave functions, $P_{n\kappa}(r)$ and $Q_{n\kappa}(r)$, using the *Thomas-Fermi potential* Eq. 2.45

$$\begin{aligned} P_{n\kappa}(r) &= P_{n\kappa}^{TF}(r) \\ Q_{n\kappa}(r) &= \frac{\alpha}{2}\left(\frac{d}{dr} + \frac{\kappa}{r}\right) P_{n\kappa}(r), \end{aligned} \tag{2.76}$$

where the equation for $Q_{n\kappa}(r)$ comes from Eq. 2.74 and α is the fine structure constant.

Expansion coefficients Here, a weighted energy functional of the levels that the calculation began with is constructed, then by applying the variational principle the expansion coefficients are determined

$$\left(\mathbf{H} - \mathbf{1}\varepsilon_i\right) c_i = 0, \tag{2.77}$$

where $\mathbf{1}$ is the $n_c \times n_c$ unit matrix, ε_i is given by

$$\varepsilon_i = \langle \Psi(\pi J)|H|\Psi(\pi J)\rangle \equiv c_i^* \, \mathbf{H} \, c_i \tag{2.78}$$

is the energy of the atomic state i, and $\mathbf{H}$ is the Hamiltonian matrix.

The Hamiltonian matrix The Hamiltonian matrix, $\mathbf{H}$, has the elements

$$H_{ij} = \langle \psi_i(n\kappa m)| \; H \; \left|\psi_j(n\kappa m)\right\rangle \tag{2.79}$$

which are expressed in terms of angular and radial integrals. According to the approach introduced by Grant, 1970, the matrix elements can be written as:

$$\langle \psi_i(n\kappa m)| \; H \; \left|\psi_j(n\kappa m)\right\rangle = d^{\kappa}(j'm', jm) \left\langle \psi_i(n'\kappa')\right| \; H \; \left|\psi_j(n\kappa)\right\rangle . \tag{2.80}$$

Here, $\langle \psi_i(n'\kappa')| \; H \; \left|\psi_j(n\kappa)\right\rangle$ is the radial integral and $d^{\kappa}(j'm', jm)$ represents an angular momentum coupling coefficient which appears when integrating over polar angles in the matrix elements.

Self-consistent field procedure Beginning with the total energy Eq. 2.78 and estimating wavefunction Eq. 2.76, the new radial wavefunction can be calculated from Eq. 2.71 and Eq. 2.72. Then, an improved estimated set of radial functions is obtained from

$$\begin{pmatrix} P_{n\kappa}^{est}(r) \\ Q_{n\kappa}^{est}(r) \end{pmatrix} \rightarrow (1-\eta) \begin{pmatrix} P_{n\kappa}^{new}(r) \\ Q_{n\kappa}^{new}(r) \end{pmatrix} + \eta \begin{pmatrix} P_{n\kappa}^{est}(r) \\ Q_{n\kappa}^{est}(r) \end{pmatrix}, \tag{2.81}$$

with $0 < \eta < 1$.

Having the new estimates for the radial wavefunctions, calculations for the energy and the coefficients are repeated until the values from one iteration to the next one agree to within specified accuracy.

Quantum Electrodynamic (QED) corrections Other corrections beyond the Dirac theory for a many-electron system are assumed as a one-electron system.

The main relativistic correction to the electron-electron Coulomb interaction is the *transverse photon interaction*

$$H_T = -\sum_{i<j}^{N} \left[\alpha_i \cdot \alpha_j \frac{\cos\left(\omega_{ij} r_{ij}/c\right)}{r_{ij}} + (\alpha_i \cdot \nabla_i)(\alpha_j \cdot \nabla_j) \frac{\cos\left(\omega_{ij} r_{ij}/c\right) - 1}{\omega_{ij}^2 r_{ij}/c^2} \right]. \tag{2.82}$$

This equation may be an appropriate assumption for singly occupied orbitals, but not valid for multiply occupied ones.

Another correction is the *self-energy* correction. It is computed with the screened-hydrogenic approximation. However, this model may not describe well the orbitals that are far from hydrogenic.

Transition data A transition from ASF $\Psi(\pi J)$ to another ASF $\Psi(\pi' J')$ for any type of transition are computed from the matrix element

$$\left\langle \Psi(\pi' J') \right| | O^K | | \Psi(\pi J) \rangle \,, \tag{2.83}$$

where O^K is transition operator that corresponds to the appropriate moment of the radiation field, and K defines the order of transition (Grant, 1974). The allowed transitions corresponded to the electric dipole moment, and higher-order multipole moments are forbidden transitions.

In some situations, based on the selection rules and according to usual approximations, the transition cannot happen. However, at a higher level of approximation the transition is allowed with low probability. As an example, if Eq. 2.83 is said to be zero for an $E1$ transition, then $M1$ or $E2$ transition can still produce radiation.

Structure of the program

Unlike GRASP^0, to perform a calculation using the GRASP2K, a number of programs need to be run in a particular sequence. Table 2.1 shows the typical sequence of GRASP2K.

Table 2.1: Typical sequence of GRASP2K

rnucleus	Generation of nuclear data
↓	
rcsfexcitation	Specify multireference and orbital set
↓	
rcsfgenerate	Generation of list of CSFs based on multireference data
↓	
rangular	Angular integration
↓	
rwfnestimate	Initial estimates of radial orbitals
↓	
rmcdhf	Self-consistent field procedure
↓	
rci	QED corrections
↓	
jj2lsj	Transform representation from JJ- to LSJ-coupling
↓	
rtransition	Transition data

GRASP2K was the main program for the atomic structure calculations in this work, and GRASP^0 was used for comparison. Although both programs use the same method, many improvements have been applied to the new version GRASP2K. Comparing to GRASP^0, the Grasp2K package can handle expansions with hundreds of thousands of CSFs. Also, in the previous version, levels were weighted

equally by their statistical weight $2J+1$, however, in the new version it is possible to specify other weights to the levels.

Another important feature of GRASP2K is that the program can transform *JJ* coupling to *LSJ* coupling, this feature provides us the term label for each level. Previously, the program was capable to provide the configuration and the *J* number corresponding to that level without knowing the *LS* term of that level.

2.5.2 LTE spectra and expansion opacity

In this work, the aim of atomic structure calculations is to provide the LTE spectra and expansion opacity of the *r*-process ejecta from neutron star mergers. As it is discussed in 2.2, the opacity depends on the density, the temperature, and atomic properties of the ions or atoms of the plasma, which is the Kilonova ejecta.

GRASP2K was used to generate the energy levels and transition rates for different ions; approach by Kasen et al., 2013 was applied to compute the opacity.

According to Eq. 2.11 the opacity depends on the atomic/ionic level populations and transition probabilities. All the processes described in 2.1 can affect the level populations and hence the opacity. However, physical conditions of the ejecta determine which of them is the dominant atomic process.

After the merger, the ejecta starts expanding rapidly, therefore it becomes important to set the stage of the ejecta since the density and temperature vary at different stages. The focus of this work is on a day after the merger, the density of the ejecta at one day, $t_{ej} = 1$, can be estimated as (Kasen et al., 2013):

$$\rho_0 \approx \frac{M_{ej}}{(4\pi/3)v_{ej}^3 t_{ej}^3} \approx 2.8 \times 10^{-13} \frac{M_{-2}}{v_{0.1}^3 t_d^3} g\ cm^{-3}, \tag{2.84}$$

where $M_{-2} = M_{ej}/10^{-2} M_\odot$, $v_{0.1} = v_{ej}/0.1c$, and $t_d = t_{ej}/day$.

After the merger, as the ejecta expands, the material cools effectively, but then the decay of *r*-process nuclei reheats the ejecta. It is estimated that the ejecta temperature 1 day after the merger would be in the range $T \sim 10^3 - 10^4 K$ (Metzger et al., 2010).

According to the density of the ejecta at the given temperature, the environment of the kilonova ejecta at early days has sufficiently high density that LTE can be assumed. Under this condition, the occupation number for each level can be calculated using Eq. 2.20. Regarding to the cross section, in general this quantity is characterized by inverse mean free path which is the average distance that a particle travels before collisions.

The kilonova ejecta has high expansion velocity that all frequencies are shifted due to the Doppler effect, hence the correct approximation to the description of radiation, absorption, and scattering is a problem. In this regard, the concept of *expansion opacity* has been introduced (Karp et al., 1977).

Within a wavelength range (λ_i, $\lambda_i + \Delta\lambda_i$) there are some strong lines which are being shifted at a velocity gradient $\Delta v_s = c\Delta_i/\lambda_i$. Then having the mean free path $l_{mfp} = \Delta v_s t_{ej}$, the cross section would be:

$$\sigma \approx \frac{1}{l_{mpf}} \approx \frac{1}{ct_{ej}} \frac{\lambda_i}{\Delta\lambda_i}. \tag{2.85}$$

The Sobolev optical depth (Sobolev, 1960) is given by

$$\tau_i = \frac{\pi e^2}{m_e c} f_{osc} n_l t_{ej} \lambda_i, \tag{2.86}$$

with the probability that a photon is scattered or absorbed is $1 - e^{-\tau_i}$. Here, f_{osc} is the oscilator strength and n_l is the number density in the lower state. Then the Eq. 2.87 can be written as (Eastman & Pinto, 1993):

$$\sigma = \frac{1}{ct_{ej}} \sum_i \frac{\lambda_i}{\Delta\lambda_i} [1 - e^{-\tau_i}]. \tag{2.87}$$

Having all the required quantities, the expansion opacity ($cm^2 g^{-1}$) is given by:

$$\kappa_{ex}(\lambda) = \frac{1}{ct_{ej}\rho} \sum_i \frac{\lambda_i}{\Delta\lambda_i} [1 - e^{-\tau_i}], \tag{2.88}$$

where the sum runs over all lines in the wavelength bin $\Delta\lambda_i$ for each ion in the ejecta.

Adopting computed atomic structure for different ions, the LTE spectra and expansion opacity are calculated. The LTE spectra are obtained from the line intensities,

$$I(i,k) = F(i,k) A_{ki}, \tag{2.89}$$

where A_{ki} is the transition probability and $F(i)$ is the relative LTE population for level i that can be calculated from 2.20 ($F(i) = n_i$).

Among all the sources of opacity, the expansion opacity due to bound–bound transitions are dominant under the kilonova ejecta conditions. The other sources of opacity, free–free, bound-free, and electron scattering, are not considered (Kasen et al., 2013).

2.5.3 AUTOSTRUCTURE

AUTOSTRUCTURE (Badnell, 2011b) is a general code for the calculation of atomic and molecular processes in plasmas (energy levels, photoionization cross sections, dielectronic and radiative recombination cross sections, etc.). It makes use of non-relativistic wavefunctions and the full Breit interaction in the Pauli approximation for relativistic corrections.

The code is based on the non-relativistic Hamiltonian Eq. 2.22 and the Slater determinant. Then a central field approximation is applied for electron– electron interaction. In regards to the relativistic corrections, as it has been discussed in Breit–Pauli approximation, relativistic effects are considered to first order in perturbation theory as given by Eq. 2.56.

In this work, AUTOSTRUCTURE was employed for computing the photoionization (PI) cross section and dielectronic recombination (DR) rate. These calculations are based on the Breit–Pauli distorted-wave (DW) approach for the electron-impact excitation of atomic ions which have been implemented within the code. In the DW approach, the incident electron is taken to be elastically scattered and the transition between the initial and final elastic-scattering states is calculated by perturbation method (Badnell, 2011c; Eissner et al., 1974).

PI cross section

The Breit–Pauli approximation method is applied to find the wavefunction and the corresponding energy for the $electron - ion$ system. The total photoionization cross section in atomic units is written as:

$$\sigma_{PI} = \frac{4}{3}\pi^2 a_0^2 \frac{h\nu}{g_i}\alpha \mathbf{S}. \tag{2.90}$$

g_i is the statistical weight $(2J_i + 1)$ of the initial bound state, $h\nu$ is the photon energy, α is the fine structure constant, and a_0 is the Born radius.

S defines the transition strength from an initial bound state i of energy E_i to a final continuum state f of energy $E_f = E_i + h\nu$

$$\mathbf{S} = |\left\langle \Psi_f \right| |\mathbf{D}| \Psi_i \rangle|^2 = \left| \left\langle \Psi_f \right| | \sum_{j=1}^{N+1} er_j |\Psi_i\rangle \right|, \tag{2.91}$$

where **D** is the dipole operator and the sum is over the number of electrons.

DR rate coefficients

The AUTOSTRUCTURE code produces large amounts of data on energy levels and transition probabilities for photoionization. The post-processing code of Atomic Data and Analysis Structure, (ADAS) package deals with one specific process, like DR (Badnell et al., 2003).

In the section 2.1.3 it is explained that the DR process happens by capturing a free electron and forming a doubly excited state ion. Generally, any state of the unrecombined ion can serve as the initial state in the DR process. In low-density plasmas the population density of the metastables are not significant to be considered in the recombination rate. However, in higher-density plasmas the metastables have sufficient population to be considered as the initial states in the DR process. In this regard, for more accurate calculation the recombination data from all metastable levels need to be computed.

The dielectronic recombination rate coefficient from an initial metastable state i of an ion X^{+N} into a final state f of an ion $X^{+(N+1)}$ is given by (Burgess, 1964)

$$\alpha_{fi}^{+N} = \left(\frac{4\pi a_0^2 I_H}{k_B T_e}\right)^{3/2} \sum_j \frac{g_j}{2g_i} e^{-E_c/(k_B T_e)} \times \frac{\Sigma_l A^a_{j\to i,E_c l}\, A^r_{j\to f}}{\Sigma_h A^r_{j\to h} + \Sigma^a_{m,l} A^a_{j\to m,E_c l}}. \tag{2.92}$$

In this equation g_j is the statistical weight $(2J_j+1)$ of the $(N+1)$-electron doubly excited state j, and g_i is the statistical weight $(2J_j+1)$ of the N-electron target state. E_c is the energy of the continuum electron with orbital number l ($E_c = E_{N+1} - E_N$), I_H is the ionization potential energy of the hydrogen atom, k_B is the Boltzmann constant, a_0 is the Bohr radius, and T_e is the the electron temperature.

The autoionisation transition rate, A^a is given in first-order perturbation theory by

$$A^a_{i\to f} = \frac{2I_H}{\hbar} |\langle f|H|i\rangle|^2, \tag{2.93}$$

and the radiative rate A^r is

$$A^r_{i\to f} = \frac{\omega_{if}^3}{3\pi c^3 \hbar \varepsilon_0} |\langle f|e\mathbf{r}|i\rangle|^2, \tag{2.94}$$

where ω_{if} is the angular frequency of the emitted photon.

This chapter has provided a brief overview of the background contained within this dissertation. The next chapters present results and discussions of work that have already been published in a peer-reviewed journal, or are currently under preparation for publication.

Chapter 3

Opacity Data for Kilonova Ejecta: Os Isoelectronic Sequence[1]

The detection of a neutron star merger (NSM) (Abbott et al., 2017) event and the spectral observation of its optical and infrared emission opens up the possibility of direct interrogation of the formation site of heavy r-process elements. However, interpretation, analysis, and modeling of the observed optical/IR spectra is hindered by the sparsity of atomic opacity studies for the r-process elements, particularly beyond Mo.

In this work we focus on a small number of ion stages, with the aim of providing calculations that have been tailored for each charge state. Our goal is to provide additional large-scale, but reliable, atomic line lists for Re-Pt ($Z = 75 - 79$). Thus atomic data, such as wavelengths, spectroscopic labels, and transition probabilities are needed. For our calculation, we focus on the multiconfiguration Dirac–Hartree–Fock (MCDHF) method with Breit and quantum electrodynamics (QED) corrections as implemented in the General purpose Relativistic Atomic Structure Package (GRASP) (Jönsson, Gaigalas, Bieroń, et al., 2013; Parpia et al., 1996).

In this chapter the Os isoelectronic sequence (Os I , ..., Hg V) will be covered and a discussion of the results on the energy levels, E1 and M1 spontaneous emission rates, and expansion opacity will be given accordingly.

3.1 Computation

As it has been discussed in section 2.5.1, GRASP, the general-purpose relativistic atomic structure packages, is a code for atomic structure calculation. In this work both of these codes were used in order to check the convergence of the calculations and give an indication of the approximate uncertainties in the final results.

Based on Table 2.1, the calculation starts with nuclear data and specifying reference orbital sets. The adopted electron configurations are given in Table 3.1, which includes the ground configuration and

[1]This chapter is based on Taghadomi, Z. S., Wan, Y., Flowers, A., Stancil, P., McLaughlin, B., Bromley, S., Marler, J., Sosolik, C., & Loch, S. (2022). Relativistic atomic structure of au iv and the os isoelectronic sequence: Opacity data for kilonova ejecta. Atoms, 10(3), 94.

the configurations likely to dominate the expansion opacity under the low temperature radiation field conditions of the kilonova. This means that we focused on low-lying configurations. In the GRASP^0 calculations, we performed three different computations with increasingly larger numbers of configurations to allow for convergence checks, with the configurations for the three calculations (10, 12, and 16 configurations) being shown in the Table 3.1.

Table 3.1: GRASP2K and GRASP^0 target models adopted in the current work.

Ion/Atom	**Ground Config.**	**GRASP2K**
Os I	$[Xe]4f^{14}5d^66s^2$	$5d^8, 5d^7\{6s, 6p\}, 5d^6\{6s^2, 6s6p\}$
Ir II	$[Xe]4f^{14}5d^76s$	$5d^8, 5d^7\{6s, 6p\}, 5d^6\{6s^2, 6s6p\}$
Pt III	$[Xe]4f^{14}5d^8$	$5d^8, 5d^7\{6s, 6p\}, 5d^6\{6s^2, 6s6p\}$
Au IV	$[Xe]4f^{14}5d^8$	$5d^8, 5d^7\{6s, 6p\}, 5d^6\{6s^2, 6s6p\}$
Hg V	$[Xe]4f^{14}5d^8$	$5d^8, 5d^7\{6s, 6p\}, 5d^6\{6s^2, 6s6p\}$
	GRASP^0	
10-Config.	**12-Config.**	**16-Config.**
$5d^8$	$5d^8$	$5d^8$
$5d^7\{6s, 6p, 6d\}$	$5d^7\{6s, 6p, 6d\}$	$5d^7\{6s, 6p, 6d, 7s, 7p, 7d\}$
$5d^6\{6s^2, 6p^2, 6d^2, 6s6p, 6s6d, 6p6d\}$	$5d^6\{6s^2, 6p^2, 6d^2, 7s^2, 7p^2, 6s6p, 6s6d, 6p6d\}$	$5d^6\{6s^2, 6p^2, 6d^2, 7s^2, 7p^2, 7d^2, 6s6p, 6s6d, 6p6d\}$

It has been discussed in section 2.5.2 that in an expanding object, the frequency of the photons suffers a continuous Doppler shift with respect to the rest frame of the material. This enhanced effect of spectral lines can be taken into account as an expansion opacity. In this regard, after calculating the atomic data, the expansion opacity was calculated using Eq. 2.88.

From Kasen et al., 2013, we adopt the typical values $\rho = 10^{-13}\,\mathrm{g\,cm^{-3}}$, $t_{\mathrm{ej}} = 1$ day, and the wavelength binning $\Delta\lambda = 0.01\lambda$. Note that these expansion opacities are provided for illustrative purposes showing the use of the fundamental data and to allow us to explore the effects of the atomic data on opacities. We assume the gas to be completely composed of only one ion.

3.2 Results and discussions

We have calculated energy levels and transition probabilities for the Os isoelectronic sequence using the GRASP^0 and GRASP2K codes. The NIST Atomic Spectral Database (Kramida et al., 2018) has energies for some of the Os I (Moore, 1958) and Ir II (Van Kleef & Metsch, 1978) levels. Moreover, some calculations have been evaluated by Gillanders et al., 2021, and Ryabtsev et al., 1993 for Pt III, and the HULLAC code has been used to compute atomic data for Os I, Ir II, Pt III, and Au IV (Kato et al., 2021; Tanaka et al., 2020), for E1 transitions.

Figure 3.1 shows energy level diagrams for Figure 3.1a Os I, Figure 3.1b Ir II, Figure 3.1c Pt III, Figure 3.1d Au IV, and Figure 3.1e Hg V obtained from GRASP2K and GRASP^0 calculations using the target model in Table 3.1 as the reference configurations. Comparison is made to theoretical data calculated using the HULLAC code (Kato et al., 2021; Tanaka et al., 2020) and experimental data from the NIST database

when available (Kramida et al., 2018). Moreover, in GRASP2K we used four and five reference configurations; for four configurations the $5d^6 6s^2$ was omitted. Since the ground level is $5d^6 6s^2$ for Os I, the $5d^8$ was omitted in that case. In general, the GRASP2K energies are in better agreement with the NIST values than the GRASP^0 energies for the lower lying configurations.

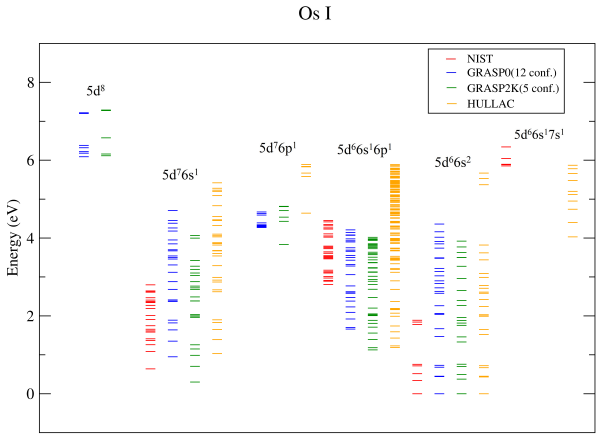

(**a**)

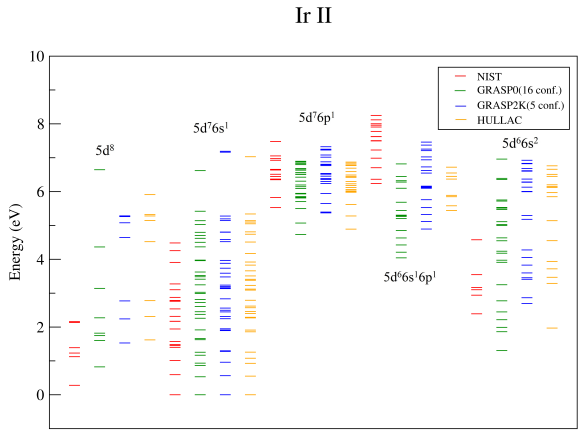

(**b**)

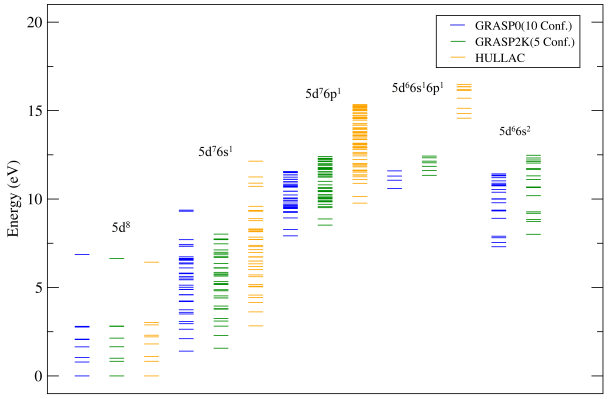

(**c**)

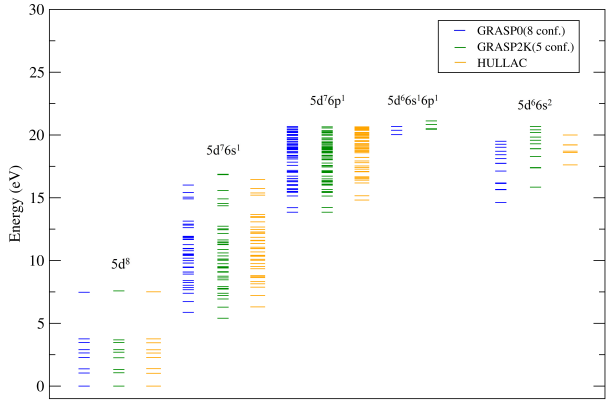

(**d**)

Figure 3.1: *Cont.*

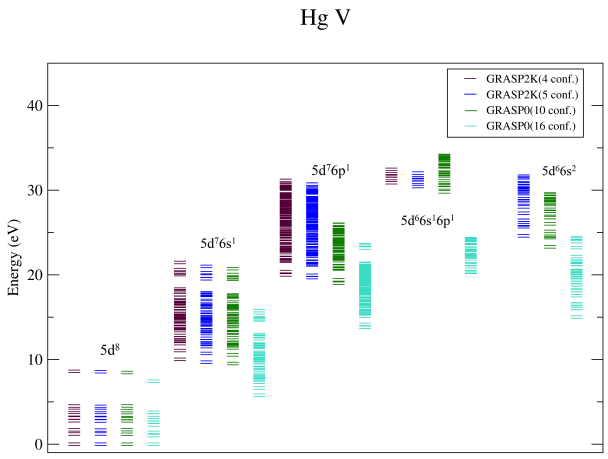

(e)

Figure 3.1: Energy level diagrams for (a) Os I, (b) Ir II, (c) Pt III, (d) Au IV, and e) Hg V, comparing our results to available NIST data (Kramida et al., 2018) and HULLAC calculations (Kato et al., 2021; Tanaka et al., 2020). Each stack of levels refers to excited states from the indicated configuration.

The energy levels of Os I and Ir II are given in Tables 3.2 and 3.3, respectively, and are compared with energies from GRASP^0, NIST (Kramida et al., 2018), HULLAC calculations (Kato et al., 2021; Tanaka et al., 2020), DESIRE (Fivet et al., 2007), and experimental studies of Ir II (Xu et al., 2007). Although levels in the ground term are in good agreement with the NIST and DESIRE data, there are deviations from the NIST database for both GRASP2K and GRASP^0 results for the higher energy levels. For Pt III, Au IV, and Hg V, literature on the energy level structures is sparse. For Pt III, a GRASP^0 calculation (Gillanders et al., 2021), and some experimental and theoretical results by Ryabtsev et al., 1993 are available. For the remainder of the Os-sequence, we are limited to comparisons between the present GRASP^0 and GRASP2K calculations.

Table 3.2: Energy levels in cm^{-1} for Os I. The GRASP^0, GRASP2K, and HULLAC calculations have been performed with configuration numbers given in parentheses.

Config.	Term	J	NIST[a]	GRASP^0(12)	GRASP^0(15)	GRASP2K(5)	HULLAC[b](8)	ΔE^c	ΔE^d	ΔE^e	ΔE^f
$5d^66s^2$	^5D	4	0.00	0.00	0.00	0.00	0.00	0.00	0.00	0.00	0.00
		2	2740.49	3668.80	3633.40	3018.98	3669.99	−928.31	−278.49	−1.19	−651.01
		3	4159.32	3561.59	3567.14	4006.11	3485.71	597.73	153.21	75.88	520.4
		1	5766.14	5463.72	5459.55	5628.12	5384.29	302.42	138.02	79.43	243.83
		0	6092.79	5914.62	5916.14	6108.75	5846.54	178.17	−15.96	68.08	262.21

Continued on next page

Table 3.2: Energy levels in cm^{-1} for Os I. The GRASP^0, GRASP2K, and HULLAC calculations have been performed with configuration numbers given in parentheses.

Config.	Term	J	NIST[a]	GRASP^0(12)	GRASP^0(15)	GRASP2K(5)	HULLAC[b](8)	ΔE^c	ΔE^d	ΔE^e	ΔE^f
$5d^7(^4F)6s$	^5F	5	5143.92	7633.67	6955.50	2416.75	8297.05	−2489.75	2727.17	−663.38	−5880.3
		4	8742.83	10,897.65	10,189.09	5683.66	11,476.98	−2154.82	3059.17	−579.33	5795.32
		2	10165.98	11,856.53	11,599.45	9282.52	14,725.19	−1690.55	883.46	−2868.66	−5442.67
		3	11,378.00	13,234.12	12,590.30	7963.28	13,340.77	−1856.12	3414.72	−106.65	−5377.49
		1	13,020.07	15,248.91	14,621.28	10,147.57	15,321.69	−2228.84	2872.50	−72.78	−5174.12
$5d^7(^4F)6s$	^3F	4	11,030.58	13,462.15	13,181.68	15,942.40	24,083.44	−2431.57	−4911.82	−10,621.29	−8141.04
		2	12,774.38	14,693.95	14,075.83	26,417.68	21,569.16	−1919.57	−13,643.3	−6875.21	4848.52
		3	14,091.37	16,657.69	16,183.66	20,061.03	21,099.31	−2566.32	−5969.66	−4441.62	−1038.28
$5d^66s^2$	^3H	5	14,338.99	16,532.24	16,480.73	18,298.92	16,145.83	−2193.25	−3959.93	386.41	2153.09
		4	14,848.05	18,223.93	17,245.52	21,435.88	13,304.98	−3375.88	−6587.83	4918.95	8130.9
		6	14,852.33	16,646.16	16,621.41	15,797.42	16,351.83	1793.83	−945.09	294.33	−554.41
$5d^7(^4P)6s$	^5P	1	–	19,123.80	18,766.30	16,269.95	23,138.85	–	–	−4015.05	−6868.9
		2	–	16,479.35	16,008.31	16,391.99	26,552.53	–	–	−10,073.18	−10,160.54
		3	15,390.76	20,837.23	20,665.70	15,827.03	27,092.17	−5446.47	−436.27	−6254.94	−11,265.14
$5d^66s(^6D)6p$	$^7D^o$	1	–	18,018.56	18,001.46	13,798.29	14,018.25	–	–	4000.31	−219.96
		4	22,615.69	13,418.13	13,403.97	9079.96	9597.03	9197.65	13,517.73	3821.10	−517.07
		5	23,462.90	13,730.69	13,713.74	9529.18	9941.73	9732.21	13,933.72	3788.96	−412.55
		3	25,012.93	15,506.13	15,491.82	11,228.11	11,573.36	9506.80	13,784.82	3932.77	−345.25
		2	25,275.42	16,828.11	16,812.03	12,571.95	12,853.23	8447.31	12,703.47	3974.88	−281.28
$5d^66s(^6D)6p$	$^7P^o$	2	–	21,136.37	21,120.13	21,650.15	23,418.79	–	–	−2282.42	−1768.64
		4	28,331.77	19,935.86	19,919.65	–	19,087.33	8395.91	–	848.53	–
		3	28,371.68	20,829.29	20,812.61	19,925.91	21,615.17	7542.39	8445.77	−785.88	−1689.26
$5d^66s(^6D)6p$	$^7F^o$	5	–	20,840.01	20,820.07	16,297.80	17,640.90	–	–	3199.11	−1343.1
		2	–	28,666.02	26,452.48	16,527.91	17,633.15	–	–	11,032.87	−1105.24
		4	–	22,321.80	22,302.33	15,195.33	16,686.90	–	–	5634.9	−1491.57
		1	–	21,167.55	21,152.65	16,539.25	17,589.88	–	–	3577.67	−1050.63
		3	–	24,695.57	24,674.47	16,189.48	17,430.42	–	–	7265.15	−1240.94
		0	–	21,017.96	21,003.91	16,335.38	17,416.14	–	–	3601.82	−1080.76
		6	29,099.41	19,162.43	19,140.88	14,586.66	16,014.09	9936.98	14,512.75	3148.34	−1427.43

[a] Atomic energy levels from the NIST database (Kramida et al., 2018; Moore, 1958).

[b] Atomic energy levels from Tanaka et al., 2020 and Kato et al., 2021 using the HULLAC code. [c] Energy difference between NIST and GRASP^0(12).

[d] Energy difference between NIST and GRASP2K.

[e] Energy difference between GRASP^0(12) and HULLAC.

[f] Energy difference between GRASP2K and HULLAC.

Table 3.3: Energy levels in cm^{-1} for Ir II. The GRASP^0, GRASP2K, and HULLAC calculations have been performed with configuration numbers given in parentheses.

Config.	Term	J	NIST[a]	DESIRE[b]	GRASP^0 (10)	GRASP^0 (16)	GRASP2K (5)	HULLAC[c] (7)	ΔE^d	ΔE^e	ΔE^f	ΔE^g
$5d^7(^4F)6s$	^5F	5	0.00	0.00	0.00	0.00	0.00	0.00	0.00	0.00	0.00	0.00
		4	4787.93	4692.00	4392.63	4297.37	4544.01	4413.33	395.30	243.92	−20.7	130.68
		3	8186.96	8277.00	7578.85	7540.14	7740.31	7511.43	608.11	446.65	67.42	228.88
		2	11,307.32	11,374.00	8400.55	9412.94	10,331.82	8731.69	2906.77	975.50	−331.14	1600.13
		1	11,957.70	12,103.00	10,226.85	10,127.30	10,466.53	10,173.43	1730.85	1511.17	53.42	293.10
$5d^8$	^3F	4	2262.75	2268.00	9786.89	6657.87	12,345.86	13,102.15	−7524.14	−1083.11	−3315.26	−756.29
		3	9927.83	9838.00	14,900.59	12,920.44	18,062.12	18,636.08	−4972.76	−8134.17	−3735.49	−573.96
		2	17,413.24	17,692.00	9910.22	14,098.24	22,352.96	22,390.63	7503.02	−4939.72	−12,480.41	−37.67
$5d^8$	^3P	2	3090.17	3266.00	16399.17	16,057.24	–	36,459.05	−13,309.00	–	−20,059.88	–
		1	9062.14	9014.00	18553.06	13,368.85	42,438.61	42,915.57	−9490.92	−33,376.47	−24,362.51	−476.96
		0	11,211.93	11,134.00	16,812.57	14,685.56	40,965.51	41,500.78	−5600.64	−29,753.58	−24,688.21	−535.27
$5d^8$	^1D	2	8975.01	8867.00	18,023.33	18,327.27	–	47,691.11	−9048.32	–	−29,667.78	–
$5d^7(^4F)6s$	^3F	4	11,719.09	11,639.00	14,183.47	10,512.92	15,417.13	10,181.02	−2464.38	−3698.04	4002.45	5236.11
		3	17,499.29	17,499.00	15,542.50	15,031.34	20,656.18	20,745.07	1956.79	−3156.89	−5202.57	−88.89
		2	22,467.78	22,351.00	20,903.68	19,787.66	26,129.89	19,864.06	1564.10	−3662.11	1039.62	6265.83
$5d^7(^4P)6s$	^5P	3	12,714.64	12,808.00	18,881.64	15,462.13	15,719.57	15,417.58	−6167.00	−3004.93	3464.06	301.99
		2	15,676.35	15,594.00	21,657.44	22,376.16	18,121.80	18,348.06	−5999.09	−2445.45	3309.38	−226.26
		1	18,676.50	18,604.00	18,553.06	17,878.59	22,858.00	15,037.46	123.44	−4181.50	3515.6	7550.54
$5d^8$	^1G	4	17,210.14	17,333.99	15,079.92	13,113.93	37,427.14	42,637.17	2130.22	123.44	−27,557.25	−5210.03
$5d^7(^2G)6s$	^3G	5	17,477.92	17,440.00	19,332.94	19,154.40	19,729.27	19,365.93	−1855.02	−2251.35	−32.99	363.34

Continued on next page

Table 3.3: Energy levels in cm^{-1} for Ir II. The GRASP^0, GRASP2K, and HULLAC calculations have been performed with configuration numbers given in parentheses.

Config.	Term	J	NIST[a]	DESIRE[b]	GRASP^0 (10)	GRASP^0 (16)	GRASP2K (5)	HULLAC[c] (7)	ΔE^d	ΔE^e	ΔE^f	ΔE^g
		4	20,294.23	20,317.00	21,701.91	21,012.21	–	21,113.67	−1407.68	–	588.24	–
		3	23,195.21	23,122.00	20,305.01	18,229.64	25,481.87	24,945.96	2890.20	−2286.66	−4640.95	535.91
$5d^7(^4P)6s$	^3P	2	18,944.93	18,970.00	25,459.52	25,340.26	–	26,027.90	−6550.59	–	−568.38	–
		1	20,440.66	20,494.00	23,091.32	21,999.04	25,764.70	22,409.70	−3650.66	−5324.04	681.62	3355.00
$5d^66s^2$	^5D	4	19,279.05	19,217.00	24,103.48	22,690.11	21,725.60	15,855.13	−4824.43	−2446.55	8248.35	5870.47
		3	23,727.67	23,681.00	24,841.36	24,421.62	27,514.10	26,549.94	−1113.69	−3786.43	−1708.58	964.16
		2	25,563.72	25,484.00	25,459.52	29,233.36	27,861.34	30,068.05	68.20	−2297.62	−4608.53	−2206.71
		1	28,600.35	28,725.00	25,531.45	24,137.33	32,703.21	31,786.78	3068.90	−4102.86	−6255.33	916.43
$5d^7(^2H)6s$	^3H	6	22,267.00	22,436.00	24,404.96	24,200.01	75,768.56	24,819.68	−2137.96	−53,501.65	−414.72	50,948.88
		5	25,011.15	24,938.00	26,557.89	26,192.99	77,210.42	36,343.71	−1546.74	−52,199.27	−9785.82	40,866.71
$5d^7(^2D2)6s$	^3D	3	26,391.40	26,310.00	27,838.83	27,527.03	28,943.95	28,333.41	−1447.43	−2552.55	−494.58	610.54
$5d^7(^2F)6s$	^3F	3	31,518.56	31,445.00	35,297.24	29,233.36	38,706.84	38,230.60	−3778.68	−7188.28	−2933.36	476.24
$5d^7(^2G)6s$	^1G	4	34,319.48	–	28,544.96	26,202.92	25,453.56	25,167.13	5774.52	8865.92	3377.83	286.43
$5d^7(^2P)6s$	^3P	2	36,160.59	–	27,438.80	32,071.58	43,505.18	38,790.16	8721.79	−7344.59	−11,351.36	4715.02
$5d^66s^2$	^3H	5	36,916.82	36,960.00	32,820.88	32,051.19	42,698.55	41,484.66	4095.94	−5781.73	−8663.78	1213.89

[a] Atomic energy levels, NIST database (Kramida et al., 2018; Van Kleef & Metsch, 1978).

[b] Atomic energy levels, DESIRE database (Fivet et al., 2007; Xu et al., 2007), Relativistic Hartree–Fock plus core polarization (HFR + CP).

[c] Atomic energy levels from Tanaka et al., 2020 and Kato et al., 2021 using the HULLAC code.

[d] Energy difference between NIST and GRASP^0(10).

[e] Energy difference between NIST and GRASP2K.

[f] Energy difference between GRASP^0(10) and HULLAC.

[g] Energy difference between GRASP2K and HULLAC.

Table 3.4 gives as an example the convergence of energy eigenvalues for levels in the ground term of each of the considered ions from the current calculations. Here we give energies for all GRASP^0 and

GRASP2K results. In all cases, the ground level is correctly predicted and the ordering of J-levels is consistent.

Computed energies for low-lying levels of Pt III are compared in Table 3.5 from our GRASP2K(5) calculations to those of Gillanders et al., 2021, Ryabtsev et al., 1993, and the HULLAC calculations (Kato et al., 2021; Tanaka et al., 2020), while comparisons to the two M1 transition probabilities given in Gillanders et al., 2021 are also shown. There is general agreement amongst the calculations except for the energy of the $^5D_4$ state, and our M1 values are 36–52% smaller than those computed by Gillanders et al., 2021.

Table 3.4: Energy comparison of GRASP2K and GRASP^0 with different configurations as given in parentheses for the ground term.

Os I						
Configuration	Term	J	GRASP2K(4)	GRASP2K(5)	GRASP^0(12)	GRASP^0(15)
$5d^6 6s^2$	^5D	4	0.00	0.00	0.00	0.00
		2	3515.19	3018.98	3668.80	3633.40
		3	3854.65	4006.11	3561.59	3567.14
		1	5720.24	5628.12	5463.72	5459.55
		0	6216.58	6108.75	5914.62	5916.14
Ir II						
Configuration	Term	J	GRASP2K(4)	GRASP2K(5)	GRASP^0(10)	GRASP^0(16)
$5d^7(^4F)6s$	^5F	5	0.00	0.00	0.00	0.00
		4	4732.38	4544.01	4392.63	4297.37
		3	8037.62	7740.31	7578.85	7540.14
		2	9620.11	10,331.82	8400.55	9412.94
		1	10,855.25	10,466.53	10,226.85	10,127.30
Pt III						
Configuration	Term	J	GRASP2K(4)	GRASP2K(5)	GRASP^0(10)	GRASP^0(16)
$5d^8$	^3F	4	0.00	0.00	0.00	0.00
		3	8388.75	8089.99	8436.73	8618.15
		2	14,123.55	13,312.88	13,262.17	13,903.07
Au IV						
Configuration	Term	J	GRASP2K(4)	GRASP2K(5)	GRASP^0(8)	GRASP^0(16)
$5d^8$	^3F	4	0.00	0.00	0.00	0.00
		3	10,945.77	10,689.7	11,094.69	11,189.87
Hg V						
Configuration	Term	J	GRASP2K(4)	GRASP2K(5)	GRASP^0(10)	GRASP^0(16)
$5d^8$	^3F	4	0.00	0.00	0.00	0.00
		3	13,677.30	13,440.74	13,827.29	11,189.87

Transition probabilities for E1 vs. wavelength are plotted in Figure 3.2 for Figure 3.2a Os I, Figure 3.2b Ir II, Figure 3.2c Pt III, Figure 3.2d Au IV, and Figure 3.2e Hg V. The strongest transitions occur at shorter wavelengths, with most of them being shorter than 200 nm. We note that, while the bulk of the transitions are at UV wavelengths, the density of lines may make this wavelength range difficult to use for line identification. Observing at longer wavelengths, where the lines are more sparse, may provide opportunities for more definitive identification of the charge state of the ion. The weighted transition probabilities (gA, where $g = 2J + 1$), are compared with HULLAC calculations (Kato et al., 2021; Tanaka et al., 2020) and DESIRE (Fivet et al., 2007) for Os I (Quinet et al., 2006) and Ir II (Xu et al., 2007) in Tables 3.6 and 3.7, respectively. There is reasonable agreement between GRASP2K and DESIRE, and GRASP2K and HULLAC calculations. The average percent difference of Os I is 113%, and 126%, and the average percent difference of Ir II is 63.5%, and 82.7%, between GRASP2K and DESIRE, and GRASP2K and HULLAC calculations, respectively. To illustrate the convergence of the A-values with calculation size, an electron dipole transition present in all ions was selected. The A-value for the various calculations is plotted in Figure 3.3, showing a reasonable convergence for all members of the iso-electronic sequence. The reason for choosing $5d^8\ ^3F \rightarrow 5d^7(^2H_3)6p\ ^3G$ transition is that for most of the ions in this work, this transition has the strongest A-value, as shown in Table 3.8. DESIRE does not provide this transition. Increasing the number of configurations was observed to have a minor impact on the transition rates of the most highly ionized systems in the Os-sequence. However, near-neutral systems (e.g., Ir II) show slower convergence with respect to increasing numbers of configurations.

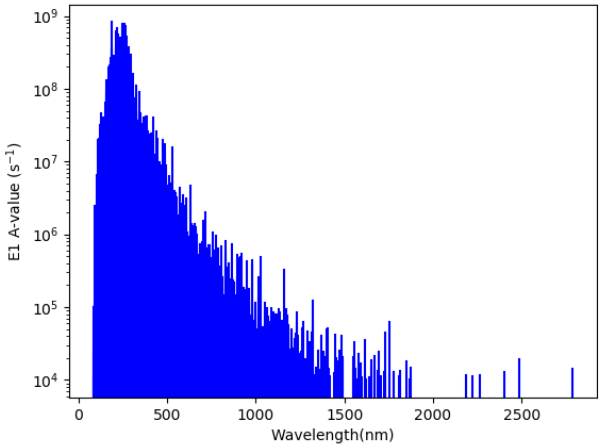

(**a**) Os I

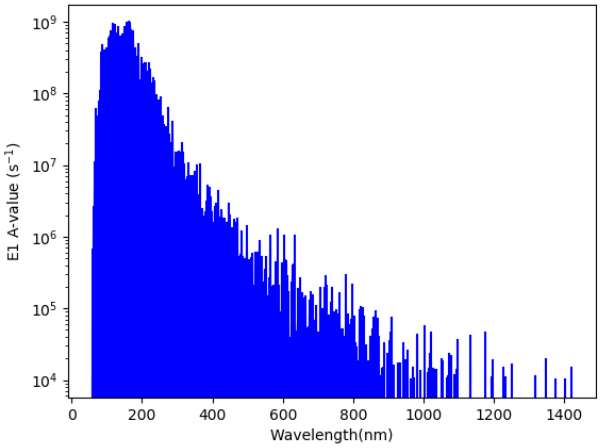

(**b**) Ir II

Figure 3.2: *Cont.*

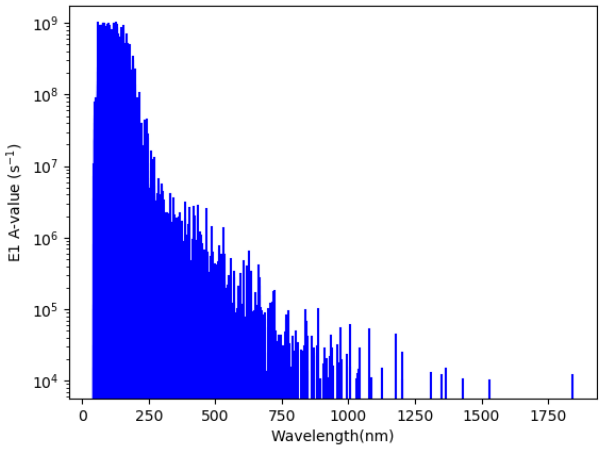

(**c**) Pt III

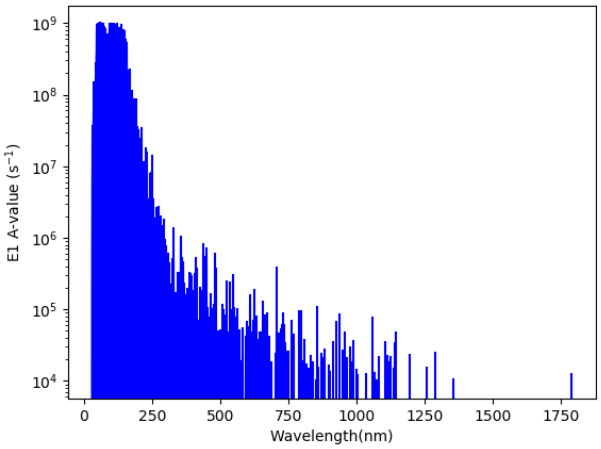

(**d**) Au IV

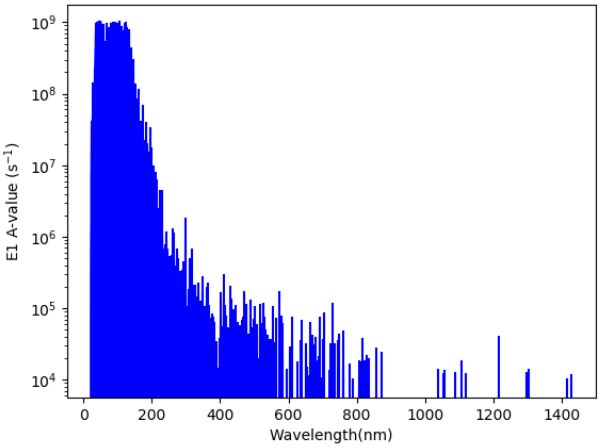

(**e**) Hg V

Figure 3.2: Transition probabilities (E1) for (a) Os I, (b) Ir II, (c) Pt III, (d) Au IV, and (e) Hg V obtained from GRASP2K calculations.

Table 3.5: Energy levels in cm^{-1} and M1 transition for Pt III. The GRASP2K and HULLAC calculations have been performed with configuration numbers given in parentheses.

Configuration	Term	J	Gillanders[a]	GRASP2K(5)	HULLAC[b](5)	E^*_{exp}	E^*_{th}	ΔE^c	ΔE^d
$5d^8$	^3F	4	0.00	0.00	0.00	0.00	-69	0.00	0.00
		3	9159.88	8089.99	8888.95	9751.7	9784	−1069.89	−798.96
		2	14,798.78	13,312.88	14,596.35	14,171.9	14,226	−1485.90	−1283.47
$5d^8$	^1D	2	6776.39	6680.22	6683.36	5293.1	5351	−96.17	−3.14
$5d^6 6s^2$	^5D	4	79,582.08	64,561.61	–	–	67,965	−15,020.47	–

					M1 A-value (s^{-1})		
	Lower Level	J	Upper Level	J	Gillanders [a]	GRASP2K(5)	$\%D_i$
	$5d^8\ ^3F$	4	$5d^8\ ^3F$	3	19.30	13.38	36.23
	$5d^8\ ^1D$	2	$5d^8\ ^3F$	2	8.19	4.80	52.19

* Experimental and theoretical energy levels by Ryabtsev et al., 1993.
[a] The GRASP^0 calculation performed by Gillanders et al., 2021.
[b] Atomic energy levels from Tanaka et al., 2020 and Kato et al., 2021 using the HULLAC code.
[c] Energy difference between GRASP2K and Gillanders et al., 2021.
[d] Energy difference between GRASP2K and HULLAC.
$\%D_i$ percent difference of GRASP2K and Gillanders et al., 2021.

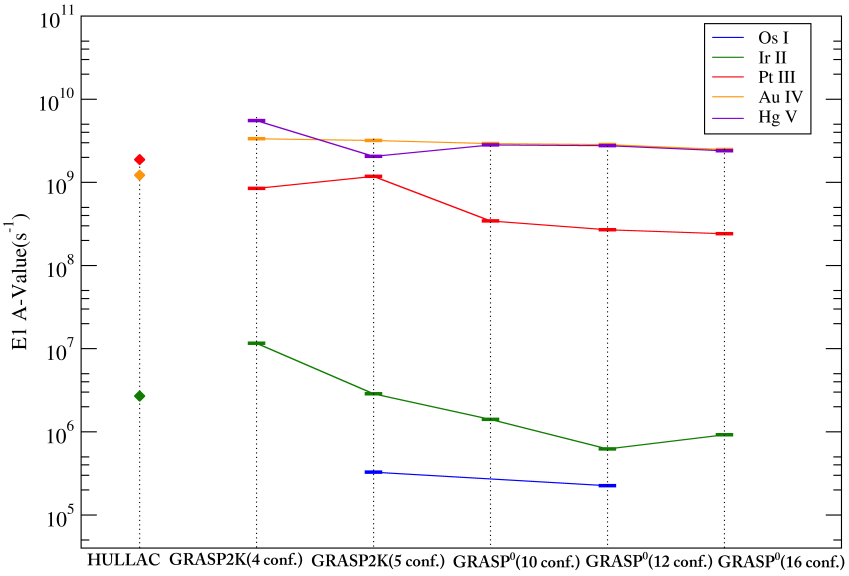

Figure 3.3: Convergence of E1 transition probability for different methods and numbers of configurations for the $5d^8\ ^3F \rightarrow 5d^7(^2H_3)6p\ ^3G$ transition.

Table 3.6: Weighed transition probabilities (gA-values) for Os I.

				gA(s^{-1})				
Lower Level	J	Upper Level	J	DESIRE[a]	GRASP2K	HULLAC[b]	$\%D_i$ [c]	$\%D_j$ [d]
$5d^6 6s^2\ ^5D_4$	4	$5d^6 6s(^6D)6p\ ^5F_5$	5	4.35×10^8	4.41×10^8	1.16×10^8	1.37	116.70
$5d^6 6s^2\ ^5D_4$	4	$5d^6 6s(^6D)6p\ ^7D_5$	5	1.35×10^7	8.96×10^5	6.51×10^8	175.10	199.45
$5d^6 6s^2\ ^5D_4$	4	$5d^6 6s(^4D)6p\ ^3F_4$	4	1.34×10^8	1.97×10^8	1.63×10^8	38.07	18.89
$5d^6 6s^2\ ^5D_4$	4	$5d^6 6s(^4D)6p\ ^5D_4$	4	2.44×10^8	6.58×10^8	4.23×10^8	91.80	43.48
$5d^6 6s^2\ ^5D_4$	4	$5d^6 6s(^6D)6p\ ^5D_4$	4	8.44×10^7	2.31×10^8	2.16×10^8	92.96	6.71
$5d^6 6s^2\ ^5D_4$	4	$5d^6 6s(^6D)6p\ ^5F_4$	4	2.06×10^7	6.49×10^5	2.58×10^7	187.78	190.18
$5d^6 6s^2\ ^5D_4$	4	$5d^6 6s(^6D)6p\ ^7F_4$	4	2.78×10^8	1.41×10^6	7.69×10^7	197.98	192.80
$5d^6 6s^2\ ^5D_4$	4	$5d^6 6s(^6D)6p\ ^7D_4$	4	2.17×10^7	7.60×10^5	3.17×10^4	186.46	183.98
$5d^6 6s^2\ ^5D_4$	4	$5d^7(^4F)6p\ ^3D_3$	3	3.97×10^8	1.20×10^6	2.96×10^7	198.79	184.42
$5d^6 6s^2\ ^5D_4$	4	$5d^6 6s(^6D)6p\ ^5P_3$	3	1.38×10^8	8.41×10^7	9.97×10^7	48.54	16.97
$5d^6 6s^2\ ^5D_4$	4	$5d^6 6s(^6D)6p\ ^7P_3$	3	4.55×10^6	6.08×10^5	3.41×10^6	152.85	139.47
$5d^6 6s^2\ ^5D_2$	2	$5d^7(^4F)6p\ ^3D_3$	3	4.29×10^8	2.76×10^7	8.22×10^7	175.82	99.45
$5d^6 6s^2\ ^5D_2$	2	$5d^6 6s(^6D)6p\ ^5P_3$	3	5.69×10^7	1.39×10^7	9.67×10^7	121.47	149.73
$5d^6 6s^2\ ^5D_3$	3	$5d^7(^4F)6p\ ^3D_3$	3	3.35×10^7	5.38×10^6	2.99×10^8	144.65	192.93
$5d^6 6s^2\ ^5D_3$	3	$5d^6 6s(^6D)6p\ ^5P_3$	3	5.39×10^6	5.99×10^7	4.80×10^7	166.98	22.06
$5d^6 6s^2\ ^5D_3$	3	$5d^6 6s(^6D)6p\ ^7P_3$	3	3.85×10^6	6.41×10^5	1.55×10^8	142.91	198.35
$5d^6 6s^2\ ^5D_3$	3	$5d^6 6s(^4D)6p\ ^3F_4$	4	8.05×10^7	3.11×10^7	1.04×10^7	88.53	99.76
$5d^6 6s^2\ ^5D_3$	3	$5d^6 6s(^4D)6p\ ^5D_4$	4	3.99×10^7	7.36×10^6	2.76×10^6	137.71	90.91
$5d^6 6s^2\ ^5D_3$	3	$5d^6 6s(^6D)6p\ ^5D_4$	4	8.01×10^6	3.93×10^6	4.66×10^6	68.34	16.70
$5d^6 6s^2\ ^5D_3$	3	$5d^6 6s(^6D)6p\ ^5F_4$	4	7.20×10^7	1.80×10^8	1.46×10^8	85.71	20.86
$5d^6 6s^2\ ^5D_3$	3	$5d^6 6s(^6D)6p\ ^7F_4$	4	1.96×10^7	2.27×10^6	1.04×10^7	158.48	128.33
$5d^6 6s^2\ ^5D_3$	3	$5d^6 6s(^6D)6p\ ^7D_4$	4	9.00×10^4	1.82×10^3	4.65×10^5	192.07	198.44
$5d^7(^4F)6s\ ^5F_4$	4	$5d^7(^4F)6p\ ^3D_3$	3	3.65×10^7	7.47×10^7	9.45×10^7	68.70	23.40
$5d^7(^4F)6s\ ^5F_4$	4	$5d^6 6s(^6D)6p\ ^5P_3$	3	1.18×10^7	4.81×10^5	7.17×10^5	184.33	39.40
$5d^7(^4F)6s\ ^5F_4$	4	$5d^6 6s(^6D)6p^7P_3$	3	9.80×10^5	6.49×10^3	2.31×10^7	197.37	199.89
$5d^7(^4F)6s\ ^5F_4$	4	$5d^6 6s(^4D)6p^3F_4$	4	2.44×10^7	4.63×10^7	5.51×10^7	61.95	17.36
$5d^7(^4F)6s\ ^5F_4$	4	$5d^6 6s(^4D)6p^5D_4$	4	2.48×10^7	2.56×10^7	3.17×10^5	3.17	195.11
$5d^7(^4F)6s\ ^5F_4$	4	$5d^6 6s(^6D)6p^5D_4$	4	5.62×10^7	7.59×10^7	7.99×10^6	29.83	161.90
$5d^7(^4F)6s\ ^5F_4$	4	$5d^6 6s(^6D)6p^5F_4$	4	6.48×10^6	3.45×10^6	1.72×10^5	61.03	181.00
$5d^7(^4F)6s\ ^5F_4$	4	$5d^6 6s(^6D)6p^7F_4$	4	9.00×10^4	8.75×10^4	5.45×10^6	2.82	193.68
$5d^7(^4F)6s\ ^3F_4$	4	$5d^7(^4F)6p^3D_3$	3	1.31×10^8	2.03×10^8	4.869×10^7	43.11	122.62
$5d^7(^4F)6s\ ^3F_4$	4	$5d^6 6s(^6D)6p^5F_4$	4	4.50×10^5	3.22×10^4	2.97×10^5	173.29	160.87
$5d^7(^4F)6s\ ^3F_4$	4	$5d^6 6s(^6D)6p^5F_5$	5	1.32×10^6	1.43×10^4	1.57×10^6	195.71	196.39
$5d^7(^4F)6s^5F_3$	3	$5d^7(^4F)6p^3D_3$	3	4.96×10^7	7.12×10^7	2.05×10^7	35.76	110.58

Continued on next page

Table 3.6: Weighed transition probabilities (gA-values) for Os I.

				gA(s^{-1})				
Lower Level	J	Upper Level	J	DESIRE[a]	GRASP2K	HULLAC[b]	$\%D_i$ [c]	$\%D_j$ [d]
$5d^7(^4F)6s^5F_3$	3	$5d^66s(^6D)6p^5P_3$	3	3.64×10^6	2.48×10^6	2.73×10^6	37.91	166.69
$5d^7(^4F)6s^5F_3$	3	$5d^66s(^6D)6p^7P_3$	3	6.30×10^5	4.50×10^4	4.64×10^5	173.33	164.64
$5d^7(^4F)6s^5F_3$	3	$5d^66s(^4D)6p^3F_4$	4	9.54×10^6	7.02×10^6	2.47×10^6	30.43	95.89
$5d^7(^4F)6s^5F_3$	3	$5d^66s(^4D)6p^5D_4$	4	1.26×10^6	2.00×10^7	1.17×10^4	176.29	199.77
$5d^7(^4F)6s^5F_3$	3	$5d^66s(^6D)6p^5D_4$	4	5.40×10^6	9.73×10^5	5.61×10^6	138.93	140.88
$5d^7(^4F)6s^5F_3$	3	$5d^66s(^6D)6p^5F_4$	4	2.70×10^5	1.84×10^5	2.50×10^6	37.88	172.58

[a] gA-values, DESIRE database (Fivet et al., 2007; Quinet et al., 2006).

[b] gA-values from Tanaka et al., 2020 and Kato et al., 2021 using HULLAC.

[c] $\%D_i$ percent difference of GRASP2K and DESIRE.

[d] $\%D_j$ percent difference of GRASP2K and HULLAC.

Table 3.7: Weighed transition probabilities (gA-values) for Ir II.

				gA(s^{-1})				
Lower Level	J	Upper Level	J	DESIRE[a]	GRASP2K	HULLAC[b]	$\%D_i$ [c]	$\%D_j$ [d]
$5d^7(^4F)6s\,^5F$	5	$5d^7(^4F)6p$	4	2.85×10^8	2.55×10^8	1.75×10^8	11.11	37.21
$5d^7(^4F)6s\,^5F$	5	$5d^7(^4F)6p$	4	5.10×10^7	6.81×10^7	4.80×10^7	28.71	34.62
$5d^7(^4F)6s\,^5F$	5	$5d^6(^5D)6s6p$	4	1.28×10^8	9.03×10^7	1.96×10^8	34.54	73.84
$5d^7(^4F)6s\,^5F$	5	$5d^7(^4F)6p$	4	1.60×10^9	1.46×10^9	1.37×10^9	9.15	6.21
$5d^7(^4F)6s\,^5F$	5	$5d^7(^4F)6p$	5	1.33×10^9	2.93×10^9	7.31×10^8	75.12	120.13
$5d^7(^4F)6s\,^5F$	5	$5d^6(^5D)6s6p$	5	1.28×10^8	7.82×10^8	2.23×10^8	143.74	111.24
$5d^7(^4F)6s\,^5F$	5	$5d^7(^4F)6p$	5	1.90×10^9	2.93×10^9	2.38×10^9	42.65	20.72
$5d^8\,^3F$	4	$5d^7(^4F)6p$	3	1.49×10^7	5.76×10^7	7.40×10^7	117.79	24.92
$5d^8\,^3F$	4	$5d^7(^4F)6p$	3	1.17×10^7	9.00×10^7	1.67×10^8	153.98	59.92
$5d^8\,^3F$	4	$5d^7(^4F)6p$	4	1.34×10^8	7.94×10^8	6.58×10^7	142.24	169.39
$5d^8\,^3F$	4	$5d^6(^5D)6s6p$	4	3.80×10^6	6.60×10^7	6.09×10^6	178.22	166.21
$5d^8\,^3F$	4	$5d^7(^4F)6p$	5	2.03×10^8	3.01×10^8	6.99×10^8	38.89	79.60
$5d^8\,^3F$	4	$5d^7(^4F)6p$	5	1.17×10^7	2.55×10^7	8.03×10^7	74.19	103.59
$5d^7(^4F)6s\,^5F$	4	$5d^7(^4F)6p$	5	1.78×10^9	1.22×10^9	1.65×10^9	37.33	29.96
$5d^7(^4F)6s\,^5F$	4	$5d^6(^5D)6s6p$	5	4.50×10^6	5.11×10^8	3.01×10^4	196.51	199.98
$5d^7(^4F)6s\,^5F$	4	$5d^7(^4F)6p$	4	2.49×10^8	1.27×10^8	2.35×10^7	64.89	137.54
$5d^7(^4F)6s\,^5F$	4	$5d^7(^4F)6p$	4	1.59×10^9	1.70×10^9	2.21×10^9	6.69	26.09
$5d^7(^4F)6s\,^5F$	4	$5d^6(^5D)6s6p$	4	6.63×10^7	5.86×10^7	1.78×10^8	12.33	100.93

Continued on next page

Table 3.7: Weighed transition probabilities (gA-values) for Ir II.

				gA(s^{-1})				
Lower Level	J	Upper Level	J	DESIRE[a]	GRASP2K	HULLAC[b]	$\%D_i$ [c]	$\%D_j$ [d]
$5d^7(^4F)6s\,^5F$	4	$5d^7(^4F)6p$	4	1.48×10^8	1.02×10^8	8.01×10^7	36.80	24.05
$5d^7(^4F)6s\,^5F$	4	$5d^7(^4F)6p$	3	3.32×10^7	3.98×10^7	1.96×10^6	18.08	181.23
$5d^7(^4F)6s\,^5F$	4	$5d^6(^5D)6s6p$	3	1.81×10^8	3.85×10^8	2.70×10^8	72.08	35.11
$5d^7(^4F)6s\,^5F$	4	$5d^7(^4F)6p$	3	1.08×10^9	9.78×10^8	4.50×10^7	9.91	182.40
$5d^7(^4F)6s\,^5F$	3	$5d^7(^4F)6p$	4	1.89×10^8	2.08×10^8	4.03×10^8	9.57	63.83
$5d^7(^4F)6s\,^5F$	3	$5d^7(^4F)6p$	4	2.37×10^8	1.24×10^8	2.50×10^8	62.60	67.38
$5d^7(^4F)6s\,^5F$	3	$5d^6(^5D)6s6p$	4	5.00×10^6	3.54×10^7	2.30×10^8	150.49	146.65
$5d^7(^4F)6s\,^5F$	3	$5d^7(^4F)6p$	3	5.98×10^7	2.17×10^7	1.90×10^7	93.50	13.27
$5d^7(^4F)6s\,^5F$	3	$5d^6(^5D)6s6p$	3	1.98×10^8	1.77×10^8	8.06×10^7	11.20	74.84
$5d^7(^4F)6s\,^5F$	3	$5d^7(^4F)6p$	3	4.52×10^8	1.15×10^8	1.15×10^8	118.87	0.00
$5d^7(^4F)6s\,^5F$	3	$5d^7(^4F)6p$	2	1.17×10^8	1.94×10^8	2.10×10^8	49.52	7.92
$5d^7(^4F)6s\,^5F$	3	$5d^6(^5D)6s6p$	2	2.00×10^7	3.89×10^7	9.46×10^6	64.18	121.75
$5d^7(^4F)6s\,^5F$	3	$5d^7(^4F)6p$	2	3.61×10^8	3.38×10^8	1.82×10^8	6.58	60.00
$5d^7(^4F)6s\,^5F$	3	$5d^7(^4F)6p$	2	2.19×10^8	5.02×10^8	6.23×10^8	78.50	21.51
$5d^7(^4F)6s\,^5F$	2	$5d^7(^4F)6p$	3	2.00×10^8	3.36×10^8	9.88×10^7	50.75	109.11
$5d^7(^4F)6s\,^5F$	2	$5d^6(^5D)6s6p$	3	8.50×10^6	7.84×10^6	1.04×10^7	8.08	28.07
$5d^7(^4F)6s\,^5F$	2	$5d^7(^4F)6p$	3	5.56×10^7	1.29×10^7	1.67×10^9	124.67	196.93
$5d^7(^4F)6s\,^5F$	2	$5d^7(^4F)6p$	2	1.48×10^8	1.87×10^8	1.63×10^8	23.28	13.71
$5d^7(^4F)6s\,^5F$	2	$5d^6(^5D)6s6p$	2	1.16×10^8	6.63×10^8	9.31×10^6	140.44	194.46
$5d^7(^4F)6s\,^5F$	2	$5d^7(^4F)6p$	2	5.73×10^7	9.87×10^7	1.84×10^4	53.08	199.92
$5d^7(^4F)6s\,^5F$	2	$5d^7(^4F)6p$	2	1.22×10^8	2.13×10^8	2.91×10^8	54.33	30.95
$5d^7(^2P)6s\,^3P$	1	$5d^7(^4F)6p$	2	2.42×10^8	2.18×10^8	3.28×10^8	10.43	40.29
$5d^7(^2P)6s\,^3P$	1	$5d^7(^4F)6p$	2	2.98×10^7	2.10×10^7	5.26×10^6	34.65	119.88
$5d^7(^2P)6s\,^3P$	1	$5d^7(^4F)6p$	1	2.65×10^7	1.33×10^7	1.23×10^7	66.33	7.81
$5d^7(^2P)6s\,^3P$	1	$5d^7(^4F)6p$	1	8.55×10^7	1.05×10^8	6.92×10^7	20.47	41.10
$5d^7(^2P)6s\,^3P$	1	$5d^7(^4F)6p$	0	1.47×10^8	2.61×10^8	3.16×10^7	55.88	156.80

[a] gA-values, DESIRE database (Fivet et al., 2007; Xu et al., 2007).

[b] gA-values from Tanaka et al., 2020 and Kato et al., 2021 using HULLAC.

[c] $\%D_i$ percent difference of GRASP2K and DESIRE.

[d] $\%D_J$ percent difference of GRASP2K and HULLAC.

The temperature in neutron star merger ejecta is approximately 5000 K, and cooling off to 1000 K at later times. Therefore, as an illustration, the LTE spectra for Os I, Ir II, Pt III, Au IV, and Hg V at 5000 K are computed and displayed for E1 transitions in Figure 3.4. The emission lines are very dense in the UV

and visible, but become less crowded as the wavelength increases into the IR. Moreover, wavelengths of the three most intense lines for each ion are represented in Table 3.8.

Table 3.8: Wavelength of the most intense lines from LTE spectra at 5000 K using GRASP2K calculations.

Os I		
Lower Level	Upper Level	λ(nm)
$5d^6(^5D_4)6s^2\ ^5D$	$5d^6(^5D_4)6s(^4D)6p\ ^5F$	226.43
$5d^6(^5D_4)6s^2\ ^5D$	$5d^7(^4F_3)6p\ ^5G$	213.48
$5d^6(^5D_4)6s^2\ ^5D$	$5d^6(^3H_4)6s(^2H)6p\ ^1G$	224.99
Ir II		
Lower Level	Upper Level	λ(nm)
$5d^7(^4F_3)6s\ ^5F$	$5d^6(^3H_4)6s(^4H)6p\ ^5G$	145.93
$5d^7(^4F_3)6s\ ^5F$	$5d^7(^4F_3)6p\ ^5G$	189.69
$5d^7(^4F_3)6s\ ^5F$	$5d^6(^5D_4)6s(^4D)6p\ ^5F$	115.80
Pt III		
Lower Level	Upper Level	λ(nm)
$5d^8\ ^3F_2$	$5d^7(^2H_3)6p\ ^3G$	101.08
$5d^7(^4F_3)6s\ ^5F$	$5d^7(^2F_3)6p\ ^3F$	103.16
$5d^8\ ^3F_2$	$5d^7(^2G_3)6p\ ^3H$	105.14
Au IV		
Lower Level	Upper Level	λ(nm)
$5d^8\ ^3F_2$	$5d^7(^2H_3)6p\ ^3G$	68.59
$5d^8\ ^3F_2$	$5d^7(^4F_3)6p\ ^3G$	68.80
$5d^8\ ^3F_2$	$5d^7(^4F_3)6p\ ^3F$	67.41
Hg V		
Lower Level	Upper Level	λ(nm)
$5d^8\ ^3F_2$	$5d^7(^2H_3)6p\ ^3G$	50.36
$5d^7(^2F_3)6s\ ^3F$	$5d^6(^5D_4)6s(^4D)6p\ ^3D$	49.73
$5d^8\ ^3F_2$	$5d^7(^4F_3)6p\ ^5F$	52.71

In Figure 3.5, we plot the expansion opacity for each of the ions considered in this work. Although the GRASP^0 calculations show some improvement in the energies for certain levels, in most cases the comparison is mixed. As a consequence, we adopt the GRASP2K results for the expansion opacities. To facilitate comparison to prior studies (Kasen et al., 2013; Tanaka et al., 2020), the opacity is computed for $t = 1$ day and $\rho = 10^{-13}$ g/cm^3 with wavelength binning of $\Delta\lambda = 0.01\lambda$. We choose a temperature of 3700 K as it is representative of a kilonova. The opacity peaks in the visible shifting into the UV with increasing ion charge from $\sim$225 nm for Os I to $\sim$50 nm for Hg V similar to the behavior of the LTE

spectra in Figure 3.4. Further, as the ion charge increases, a number of IR lines appear with increasing strength over a less crowded background.

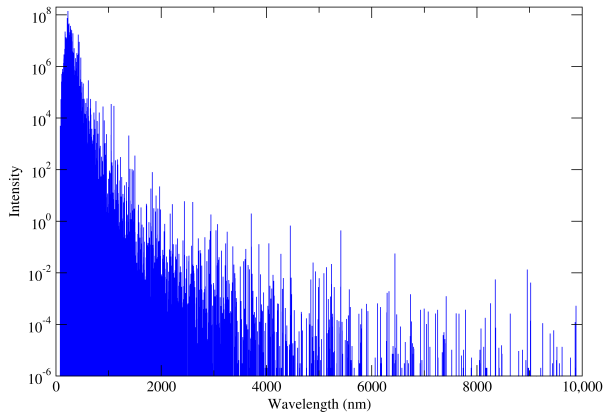

(**a**) Os I

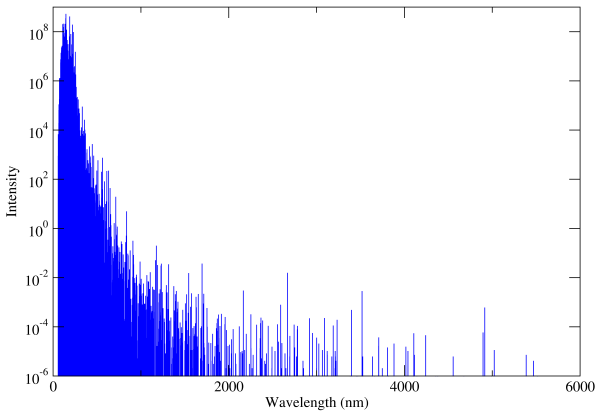

(**b**) Ir II

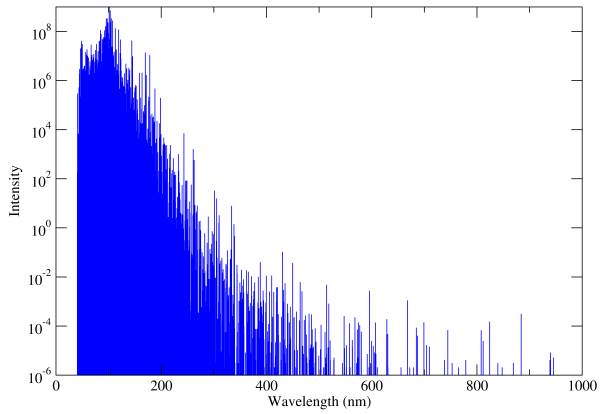

(**c**) Pt III

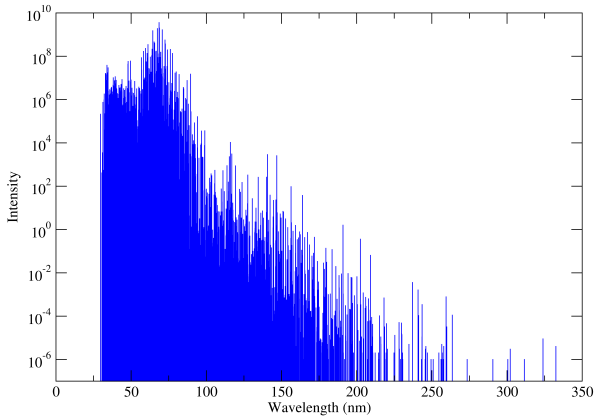

(**d**) Au IV

Figure 3.4: *Cont.*

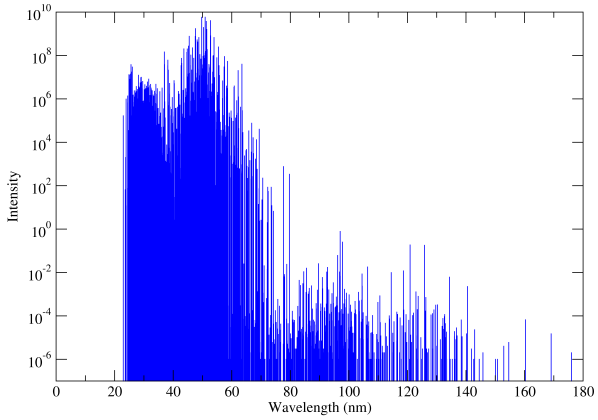

(**e**) Hg V

Figure 3.4: LTE spectra at T=5000 K for (a) Os I, (b) Ir II, (c) Pt III, (d) Au IV, and (e) Hg V obtained from GRASP2K calculations. The intensity is given in arbitrary units.

Figure 3.5f provides a comparison of the IR lines within the wavelength window of the *James Webb Space Telescope (JWST)* for 5–25 μm. The inclusion for non-dipole radiative rates in the calculation also allows for a line list that includes lines which could be observed by *JWST*. The background opacity magnitude in Figure 3.5f have been shifted to facilitate comparison of the lines for the various ions. A number of very prominent features emerge from the background and it is expected that in the mid-IR these features will be in emission. Table 3.9 lists the three most dominant transitions per ion which we predict may be observable by the Near Infrared Spectrograph (NIRSpec) or the Mid Infrared Instrument (MIRI) on *JWST* for a kilonova, particularly at late times. However, there is some uncertainty in the line positions as many transitions are between excited states for which there are very little experimental data; exceptions are for some lines due to Os I, Ir II, and Au IV as indicated in Table 3.9. The IR lines correspond primarily to M1 transitions within the ground configuration, and therefore the corresponding levels should be readily populated in the low temperature kilonova ejecta.

For Pt III, Gillanders et al., 2021 predict the $^3F_3 - ^3F_4$ line to occur at 1.092 μm, while the current work predicts the wavelength to be 1.234 μm. This aligns with a feature at 8.7 days in the observed spectrum of AT2017gfo. Further, a broad line centered near 1 μm may be explained by a cluster of Pt III lines at 0.947, 0.949, 0.991, and 1.077 μm (see Figure 5f and Figure 4 of Gillanders et al., 2021). However, MIRI/*JWST* observations near 7 μm and 8.7 μm may be the best hope of identifying platinum in a kilonova, as illustrated in the current Figure 3.5f.

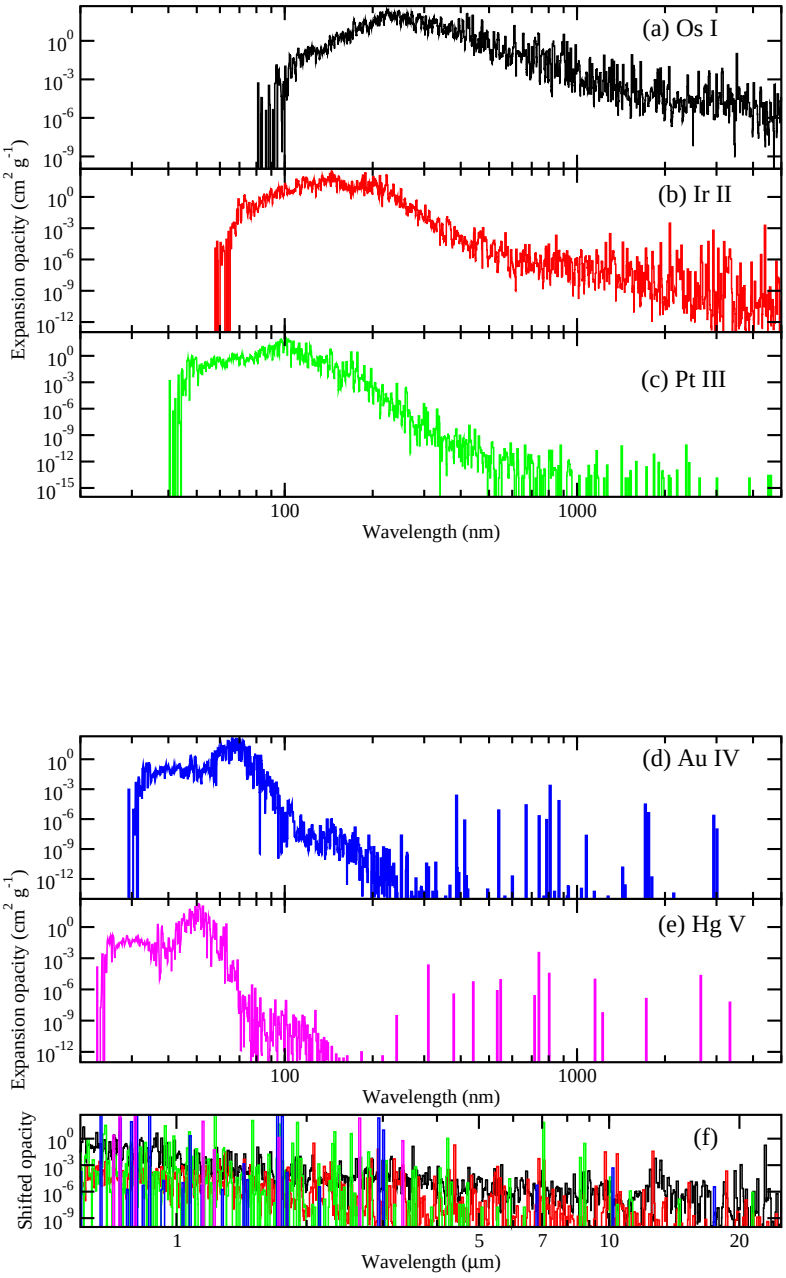

Figure 3.5: Expansion opacity at 1 day for 3700 K and 10^{-13} g/cm^3 for (a) Os I, (b) Ir II, (c) Pt III, (d) Au IV, and (e) Hg V using GRASP2K calculations. The opacities in the IR are displayed in f) for all ions but with their magnitudes shifted for comparison.

Table 3.9: Wavelengths of the three most intense IR features at 3700 K from the expansion opacity calculations using GRASP2K data. *Wavelength shifted to experimental value.

Os I		
Lower Level	Upper Level	$\lambda(\mu\mathrm{m})$
$5d^6 6s^2\ ^5D_4$	$5d^7 6s\ ^5F_5$	1.9440*
$5d^6 6s^2\ ^5D_2$	$5d^6 6s 6p\ ^7P_3$	3.540
$5d^7 6s\ ^5F_1$	$5d^6 6s 6p\ ^7D_1$	12.85
Ir II		
Lower Level	Upper Level	$\lambda(\mu\mathrm{m})$
$5d^7 6s\ ^5F_5$	$5d^7 6s\ ^5F_4$	2.0886*
$5d^7 6s\ ^5F_5$	$5d^8\ ^3F_4$	4.4201*
$5d^7 6s\ ^5F_3$	$5d^6 6s 6p\ ^5F_2$	12.689*
Pt III		
Lower Level	Upper Level	$\lambda(\mu\mathrm{m})$
$5d^8\ ^3F_4$	$5d^8\ ^3F_3$	1.234
$5d^7 6s\ ^5F_3$	$5d^7 6s\ ^5F_2$	4.257
$5d^8\ ^1D_2$	$5d^8\ ^3F_3$	7.09
Au IV		
Lower Level	Upper Level	$\lambda(\mu\mathrm{m})$
$5d^8\ ^3F_4$	$5d^8\ ^3F_3$	0.81344*
$5d^8\ ^3F_3$	$5d^8\ ^3P_2$	1.7218*
$5d^8\ ^3P_0$	$5d^8\ ^3P_1$	3.0261*
Hg V		
Lower Level	Upper Level	$\lambda(\mu\mathrm{m})$
$5d^8\ ^3F_4$	$5d^8\ ^3F_3$	0.744
$5d^8\ ^1D_2$	$5d^8\ ^3F_3$	2.665
$5d^8\ ^3P_0$	$5d^8\ ^3P_1$	3.353

3.3 Summary

In this work, we have performed atomic structure calculations for Os I (Z=76), Ir II (Z=77), Pt III (Z=78), Au IV (Z=79), and Hg V (Z=80) to construct atomic data for r-process elements. By using two different atomic code packages, GRASP2K and GRASP^0, energy levels, and transition probabilities (E1 and M1) for the above ions were computed.

A list of the strongest transitions are given for each ion in the UV for E1 transitions and in the IR for M1 transitions. It is pointed out that the possible identification of r-process elements will be easier in the

near- to mid-IR in the nebula phase of a kilonova and the M1 lines are far less crowded in this spectral window.

Chapter 4

Opacity Data for Kilonova Ejecta: Re Isoelectronic Sequence

The packages that are adopted to compute atomic energy levels, orbitals, and transition data within the relativistic formalism are GRASP^0 and GRASP2K. The detailed computational approach is same as Os isoelectronic sequence which has been explained in section 3.1.

4.1 Results and discussion

We have obtained results for the energy levels and transition probabilities for the Re isoelectronic sequence using both the GRASP^0 and GRASP2K packages. The NIST Atomic Spectral Database (Kramida et al., 2018) includes energy levels for Re I, Os II, and Pt IV, and A-Values for Pt IV only. Figure 4.1 displays energy level diagrams for Re I, Os II, Ir III, Pt IV, and Au V obtained from GRASP2K and GRASP^0 calculations using the target model in Table 4.1 as the reference configurations. Comparison is made to theoretical (Kato et al., 2021; Tanaka et al., 2020) and experimental data from the NIST database when available (Kramida et al., 2018). Moreover, in GRASP2K, 4 and 5 reference configurations were useed; for 4 configurations, the $5d^6 6s^2$ is omitted. Since the ground level is $5d^6 6s^2$ for Os I, the $5d^8$ is omitted in that case.

Table 4.1: GRASP2K and GRASP^0 target model

Ion/Atom	Ground Config.	GRASP2K
Re I	$[Xe]4f^{14}5d^5 6s^2$	$5d^6\{6s\}, 5d^5\{6s^2, 6s7s, 6s6p\}, 5d^4\{6s^2 6p\}$
Os II	$[Xe]4f^{14}5d^6 6s$	$5d^7, 5d^6\{6s, 6p\}, 5d^5\{6s^2, 6s6p\}$
Ir III	$[Xe]4f^{14}5d^7$	$5d^7, 5d^6\{6s, 6p\}, 5d^5\{6s^2, 6s6p\}$
Pt IV	$[Xe]4f^{14}5d^7$	$5d^7, 5d^6\{6s, 6p\}, 5d^5\{6s^2, 6s6p\}$
Au V	$[Xe]4f^{14}5d^7$	$5d^7, 5d^6\{6s, 6p\}, 5d^5\{6s^2, 6s6p\}$
	GRASP^0	
10-Config.	12-Config.	16-Config.
$5d^7$	$5d^7$	$5d^7$
$5d^6\{6s, 6p, 6d\}$	$5d^7\{6s, 6p, 6d\}$	$5d^6\{6s, 6p, 6d, 7s, 7p, 7d\}$
$5d^5\{6s^2, 6p^2, 6d^2, 6s6p, 6s6d, 6p6d\}$	$5d^5\{6s^2, 6p^2, 6d^2, 7s^2, 7p^2, 6s6p, 6s6d, 6p6d\}$	$5d^5\{6s^2, 6p^2, 6d^2, 7s^2, 7p^2, 7d^2, 6s6p, 6s6d, 6p6d\}$

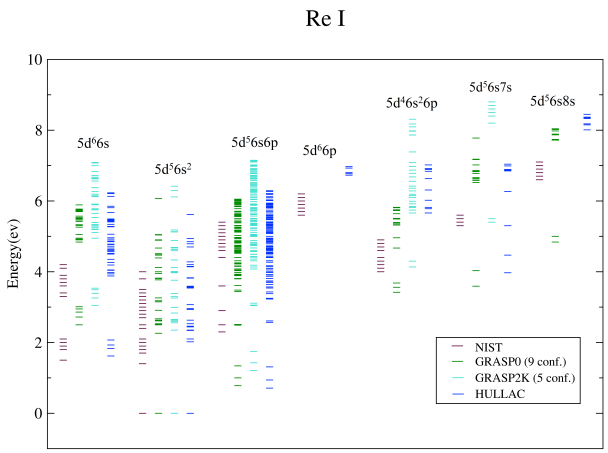

(**a**)

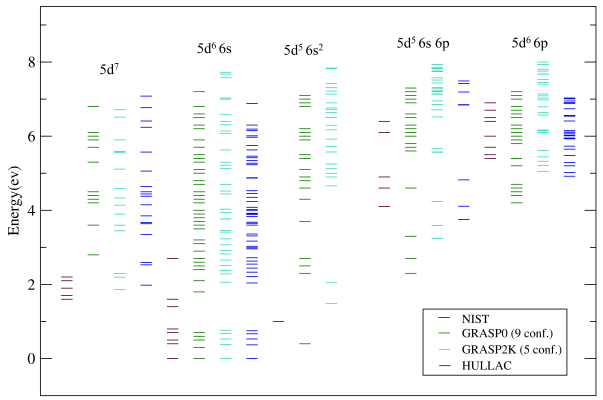

(**b**)

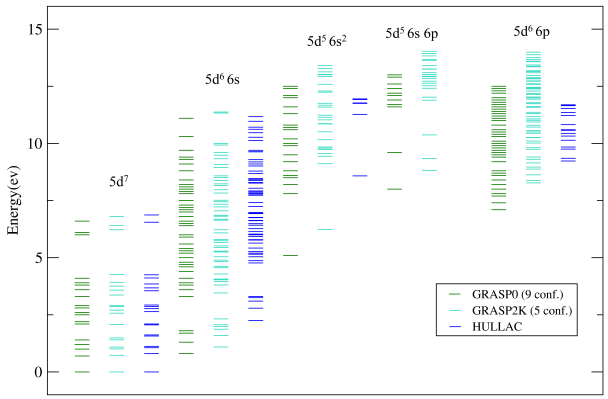

(**c**)

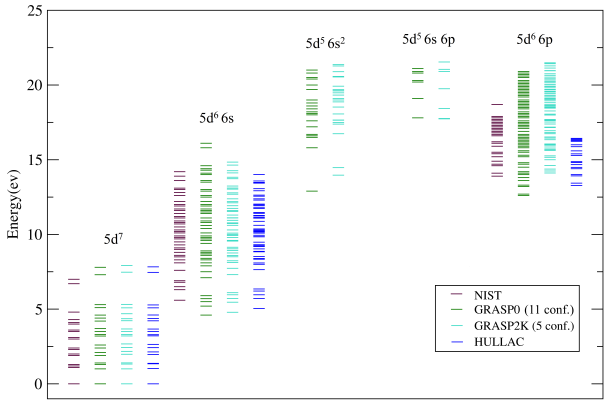

(**d**)

Figure 4.1: *Cont.*

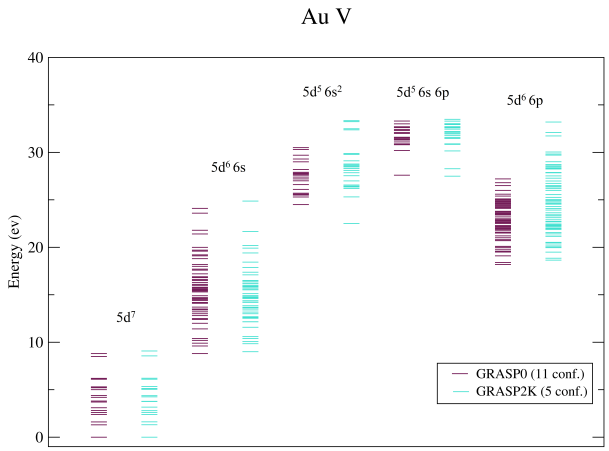

(e)

Figure 4.1: Energy level diagrams for a) Re I, b) Os II, c) Ir III, d) Pt IV, and e) Au V, comparing our results to available NIST (Kramida et al., 2018) and HULLAC calculations (Kato et al., 2021; Tanaka et al., 2020). Each stack of levels refers to excited states from the indicated configuration.

GRASP2K energy levels for Re I, Os II, and Pt IV are given in Tables 4.2, 4.3, and 4.4, respectively, where comparison is given with GRASP^0 calculations, the NIST database (Kramida et al., 2018), and from HULLAC calculations (Kato et al., 2021; Tanaka et al., 2020). Although levels in the ground term are in good agreement, there are deviations from the NIST database for both GRASP2K and GRASP^0 results for high lying levels. An average difference of 42% and 37.3% for Re I, 31% and 34% for Os II, and 15% and 17.1% for Pt IV or both GRASP^0 and GRASP2K respectively. Prior data for Ir III and Au V are unavailable, except for the ground term designation.

Table 4.2: Energy levels in cm^{-1} for Re I, calculations have been performed with configuration numbers given in parentheses.

Configuration	Term	J	NIST[a]	GRASP^0(9)	GRASP2K(5)	HULLAC[b]	ΔE^c	ΔE^d	ΔE^e	ΔE^f
$5d^5 6s^2$	^6S	5/2	0.00	0.00	0.00	0.00	0.00	0.00	0.00	0.00
$5d^5 6s^2$	^4P	5/2	11583.96	18269.24	17771.97	16936.50	-6685.28	-6188.01	1332.74	835.47
		3/2	13826.12	20154.23	25797.91	16291.30	-6328.11	-11971.79	3862.93	9506.61
		1/2	15165.89	21519.56	21947.91	20404.45	-6353.67	-6782.02	1115.11	1543.46
$5d^6(^5D)6s$	^6D	9/2	11754.52	20219.08	17298.56	13065.30	-8464.56	-5544.04	7153.78	4233.26
		7/2	14216.86	21948.75	19010.99	14758.95	-7731.89	-4794.13	7189.8	4252.04
		5/2	15770.42	23074.45	20358.63	15565.45	-7304.03	-4588.21	7509.00	4793.18

Continued on next page

Table 4.2: Energy levels in cm^{-1} for Re I, calculations have been performed with configuration numbers given in parentheses.

Configuration	Term	J	NIST[a]	GRASP^0(9)	GRASP2K(5)	HULLAC[b]	ΔE^c	ΔE^d	ΔE^e	ΔE^f
		3/2	16327.51	23796.57	21092.40	–	-7469.06	-4764.89	–	–
		1/2	17238.30	24246.34	20638.68	16694.55	-7008.04	-3400.38	7551.79	3944.13
$5d^5 6s^2$	^4G	5/2	14621.46	20267.87	19490.83	18872.10	-5646.41	-4869.37	1395.77	618.73
		7/2	15058.19	20384.98	19669.49	18952.75	-5326.79	-4611.3	1432.23	716.74
		11/2	16307.15	21053.76	20291.54	19678.60	-4746.61	-3984.39	1375.16	612.94
		9/2	16619.28	21222.65	20464.78	19839.90	-4603.37	-3845.5	1382.75	624.88
$5d^5 6s^2$	^4D	7/2	17330.82	23508.89	22457.27	21210.95	-6178.07	-5126.45	2297.94	1246.32
		5/2	19457.89	25688.21	25075.44	23872.40	-6230.32	-5617.55	1815.81	1203.04
		1/2	19757.91	25413.55	24742.65	23630.45	-5655.64	-4984.74	1783.1	1112.2
		3/2	20481.73	26296.81	19568.52	18872.10	-5815.08	913.21	7424.71	696.42
$5d^5 6s(^7S)6p$	$^8P^o$	5/2	18950.1	6329.59	5607.16	5726.15	12620.51	13342.94	603.44	-118.99
		7/2	20447.8	8081.83	7356.86	7581.10	12365.97	13090.94	500.73	-224.24
		9/2	23631.82	10800.98	9892.98	10563.84	12830.84	13738.84	237.14	-670.86
$5d^5 6s^2$	^2F	7/2	21775.40	30766.58	30231.48	28550.10	-8991.18	-8456.08	2216.48	1681.38
		5/2	24425.40	30707.74	39289.26	28711.40	-6282.34	-14863.86	1996.34	10577.86
$5d^5 6s^2$	^2G	9/2	22160.04	31883.29	30965.64	28550.10	-9723.25	-8805.6	3333.19	2415.54
		7/2	24724.22	36046.17	34693.01	–	-11321.95	-9968.79	–	–
$5d^5 6s^2$	^2D	3/2	22422.83	30841.12	30442.61	28792.05	-8418.29	-8019.78	2049.07	1650.56
		5/2	23154.81	33260.25	30281.30	30808.30	-10105.44	-7126.49	2451.95	-527.00
$5d^5 6s^2$	^2I	11/2	23956.00	30434.23	29550.37	28953.35	-6478.23	-5594.37	1480.88	597.02
		13/2	26348.96	32247.71	31261.83	30888.95	-5898.75	-4912.87	1358.76	372.88
$5d^5 6s^2$	^4F	3/2	26131.57	35412.73	35034.62	–	-9281.16	-8903.05	–	–
		9/2	27514.31	36370.47	40549.60	–	-8856.16	-13035.29	–	–
		5/2	28030.32	37658.61	32810.54	33469.75	-9628.29	-4780.22	4188.86	-659.21
		7/2	28542.13	36301.68	35459.37	33873.00	-7759.55	-6917.24	2428.68	1586.37
$5d^6(^3P)6s$	^4P	1/2	–	50366.02	44909.28	32582.60	–	–	17783.42	12326.68
		5/2	26661.43	40754.15	38080.52	34356.90	-14092.72	-11419.09	6397.25	3723.62
		3/2	30526.60	42400.15	42093.73	36292.50	-11873.55	-11567.13	6107.65	5801.23

Continued on next page

Table 4.2: Energy levels in cm^{-1} for Re I, calculations have been performed with configuration numbers given in parentheses.

Configuration	Term	J	NIST[a]	GRASP^0(9)	GRASP2K(5)	HULLAC[b]	ΔE^c	ΔE^d	ΔE^e	ΔE^f
$5d^6(^3H)6s$	^4H	13/2	27130.14	39500.15	36183.17	31776.10	-12370.01	-9053.03	7724.05	4407.07
		9/2	27161.35	39912.47	36929.89	32663.25	-12751.12	-9768.54	7249.22	4266.64
		11/2	27243.88	39707.31	36569.24	32098.70	-12463.43	-9325.36	7608.61	4470.54
		7/2	28809.87	40762.78	38011.09	31292.20	-11952.91	-9201.22	9470.58	6718.89
$5d^6(^5D)6s$	^4D	7/2	27141.13	39031.94	40673.69	35082.75	-11890.81	-13532.56	3949.19	5590.94
		3/2	27827.65	43758.02	40001.63	36292.50	-15930.37	-12173.98	7465.52	3709.13
		5/2	29800.38	42977.13	40567.95	37099.00	-13176.75	-10767.57	5878.13	3468.95
		1/2	30131.57	44251.85	40931.93	37340.95	-14120.28	-10800.36	6910.9	3590.98

[a] Atomic energy levels from the NIST database (Kramida et al., 2018).

[b] Atomic energy levels from Tanaka et al., 2020.

[c] Energy difference between NIST and GRASP^0.

[d] Energy difference between NIST and GRASP2K.

[e] Energy difference between GRASP^0 and HULLAC.

[f] Energy difference between GRASP2K and HULLAC.

Table 4.3: Energy levels in cm^{-1} for Os II. The calculations have been performed with configuration numbers given in parentheses.

Configuration	Term	J	DESIRE[a]	GRASP^0(9)	GRASP2K(5)	HULLAC[b]	ΔE^c	ΔE^d	ΔE^e	ΔE^f
$5d^6(^5D)6s$	^6D	9/2	0.00	0.00	0.00	0.00	0.00	0.00	0.00	0.00
		7/2	3593.15	2828.98	3053.08	2984.05	764.17	540.07	-155.07	69.03
		5/2	3928.94	4322.79	4260.41	4274.45	-393.85	-331.47	48.34	-14.04
		3/2	5592.05	5205.50	5450.56	5403.55	386.55	141.49	-198.05	47.01
		1/2	6636.57	5859.09	6159.83	6048.75	777.48	476.74	-189.66	111.08
$5d^5 6s^2$	^6S	5/2	7891.93	3196.42	12024.39	–	4695.51	-4132.46	–	–
$5d^6(^5D)6s$	^4D	7/2	11459.90	16614.46	19155.69	17823.65	-5154.56	-7695.79	-1209.19	1332.04
		5/2	11654.08	14841.59	22770.20	16452.60	-3187.51	-11116.12	-1611.01	6317.60
		3/2	13136.61	20419.18	22366.21	18791.45	-7282.57	-9229.60	1627.73	3574.76
$5d^7$	^4F	7/2	13203.88	22818.49	16614.46	20404.45	-9614.61	-3410.58	2414.04	-3789.99
		5/2	13414.80	–	18499.38	29598.55	–	-5084.58	–	-11099.17

Continued on next page

Table 4.3: Energy levels in cm^{-1} for Os II. The calculations have been performed with configuration numbers given in parentheses.

Configuration	Term	J	DESIRE[a]	GRASP^0(9)	GRASP2K(5)	HULLAC[b]	ΔE^c	ΔE^d	ΔE^e	ΔE^f
$5d^7$	^2G	9/2	15605.58	28809.59	29025.99	29356.60	-13204.01	-13420.41	-547.01	-330.61
		7/2	17242.26	35588.31	33366.50	27017.75	-18346.05	-16124.24	8570.56	6348.75
$5d^7$	^2P	3/2	17424.39	36590.74	33216.84	31050.25	-19166.35	-15792.45	5540.49	2166.59
$5d^7$	^4P	5/2	17569.40	35878.67	34951.96	35808.60	-18309.27	-17382.56	70.07	-856.64
$5d^7$	^2H	11/2	17688.64	34386.69	41218.17	40808.90	-16698.05	-23529.53	-6422.21	409.27
$5d^6(^3G)6s$	^4G	9/2	21590.81	31946.31	27519.06	20565.75	-10355.50	-5928.25	11380.56	6953.31
$5d^5 6s(^7S)6P$	^8P	5/2	37321.53	45400.57	26141.45	30243.75	-8079.04	11180.08	15156.82	-4102.30
		7/2	39389.49	46401.82	28972.58	33147.15	-7012.33	10416.91	13254.67	-4174.57
		9/2	41282.95	47871.16	34188.78	38873.30	-6588.21	7094.17	89997.86	-4684.52
$5d^6(^5D)6p$	^6D	7/2	43802.36	43309.56	40478.02	39679.80	492.80	3324.34	3629.76	798.22
		9/2	44315.40	43453.04	42006.04	40486.30	862.36	2309.36	2966.74	1519.74
		3/2	46157.19	42378.26	43887.56	42663.85	3778.93	2269.63	-285.59	1223.71
		5/2	46373.51	42315.24	42938.46	41938.00	4058.27	3435.05	377.24	1000.46
		1/2	48128.08	42274.61	45245.97	44196.20	5853.47	2882.11	-1921.59	1049.77
$5d^6(^5D)6p$	^6F	5/2	48798.70	49660.97	48952.31	46212.45	-862.27	-153.61	3448.52	2739.86
		9/2	51951.61	51461.90	49598.46	48470.65	489.71	2353.15	2991.25	1127.81
		7/2	52206.48	53333.92	49735.01	45567.25	-1127.44	2471.47	7766.67	4167.76
$5d^5 6s(^7S)6P$	^6P	7/2	49149.39	50843.19	44889.86	–	-1693.80	4259.53	–	–
		5/2	51770.38	51257.76	44946.08	55245.25	512.62	6824.30	-3987.49	-10299.17
$5d^6(^5D)6p$	^4F	7/2	54379.27	55243.31	56183.45	57180.85	-864.04	-1804.18	-1937.54	-997.4
		5/2	55538.65	54922.88	57172.45	56696.95	615.77	-1633.80	-1774.07	475.50
$5d^6(^5D)6p$	^4D	5/2	54445.19	56126.72	–	–	-1681.53	–	–	–

[a] Atomic energy levels, NIST database (Kramida et al., 2018), Relativistic Hartree-Fock plus core polarization (HFR + CP).

[b] Atomic energy levels from Tanaka et al., 2020.

[c] Energy difference between NIST and GRASP^0.

[d] Energy difference between NIST and GRASP2K.

[e] Energy difference between GRASP^0 and HULLAC.

[f] Energy difference between GRASP2K and HULLAC.

Table 4.4: Energy levels in cm^{-1} for Pt IV. The calculations have been performed with configuration numbers given in parentheses.

Configuration	Term	J	NIST[a]	GRASP^0(11)	GRASP2K(5)	HULLAC[b]	ΔE[c]	ΔE[d]	ΔE[e]	ΔE[f]
$5d^7$	^4F	9/2	0.00	0.00	0.00	0.00	0.00	0.00	0.00	0.00
		7/2	9567.18	8290.55	8104.91	8306.95	1276.63	1462.27	-16.40	-202.04
		5/2	10452.87	10663.48	10674.90	10807.10	-210.61	-222.03	-143.52	-132.20
		3/2	15539.29	11090.53	11306.76	11049.05	4448.76	4232.53	41.48	257.71
$5d^7$	^2P	3/2	9214.92	15745.87	28311.15	15807.40	-6530.95	-19096.23	-61.53	12503.75
		1/2	32952.87	21134.36	34099.91	21291.60	11818.51	-1147.04	-157.24	12808.31
$5d^7$	^4P	5/2	16169.35	17022.35	17528.38	17259.10	-853.00	-1359.03	-236.75	269.28
		1/2	19624.95	34096.80	21540.07	34034.30	-14471.85	-1915.12	62.50	-12494.23
		3/2	27870.20	28166.74	15984.89	28308.15	-296.54	11885.31	-141.41	-12323.26
$5d^7$	^2G	9/2	18361.43	19593.64	19605.35	19436.65	-1232.21	-1243.92	156.99	168.70
		7/2	24800.74	25903.01	25878.39	25888.65	-1102.27	-1077.65	14.36	-10.26
$5d^7$	^2H	11/2	24437.46	26586.03	26676.97	26533.85	-2148.57	-2239.51	52.18	143.12
		9/2	34556.09	35281.47	35153.10	35324.70	-725.38	-597.01	-43.23	-171.60
$5d^7$	^2F	5/2	32168.62	37079.34	37871.54	37179.65	-4910.72	-5702.92	-100.31	691.89
		7/2	39002.13	42500.16	42864.65	42583.20	-3498.03	-3862.52	-83.04	281.45
$5d^6(^5D)6s$	^6D	9/2	45091.69	36873.26	38639.36	40647.60	8218.43	6398.33	-3774.34	-2008.24
		7/2	50953.00	42063.82	44039.94	46051.15	8889.18	6913.06	-3987.33	-2011.21
		5/2	52223.37	44219.66	46008.04	48067.40	8003.71	6215.33	-3847.74	-2059.36
		3/2	54811.51	46276.93	48074.53	50083.65	8534.58	6736.98	-3806.72	-2009.12
		1/2	56071.44	47386.32	49220.03	51212.75	8685.12	6851.41	-1833.71	-1992.72
$5d^6(^5D)6s$	^4D	7/2	60955.41	57624.72	58948.93	61616.60	3330.69	2006.48	-3991.88	-2667.67
		5/2	65176.69	60782.63	62188.73	65245.85	4394.06	2987.96	-4463.22	-3057.12
		3/2	67233.76	65179.61	66422.19	68794.45	2054.15	811.57	-2372.26	-2372.26
		1/2	70622.67	67239.55	68585.98	71294.60	3383.12	2036.69	-4055.05	-2708.62
$5d^6(^3H)6s$	^4H	7/2	68196.37	63840.96	65275.50	67665.35	4355.41	2920.87	-3824.39	-2389.85

Continued on next page

Table 4.4: Energy levels in cm^{-1} for Pt IV. The calculations have been performed with configuration numbers given in parentheses.

Configuration	Term	J	NIST[a]	GRASP^0(11)	GRASP2K(5)	HULLAC[b]	ΔE[c]	ΔE[d]	ΔE[e]	ΔE[f]
		11/2	68462.66	63660.31	65137.17	67262.10	4802.35	3325.49	-3601.79	-2124.93
		13/2	69223.49	64107.87	65516.53	67584.70	5115.62	3706.96	-3476.83	-2068.17
		9/2	73763.04	69193.87	70627.32	72826.95	4569.17	3135.72	-3633.08	-2199.63

[a] Atomic energy levels from the NIST database (Kramida et al., 2018).

[b] Atomic energy levels from Tanaka et al., 2020 (Kato et al., 2021).

[c] Energy difference between NIST and GRASP^0.

[d] Energy difference between NIST and GRASP2K.

[e] Energy difference between GRASP^0 and HULLAC.

[f] Energy difference between GRASP2K and HULLAC.

Electric dipole (E1) transition probabilities as a function of wavelength are plotted in Figure 4.2 for Re I, Os II, Ir III, Pt IV, and Au V. As one sees from the figures, most transitions occur at short wavelength. The weighted transition probabilities, gA-values where $g = 2J + 1$, for Os II are compared with the DESIRE database (Fivet et al., 2007) and HULLAC calculation (Kato et al., 2021; Tanaka et al., 2020) in Table 4.5 (D.E.S.I.R.E. (DatabasE on SIxth Row Elements) is an atomic physics database where information concerning the wavelengths, the oscillator strengths, the transition probabilities and the radiative lifetimes are provided. The available data in this database are a combination of measurements and calculations.). There is reasonable agreement between calculations using GRASP2K and DESIRE, and GRASP2K and HULLAC. It is noticeable that for highly ionized ions, like Au V, most transitions occur at shorter wavelength compared to low ionized ions, like Ir II. In addition, the convergence of the E1 transition probability with different calculation methods for one transition is shown in Figure 4.3; for all ions the transition is between the $5d^8\ ^3F$ and the $5d^7(^2H_3)6p\ ^3G$. This transition is chosen as an illustration since it typical has the largest transition probability as shown in Table 4.6. Neither NIST nor DESIRE provide this transition.

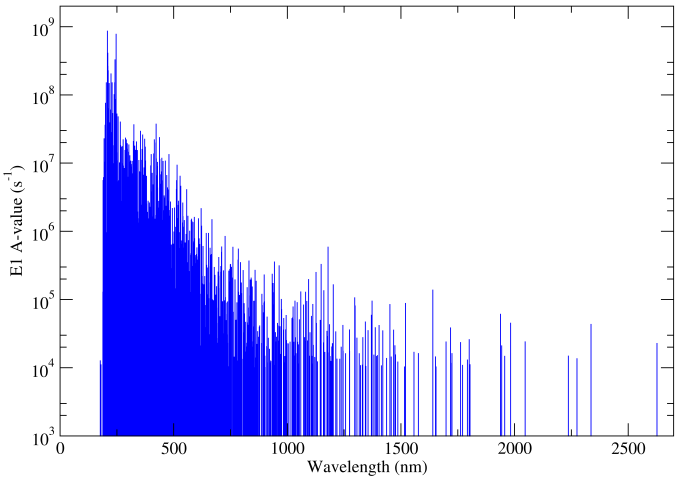

(**a**) Re I

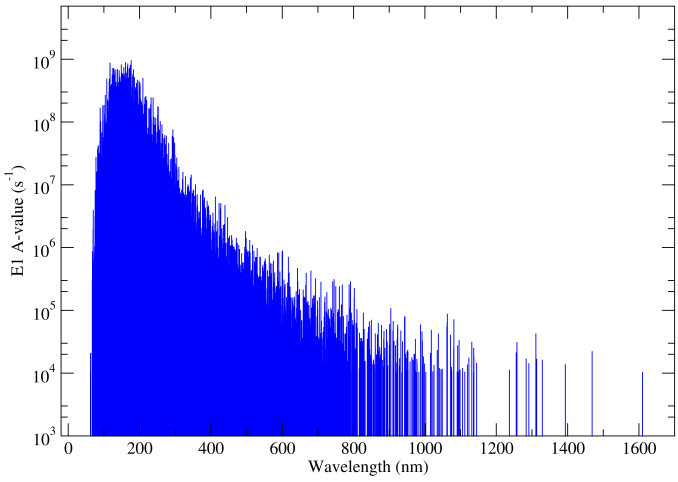

(**b**) Os II

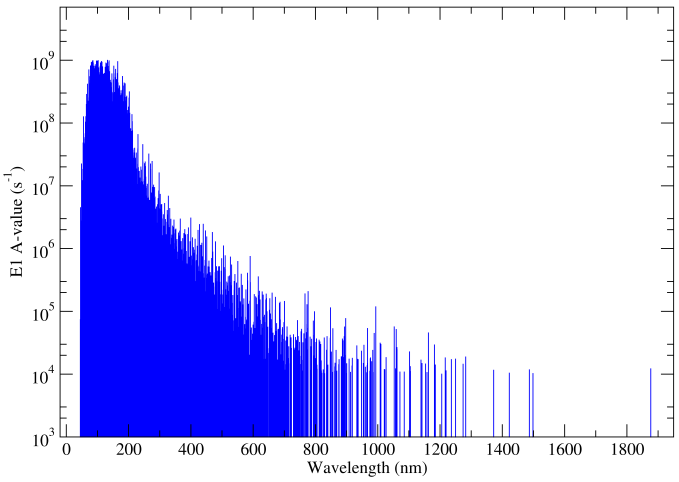

(**c**) Ir III

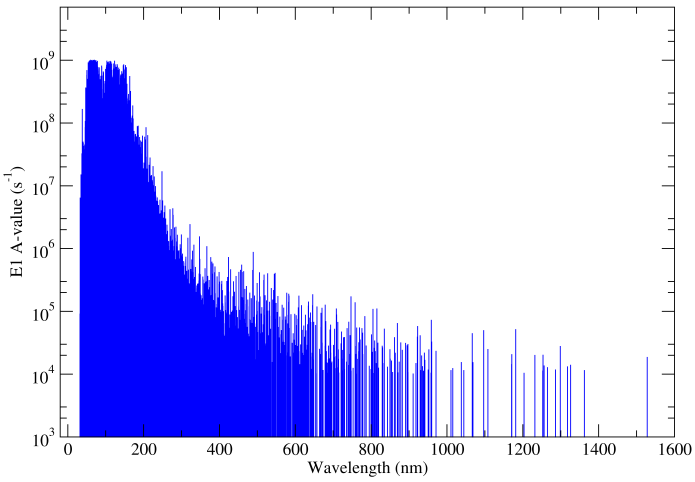

(**d**) Pt IV

Figure 4.2: *Cont.*

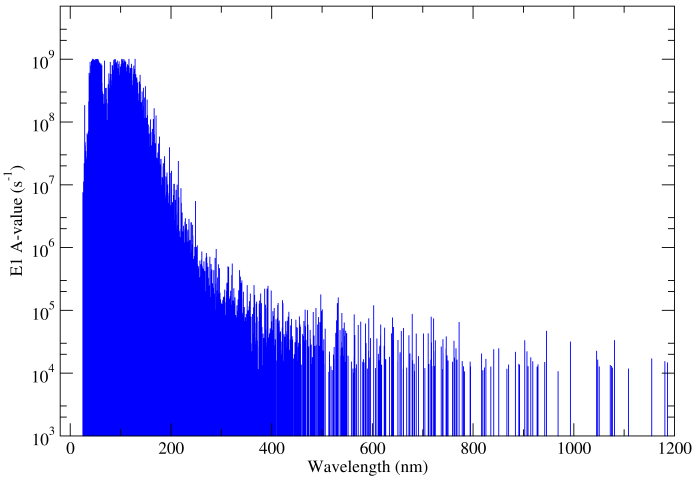

(e) Au V

Figure 4.2: Transition probabilities for E1 transitions for a) Re I, b) Os II, c) Ir III, d) Pt IV, and e) Au V obtained with Grasp2K (5 configurations) calculations.

Table 4.5: Weighed transition probabilities (gA-values) for Os II

Lower Level	J	Upper Level	J	gA(s^{-1}) DESIRE[a]	GRASP2K	HULLAC[b]	$\%D_i$	$\%D_j$
$5d^6(^5D)6s\,^6D_{9/2}$	9/2	$5d^6(^5D)6p\,^4F_{7/2}$	7/2	2.00E+06	9.91E+08	8.77E+08	199.19	12.21
$5d^6(^5D)6s\,^6D_{9/2}$	9/2	$5d^6(^5D)6p\,^6F_{7/2}$	7/2	1.60E+06	1.52E+08	5.31E+07	195.83	96.49
$5d^6(^5D)6s\,^6D_{9/2}$	9/2	$5d^6(^5D)6p\,^6F_{9/2}$	9/2	5.96E+08	1.96E+08	2.56E+08	101.01	26.55
$5d^6(^5D)6s\,^6D_{7/2}$	7/2	$5d^6(^5D)6p\,^4D_{5/2}$	5/2	8.14E+07	–	–	–	–
$5d^6(^5D)6s\,^6D_{7/2}$	7/2	$5d^6(^5D)6p\,^4F_{7/2}$	7/2	4.60E+07	9.38E+08	2.92E+08	101.01	181.30
$5d^6(^5D)6s\,^6D_{5/2}$	5/2	$5d^6(^5D)6p\,^4D_{5/2}$	5/2	1.73E+08	–	–	–	–
$5d^6(^5D)6s\,^6D_{5/2}$	5/2	$5d^6(^5D)6p\,^4F_{7/2}$	7/2	6.58E+08	9.11E+07	4.60E+07	151.37	65.84
$5d^6(^5D)6s\,^6D_{9/2}$	9/2	$5d^56s(^7S)6p\,^6P_{7/2}$	7/2	1.67E+07	1.09E+08	–	146.97	–
$5d^6(^5D)6s\,^6D_{3/2}$	3/2	$5d^6(^5D)6p\,^4D_{5/2}$	5/2	2.90E+06	–	–	–	–
$5d^6(^5D)6s\,^6D_{7/2}$	7/2	$5d^6(^5D)6p\,^6F_{9/2}$	9/2	1.76E+09	2.43E+09	2.24E+09	32.06	8.15
$5d^6(^5D)6s\,^6D_{5/2}$	5/2	$5d^6(^5D)6p\,^6F_{7/2}$	7/2	1.03E+09	1.75E+09	8.80E+07	51.80	180.85
$5d^6(^5D)6s\,^6D_{7/2}$	7/2	$5d^56s(^7S)6p\,^6P_{5/2}$	5/2	1.00E+06	1.46E+08	4.92E+07	197.28	99.18
$5d^6(^5D)6s\,^6D_{5/2}$	5/2	$5d^56s(^7S)6p\,^6P_{5/2}$	5/2	3.55E+07	1.21E+08	2.27E+08	54.60	60.92
$5d^56s^2\,^6S_{5/2}$	5/2	$5d^6(^5D)6p\,^4D_{5/2}$	5/2	1.09E+08	–	–	–	–

Continued on next page

Table 4.5: Weighed transition probabilities (gA-values) for Os II

				gA(s^{-1})				
Lower Level	J	Upper Level	J	DESIRE[a]	GRASP2K	HULLAC[b]	$\%D_i$	$\%D_j$
$5d^5 6s^2\ ^6S_{5/2}$	5/2	$5d^6(^5D)6p\ ^4F_{7/2}$	7/2	1.90E+08	2.18E+07	–	158.83	–
$5d^6(^5D)6s\ ^6D_{3/2}$	3/2	$5d^5 6s(^7S)6p\ ^6P_{5/2}$	5/2	4.14E+08	4.24E+06	1.72E+08	195.94	190.38
$5d^6(^5D)6s\ ^6D_{7/2}$	7/2	$5d^5 6s(^7S)6p\ ^6P_{7/2}$	7/2	8.31E+08	7.44E+08	–	11.05	–
$5d^6(^5D)6s\ ^6D_{5/2}$	5/2	$5d^5 6s(^7S)6p\ ^6P_{7/2}$	7/2	1.31E+07	1.63E+05	–	195.10	–
$5d^6(^5D)6s\ ^6D_{5/2}$	5/2	$5d^6(^5D)6p\ ^6F_{5/2}$	5/2	4.33E+08	4.78E+08	6.13E+08	9.89	24.77
$5d^6(^5D)6s\ ^6D_{9/2}$	9/2	$5d^6(^5D)6p\ ^6D_{9/2}$	9/2	1.73E+09	2.41E+09	2.29E+09	32.85	5.11
$5d^5 6s^2\ ^6S_{5/2}$	5/2	$5d^6(^5D)6p\ ^6F_{7/2}$	7/2	3.30E+06	2.25E+06	–	37.91	–
$5d^5 6s^2\ ^6S_{5/2}$	5/2	$5d^5 6s(^7S)6p\ ^6P_{5/2}$	5/2	1.09E+08	1.17E+08	–	7.08	–
$5d^6(^5D)6s\ ^6D_{9/2}$	9/2	$5d^6(^5D)6p\ ^6D_{7/2}$	7/2	1.15E+09	9.18E+08	1.13E+09	22.44	20.70
$5d^6(^5D)6s\ ^6D_{3/2}$	3/2	$5d^6(^5D)6p\ ^6F_{5/2}$	5/2	2.49E+08	8.52E+08	2.46E+08	109.64	110.38
$5d^6(^5D)6s\ ^4D_{7/2}$	7/2	$5d^6(^5D)6p\ ^4D_{5/2}$	5/2	5.43E+08	–	–	–	–
$5d^6(^5D)6s\ ^4D_{7/2}$	7/2	$5d^6(^5D)6p\ ^4F_{7/2}$	7/2	1.52E+08	2.04E+04	1.08E+07	199.95	199.25
$5d^6(^5D)6s\ ^4D_{5/2}$	5/2	$5d^6(^5D)6p\ ^4D_{5/2}$	5/2	1.86E+07	–	–	–	–
$5d^6(^5D)6s\ ^6D_{7/2}$	7/2	$5d^6(^5D)6p\ ^6D_{5/2}$	5/2	7.72E+08	7.58E+08	9.44E+08	1.83	21.86
$5d^6(^5D)6s\ ^4D_{5/2}$	5/2	$5d^6(^5D)6p\ ^4F_{7/2}$	7/2	2.20E+07	2.37E+08	2.74E+06	166.02	195.43
$5d^6(^5D)6s\ ^6D_{3/2}$	3/2	$5d^6(^5D)6p\ ^6D_{1/2}$	1/2	2.60E+08	3.51E+08	3.57E+08	29.79	1.69
$5d^6(^5D)6s\ ^6D_{5/2}$	5/2	$5d^6(^5D)6p\ ^6D_{5/2}$	5/2	8.00E+07	1.37E+08	1.58E+08	52.53	14.24
$5d^6(^5D)6s\ ^6D_{5/2}$	5/2	$5d^6(^5D)6p\ ^6D_{3/2}$	3/2	6.28E+08	6.82E+08	6.64E+08	8.24	2.67
$5d^6(^5D)6s\ ^4D_{3/2}$	3/2	$5d^6(^5D)6p\ ^4D_{5/2}$	5/2	6.71E+07	–	–	–	–
$5d^6(^5D)6s\ ^6D_{9/2}$	9/2	$5d^5 6s(^7S)6p\ ^8P_{9/2}$	9/2	7.01E+07	2.83E+06	4.02E+05	184.48	150.25
$5d^5 6s^2\ ^6S_{5/2}$	5/2	$5d^5 6s(^7S)6p\ ^6P_{7/2}$	7/2	7.01E+07	2.13E+08	–	100.95	–
$5d^7\ ^4F_{5/2}$	5/2	$5d^6(^5D)6p\ ^4F_{7/2}$	7/2	3.80E+07	5.37E+07	1.29E+03	34.24	199.99
$5d^5 6s^2\ ^6S_{5/2}$	5/2	$5d^6(^5D)6p\ ^6F_{5/2}$	5/2	3.22E+07	4.13E+07	–	24.76	–
$5d^6(^5D)6s\ ^6D_{3/2}$	3/2	$5d^6(^5D)6p\ ^6D_{5/2}$	5/2	5.70E+07	6.14E+07	5.90E+07	7.43	3.99
$5d^6(^5D)6s\ ^4D_{7/2}$	7/2	$5d^6(^5D)6p\ ^6F_{7/2}$	7/2	9.80E+07	2.06E+07	7.25E+05	130.52	186.40
$5d^6(^5D)6s\ ^6D_{7/2}$	7/2	$5d^6(^5D)6p\ ^6D_{9/2}$	9/2	2.16E+07	7.43E+05	3.03E+06	186.70	121.23
$5d^6(^5D)6s\ ^6D_{3/2}$	3/2	$5d^6(^5D)6p\ ^6D_{3/2}$	3/2	1.00E+07	1.70E+07	1.94E+07	51.85	13.19
$5d^6(^5D)6s\ ^4D_{5/2}$	5/2	$5d^6(^5D)6p\ ^6F_{7/2}$	7/2	3.59E+07	5.51E+07	9.95E+06	42.20	138.82
$5d^6(^5D)6s\ ^4D_{7/2}$	7/2	$5d^6(^5D)6p\ ^6F_{9/2}$	9/2	2.78E+08	1.88E+08	1.84E+08	38.63	2.15
$5d^6(^5D)6s\ ^4D_{7/2}$	7/2	$5d^5 6s(^7S)6p\ ^6P_{5/2}$	5/2	2.07E+07	2.72E+06	7.38E+06	153.54	92.28
$5d^6(^5D)6s\ ^6D_{7/2}$	7/2	$5d^6(^5D)6p\ ^6D_{7/2}$	7/2	2.26E+08	2.66E+08	3.40E+08	16.26	24.42
$5d^6(^5D)6s\ ^4D_{5/2}$	5/2	$5d^5 6s(^7S)6p\ ^6P_{5/2}$	5/2	4.53E+07	6.56E+05	3.83E+08	194.29	199.23
$5d^6(^5D)6s\ ^6D_{5/2}$	5/2	$5d^6(^5D)6p\ ^6D_{7/2}$	7/2	2.41E+07	2.48E+07	3.39E+07	2.86	31.00
$5d^6(^5D)6s\ ^6D_{1/2}$	1/2	$5d^6(^5D)6p\ ^6D_{3/2}$	3/2	2.07E+07	4.40E+07	4.75E+07	72.02	7.65
$5d^6(^5D)6s\ ^6D_{9/2}$	9/2	$5d^5 6s(^7S)6p\ ^8P_{7/2}$	7/2	3.72E+07	1.49E+06	1.82E+07	184.60	169.73

Continued on next page

Table 4.5: Weighed transition probabilities (gA-values) for Os II

Lower Level	J	Upper Level	J	gA(s^{-1}) DESIRE[a]	GRASP2K	HULLAC[b]	$\%D_i$	$\%D_j$
$5d^7\ ^4F_{5/2}$	5/2	$5d^6(^5D)6p\ ^6F_{7/2}$	7/2	6.04E+07	2.95E+06	9.44E+04	181.37	187.60

[a] gA-values, DESIRE database (Xu et al., 2007).

[b] gA-values from Tanaka et al., 2020 using HULLAC.

$\%D_i$ percent difference of GRASP2K and DESIRE.

$\%D_J$ percent difference of GRASP2K and HULLAC.

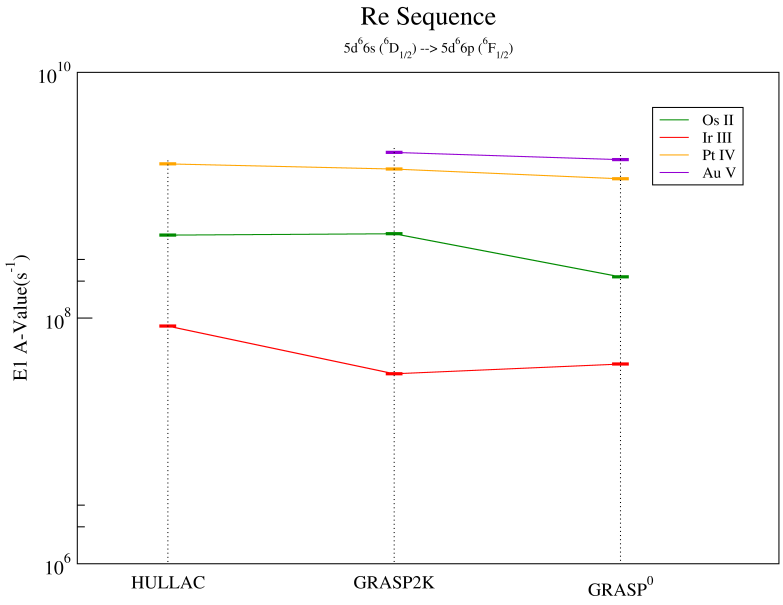

Figure 4.3: Convergence of E1 transition probability for different methods for the $5d^6 6s\ ^6D_{\frac{1}{2}} \rightarrow 5d^6 6p\ ^6F_{\frac{1}{2}}$ transition.

LTE spectra are shown in Figure 4.4 for Re I, Os II, Ir III, Pt IV, and Au V considering only E1 transitions. The spectra were computed assuming a Boltzmann distribution of electronic states at 5000 K, which is the expected temperature of a kilonova at early times. The line intensities are strongest at short wavelengths as expected. Table 4.6 lists the three most intense lines from the LTE spectrum at 5000 K for each ion. Also, to compare our results with the Tanaka et al., 2020, in Table 4.7 the gA-values of the most intense lines are listed.

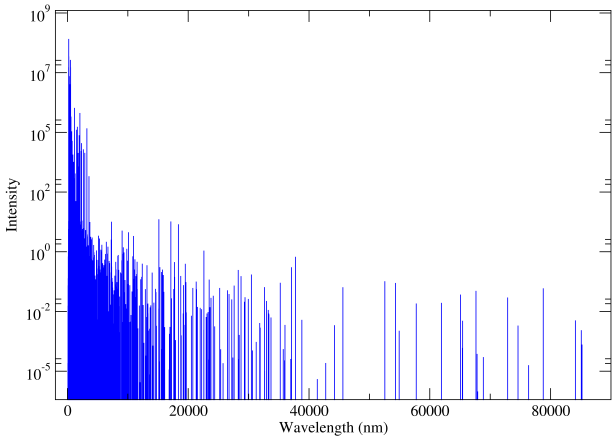

(**a**) Re I

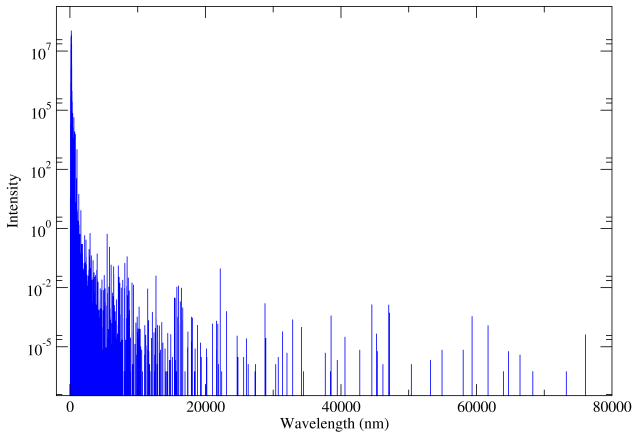

(**b**) Os II

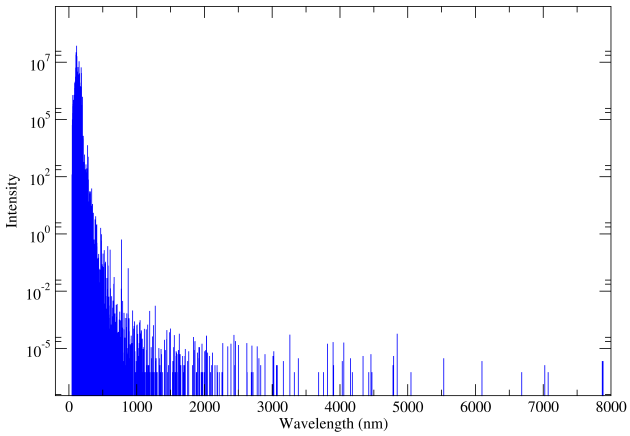

(**c**) Ir III

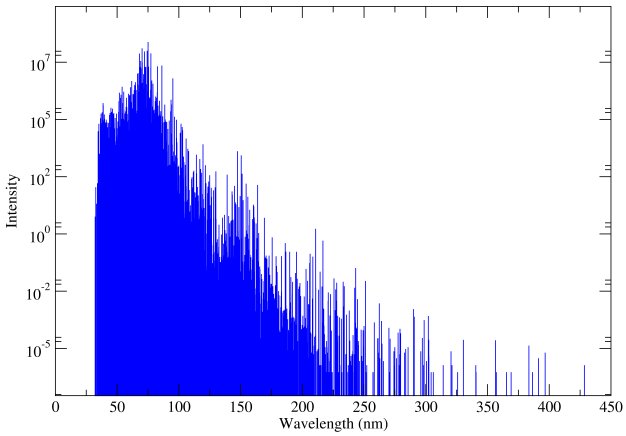

(**d**) Pt IV

Figure 4.4: *Cont.*

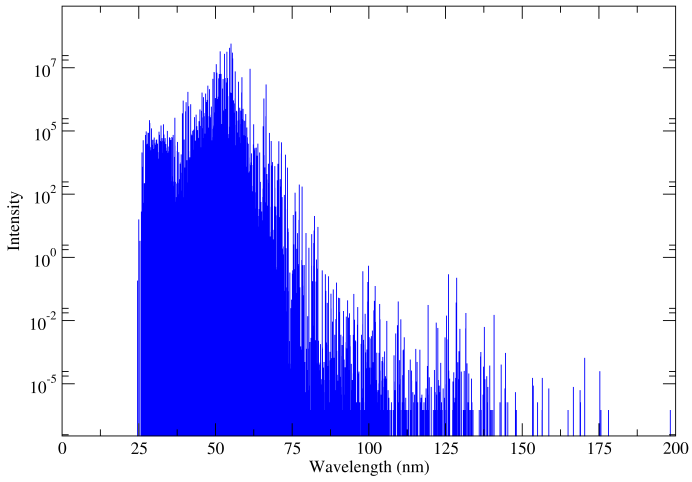

(**e**) Au V

Figure 4.4: LTE spectra at T=5000 for a) Re I, b) Os II, c) Ir III, d) Pt IV, and e) Au V obtained from GRASP2K (5 configurations) calculations.

Table 4.6: Wavelengths of the most intense lines from LTE spectra at 5000 K from GRASP2K calculations.

Re I		
Lower Level	Upper Level	λ(nm)
$5d^5(^6S_5)6s^2\ ^6S$	$5d^4(^5D_4)6s^26p\ ^5P$	208.35
$5d^5(^6S_5)6s^2\ ^6S$	$5d^4(^5D_4)6s^26p\ ^4P$	228.78
$5d^5(^6S_5)6s^2\ ^6S$	$5d^5(^5D_4)6s(^5D)6p\ ^6P$	237.81
Os II		
Lower Level	Upper Level	λ(nm)
$5d^5(^5D_4)6s^2\ ^6D$	$5d^6(^5D_4)6p\ ^6F$	201.12
$5d^5(^5D_4)6s^2\ ^6D$	$5d^5(^4G_5)6s(^5G)6p\ ^6F$	166.82
$5d^5(^5D_4)6s^2\ ^6D$	$5d^5(^4D_5)6s(^5D)6p\ ^6D$	145.16
Ir III		
Lower Level	Upper Level	λ(nm)
$5d^7\ ^4F_3$	$5d^6(^3H_4)6p\ ^4G$	113.15
$5d^7\ ^4F_3$	$5d^6(^3G_4)6p\ ^4F$	105.64
$5d^7\ ^4F_3$	$5d^6(^3P_4)6p\ ^4D$	102.42
Pt IV		
Lower Level	Upper Level	λ(nm)
$5d^7\ ^4F_3$	$5d^6(^3H_4)6p\ ^4G$	75.05
$5d^7\ ^4F_3$	$5d^6(^3G_4)6p\ ^4F$	70.20
$5d^7\ ^4F_3$	$5d^6(^3P_4)6p\ ^4D$	68.12
Au V		
Lower Level	Upper Level	λ(nm)
$5d^7\ ^4F_3$	$5d^6(^3H_4)6p\ ^4G$	55.06
$5d^7\ ^4F_3$	$5d^6(^5D_4)6p\ ^6F$	54.61
$5d^7\ ^4F_3$	$5d^6(^3H_4)6p\ ^4G$	52.93

The expansion opacity, as defined in Kasen et al., 2013, at 3700 K for Re I, Os II, Ir III, Pt IV, and Au V, is shown in Figure 4.5 for all E1 and M1 transitions. We adopt typical values of the kilonova density at $t = 1$ day and include our full line list for each ion: 652 levels and 95,447 transitions. Where experimental data are available, the energies and transition probabilities in our line lists are replaced by these values. The opacity increases to short wavelengths, moves to shorter wavelengths with increase in ion charge, and is dominated by E1 transitions. Opacity due to photoionization will become important for wavelengths shorter than the bound-bound transitions considered here. Importantly, at long wavelengths in the infrared (IR) and mid-infrared (MIR), the density of lines decreases so that individual lines become more apparent. The sparsity of MIR lines increases with ion charge with many due to forbidden M1 fine-structure transitions. As it has been highlighted by Hotokezaka et al., 2022 who focused on NIR M1 transitions including [Os II] 2.78 μm, [Os II] 6.01 μm, [Os III] 2.60 μm, and [W II] 6.05 μm. However, platinum is predicted to have one of the largest abundances in binary neutron star merger nucleosynthesis models (Goriely et al., 2011).

For the Re isoelectronic sequence, Figure 4.5f displays the infrared opacities for 0.6-28.8 μ, the detector window for the *James Web Space Telescope* covered by the Near Infrared Spectrograph (NIRSpec) and the

Mid InfraRed Instrument (MIRI). A number of prominent lines are visible, while Table 4.8 lists the three strongest IR/MIR lines for each element. Except for Re I, the strongest lines are due to fine-structure transitions in the ground term. The late-time kilonova nebular models of Pognan et al., 2022 find that Pt^{2+} and Pt^{3+} dominate the ionization fraction for times greater than 20 days, particularly for models with low ejecta mass ($\lesssim 0.05 M_{\odot}$) and high outflow velocities ($\gtrsim 0.1c$). Future NSM ejecta observations with MIRI/*JWST* should focus on the [Pt IV] 11.291 μm, [Pt IV] 15.872 μm, and [Pt III] 7.07 μm transitions which may prove the best options for a definitive r-process element identification.

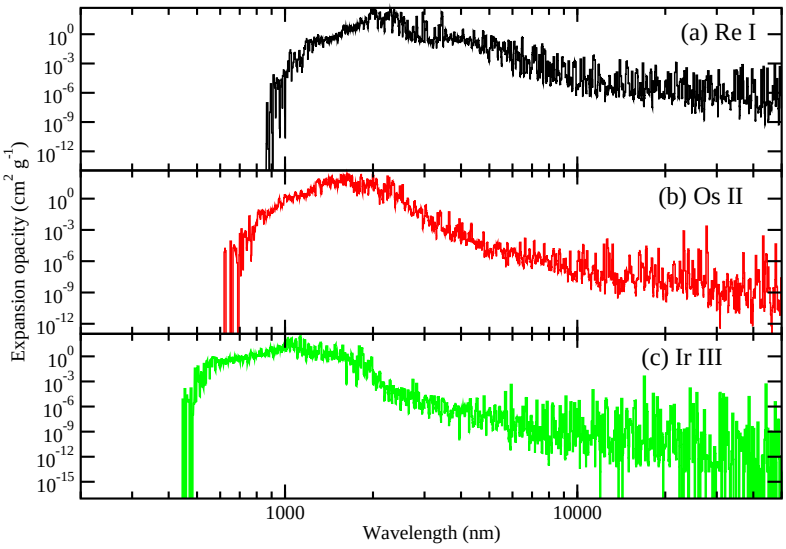

Figure 4.5: *Cont.*

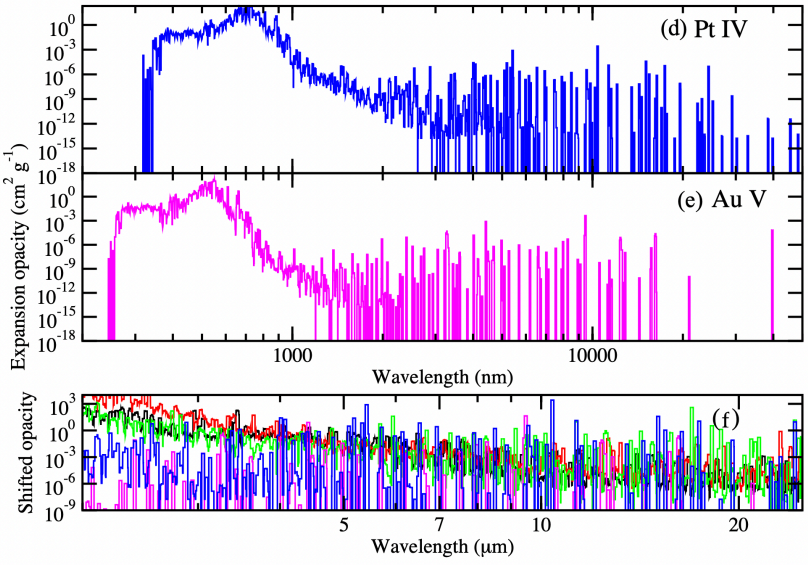

Figure 4.5: Expansion opacity at 1 day for 3700 K and 10^{-13} g/cm^3 for a) Re I, b) Os II, c) Ir III, d) Pt IV, and e) Au V. The opacities in the IR are displayed in f) for all ions but with their magnitudes shifted to enable comparison.

Table 4.7: Weighed transition probabilities (gA-values) of the most intense lines from LTE spectra at 5000 K from GRASP2K calculations compared to Tanaka et al., 2020 (Kato et al., 2021) using HULLAC.

Re I				
Lower Level	Upper Level	GRASP2K	HULLAC	$\%D_i$
$5d^5(^6S_5)6s^2\ ^6S$	$5d^4(^5D_4)6s^26p\ ^6P$	2.41E+09	2.63E+05	99.99
$5d^5(^6S_5)6s^2\ ^6S$	$5d^4(^5D_4)6s^26p\ ^4P$	6.34E+08	4.51E+07	92.88
$5d^5(^6S_5)6s^2\ ^6S$	$5d^5(^4D_5)6s(^5D)6p\ ^6P$	9.36E+08	1.71E+08	81.77
Os II				
Lower Level	Upper Level	GRASP2K	HULLAC	$\%D_i$
$5d^6(^5D_4)6s\ ^6D$	$5d^6(^5D_4)6p\ ^6F$	1.96E+08	2.56E+08	30.61
$5d^6(^5D_4)6s\ ^6D$	$5d^5(^4G_5)6s(^5G)6p\ ^6F$	4.19E+09	5.26E+09	25.44
$5d^6(^5D_4)6s\ ^6D$	$5d^5(^4D_5)6s(^5D)6p\ ^6D$	2.77E+09	2.02E+09	26.88
Ir III				
Lower Level	Upper Level	GRASP2K	HULLAC	$\%D_i$
$5d^7\ ^4F_3$	$5d^6(^3H_4)6p\ ^4G$	9.45E+09	5.58E+08	94.10
$5d^7\ ^4F_3$	$5d^6(^3G_4)6p\ ^4F$	5.78E+09	1.02E+09	82.29
$5d^7\ ^4F_3$	$5d^6(^3P_4)6p\ ^4D$	4.94E+09	7.55E+08	84.71
Pt IV				
Lower Level	Upper Level	GRASP2K	HULLAC	$\%D_i$
$5d^7\ ^4F_3$	$5d^6(^3H_4)6p\ ^4G$	2.55E+10	2.99E+10	17.40
$5d^7\ ^4F_3$	$5d^6(^3G_4)6p\ ^4F$	1.59E+10	1.19E+09	92.48
$5d^7\ ^4F_3$	$5d^6(^3P_4)6p\ ^4D$	1.03E+10	9.30E+09	9.53

$\%D_i$ percent error of GRASP2K and HULLAC.

Table 4.8: Wavelengths of the three most intense IR features at 3700 K. *Wavelength shifted to experimental value.

Re I		
Lower Level	Upper Level	$\lambda(\mu\text{m})$
$5d^5 6s6p\ ^8P(J=5/2)$	$5d^5 6s^2\ ^4G(J=5/2)$	18.494*
$5d^5 6s6p\ ^8P(J=5/2)$	$5d^5 6s^2\ ^4D(J=5/2)$	19.693*
$5d^5 6s6p\ ^6G(J=5/2)$	$5d^6 6s\ ^4D(J=5/2)$	26.677*
Os II		
Lower Level	Upper Level	$\lambda(\mu\text{m})$
$5d^6 6s\ ^6D(J=9/2)$	$5d^6 6s\ ^6D(J=7/2)$	2.7830*
$5d^6 6s\ ^6D(J=3/2)$	$5d^6 6s\ ^6D(J=1/2)$	9.574*
$5d^7\ ^4F_3(J=9/2)$	$5d^7\ ^2G_3(J=9/2)$	16.549*
Ir III		
Lower Level	Upper Level	$\lambda(\mu\text{m})$
$5d^7\ ^4F_3(J=9/2)$	$5d^7\ ^4F_3(J=7/2)$	1.705
$5d^7\ ^4F_3(J=7/2)$	$5d^7\ ^4F_3(J=5/2)$	4.444
$5d^7\ ^4F_3(J=5/2)$	$5d^7\ ^4F_3(J=3/2)$	15.485
Pt IV		
Lower Level	Upper Level	$\lambda(\mu\text{m})$
$5d^7\ ^4F_3(J=9/2)$	$5d^7\ ^4F_3(J=7/2)$	1.045*
$5d^7\ ^4F_3(J=7/2)$	$5d^7\ ^4F_3(J=5/2)$	11.291*
$5d^7\ ^4F_3(J=3/2)$	$5d^7\ ^4P_3(J=5/2)$	15.872*
Au V		
Lower Level	Upper Level	$\lambda(\mu\text{m})$
$5d^7\ ^4F_3(J=9/2)$	$5d^7\ ^4F_3(J=7/2)$	0.952
$5d^7\ ^4F_3(J=5/2)$	$5d^7\ ^4F_3(J=3/2)$	1.625
$5d^7\ ^4F_3(J=7/2)$	$5d^7\ ^4F_3(J=5/2)$	3.989

4.2 Summary

New atomic structure calculations have been performed for Re I (Z=75), Os II (Z=76), Ir III (Z=77), Pt IV (Z=78), and Au V (Z=79) to construct atomic data for r-process elements. By using two different atomic code packages, GRASP2K and GRASP^0, energy levels and transition probabilities (E1 and M1) for the above ions were obtained and compared to experimental and prior theoretical data, which are sparse in all considered ions of the Re isoelectronic sequence.

The results are used to compute LTE emission spectra and sample expansion opacities typical of binary neutron star merger ejecta conditions. A list of the strongest transitions are given for each ion in the UV for E1 transitions and in the IR for M1 transitions. It is pointed out that the possible identification of r-process elements will be easier in the infrared, especially in the MIR in the nebula phase of a kilonova since the M1 lines are far less crowded in this spectral window. Strong M1 lines of Pt IV at 11.291 and 15.872 μm and Pt III at 7.07 μm are suggested as ideal candidates to detect the existence of a r-process element in a kilonova with future MIRI/*JWST* observations.

Chapter 5

Photoionization cross section calculations of W I, W II, W III, & W IV

The electron emission is one of the most efficient decay mechanisms for atoms or molecules excited above the ionization threshold. This makes the knowledge of reliable photoionization cross sections very valuable in a variety of fields. Low-Z species have relatively simple atomic structure when compared to high-Z species, hence the more accurate and reliable data are available for the atoms/ions with lower atomic number.

High-Z species have complicated atomic structure. Therefore, near neutral systems require large complicated quantum calculations to model accurately such as the R-matrix method (P. Burke & Taylor, 1975) or the distorted wave (DW) approach (Badnell, 2011c). photoionization (PI) cross sections are necessary for the computation of ionization balance in astrophysical plasmas. Also, as it is mentioned by Barnes et al., 2016, PI becomes important at lower energies ($\leq$ 1 MeV) in kilonova ejecta a day after the merger. A number of calculations exist for PI cross sections for ions of elements with relatively low atomic number ($Z \leq 54$) (Ichihara & Eichler, 2000; Trzhaskovskaya et al., 2008). However, there are few calculations of PI cross section for ions as heavy as tungsten.

In addition to scientific interest of the Tungsten in nuclear-fusion research, it is one of the heavy elements which are produced in a binary neutron star merger. With this motivation, the PI cross section of neutral, singly, doubly and triply charged Tungsten (W, W^{+}, W^{+2}, and W^{+3}) for photon energies from 10s of eV to 10 MeV was calculated and compared against available theoretical and experimental data.

5.1 Computation

For computing the PI cross section AUTOSTRUCTURE was applied which has been explained in 2.5.3. In the PI process for all the Tungsten ions, it is considered that the ion is in its ground state, as shown in Table 5.1, before ionization and it is being ionized from all the inner shells, 6*s* to 1*s*.

Table 5.1: Ground states of Tungsten ions

ion	Ground State
W I	$[Xe]4f^{14}5d^{4}6s^{2}(^{5}D)$
W II	$[Xe]4f^{14}5d^{4}6s(^{6}D)$
W III	$[Xe]4f^{14}5d^{4}(^{5}D)$
W IV	$[Xe]4f^{14}5d^{3}(^{4}F)$

The computation was carried out at the ejected electron energy up to 10^4 Ryd for both LS coupling and configuration average. There are 14 configurations for ionized W and W^+ ions, and 13 configurations for ionized W^{+2} and W^{+3} since $6s$ is not occupied in these ions. In order to calculate the photon energy, the ionization potential of all the inner shells was computed. In the case of LS coupling, 758 ionization levels for W, 472 ionization levels for W^+, 734 ionization levels for W^{+2}, and 507 ionization levels for W^{+3} were computed. Figure 5.1 shows the ionization potential of all the inner shells for W, W^+, W^{+2}, and W^{+3} on a logarithmic scale. These ionization potentials are computed based on the configuration average that only contains nl-terms. Comparing the calculated ionization potentials with Thompson, Vaughan, et al., 2001, the percent difference in binding energies at the shells close to the core, like $1s$ and $2s$, is less than 10%. However, at the higher shells, like $5s$, the percent difference increases up to 50%.

In the range of the ejected electron energy, 50-mesh points were considered. Having the ionization potentials from all the shells, the PI cross sections at any photon energy can be calculated by summing up over all the PI cross sections from the ground state to the specific final state which includes the ejected electron in different continuum orbitals up to the g orbital.

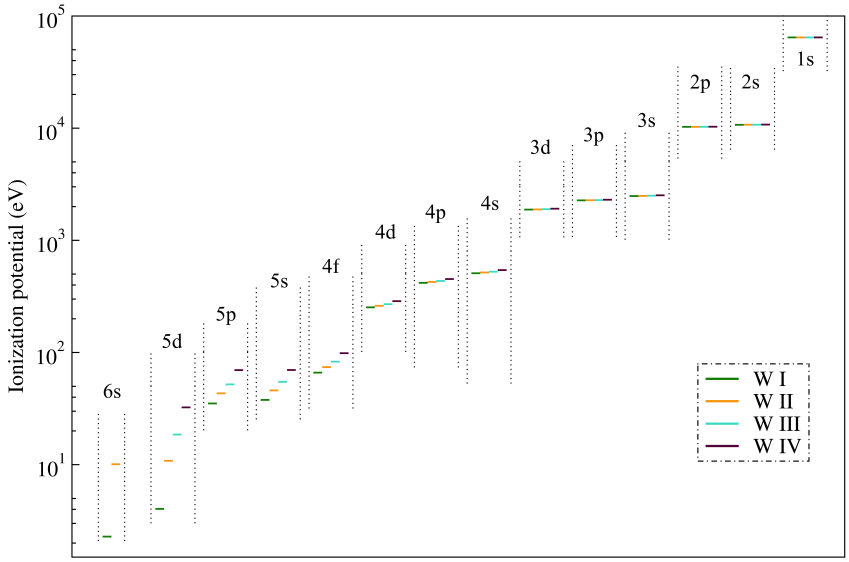

Figure 5.1: Ionization potential of all inner shells for W I, W II, W III, and W IV.

5.2 Results and discussion

Figure 5.2 presents the calculated cross section for W, W^{+}, W^{+2}, and W^{+3} from configuration average. Each edge in the cross section represents ionization of an electron from specific shell. For W and W^{+} the ionization starts from $6s$ subshell, unlike W^{+2} and W^{+3} that starts from $5d$. As it can be seen from Figure 5.2, the first edge of cross section for W and W^{+} happens near $50 - 60$ eV, and the first one for W^{+2} and W^{+3} is around $110 - 120$ eV.

Comparing the photon energy in Figure 5.2 with ionization potentials in Figure 5.1, while the background ionization cross section drops as $1/nu^3$, the rises rapidly at each ionization edge. The ejected electron kinetic energy is zero at the edge, but increases with photon energy..

Beyond $120 - 130$ eV, the calculated cross sections rapidly drop and have the same pattern for all the Tungsten ions.

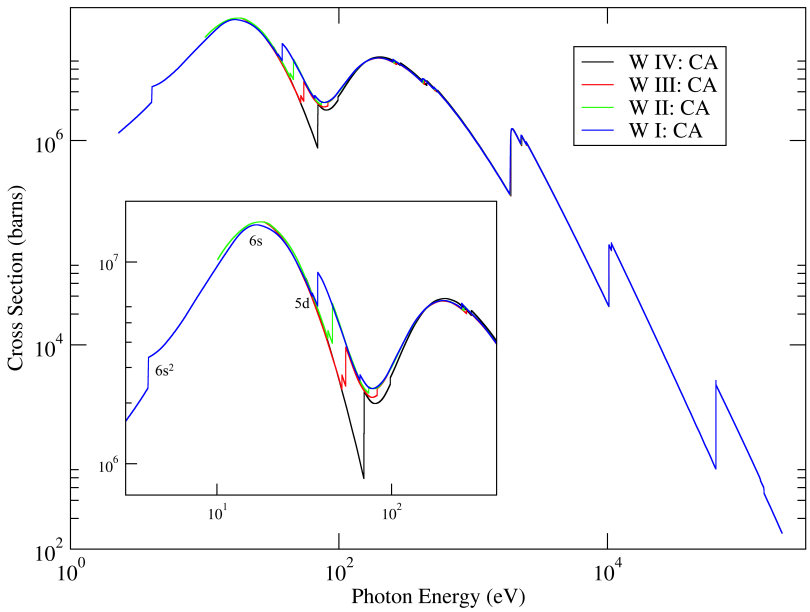

Figure 5.2: Comparison of W I, W II, W III, and W IV cross sections from configuration average.

Figure 5.3 shows the computed PI cross section for the neutral Tungsten on a double-logarithmic scale compared with available theoretical and experimental data. The overall results from both configuration average and LS-coupling are in a good agreement with NIST XCOM (Berger et al., 2009) and Ballance and McLaughlin, 2015 R-matrix calculation. Also, the vertical blue lines indicate the ionization potential around the edges.

Configuration average cross section has higher value comparing to LS-coupling, the reason to this pattern could be the selection rules for the dipole transition. In the LS-coupling, the number of possible electronic transitions would be reduced due to the selection rules which are applied to J quantum number and S quantum number.

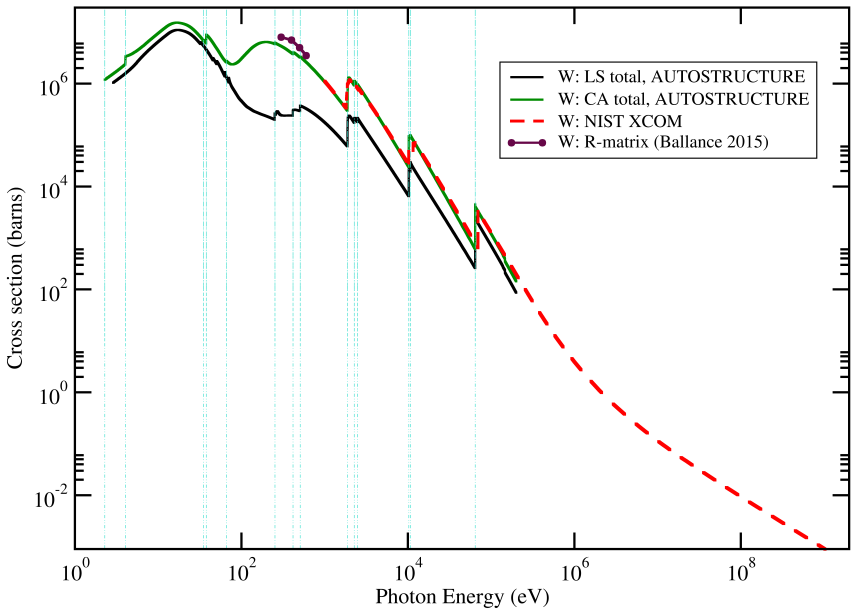

Figure 5.3: Total configuration average (CA) and LS-coupling (LS) PI cross section of W I compared with NIST XCOM (Berger et al., 2009) and R-matrix calculation (Ballance & McLaughlin, 2015).

Figure 5.4 illustrates the results for W^+ on a double-logarithmic scale and the comparison has been made with Müller et al., 2015 experimental and R-matrix calculation data, and the vertical lines indicate the ionization potentials. The general pattern of all the PI cross sections are the same. however, difference can be seen at lower photon energy, below 100 eV. As it is described in Müller et al., 2015, in their calculations the first excited terms were also considered that can be neglected at higher photon energy where the focus of our work is.

The experimental or calculated data for PI cross section of heavy elements like Tungsten is limited, specifically at high photon energy ($h\nu > 200$ eV). Hence, there was no available data for W^{+2} and W^{+3} to be compared with.

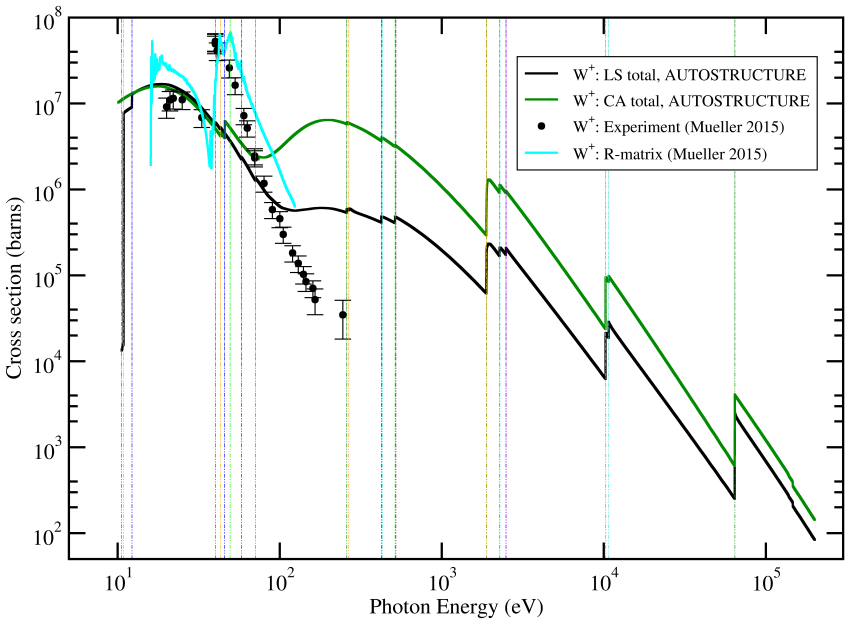

Figure 5.4: Total configuration average (CA) and LS-coupling (LS) PI cross section of W II compared with experimental results and R-matrix calculation drawn from Müller et al., 2015.

Comparing the computed PI cross section with available experimental data suggests that for detailed modeling, adding the lowest excited states to the calculation is required.

5.3 Summary

We presented theoretical photoionization cross sections for W, W^{+}, W^{+2}, and W^{+3}. We obtained AUTOSTRUCTURE, and performed both LS coupling and configuration average (CA) calculations. Also, only photoionization from ground states was considered.

We found that the PI cross sections from CA calculation have larger values compared to LS coupling calculation due to missing some of the transitions.

Although the available data was limited in the case of Tungsten ions, the results are reasonably well reproduced by our calculations.

Chapter 6

Dielectronic recombination of Li-like and Be-like Oxygen

Understanding the spectral and thermal properties of plasmas requires an accurate knowledge of the ionization level of the gas. Dielectronic recombination (DR) rates are essential for accurate determinations of ionization parameters. However, there are large uncertainties on currently available DR rates, particularly for elements beyond the second row of the periodic table. A majority of the theoretical and experimental efforts to determine DR rate coefficient data have been focused on the high temperature astrophysical region. DR data for the low temperature, where photoionization is dominant, remains sparse theoretically due to many-body configuration interaction effects and experimentally due to the need to produce small electron-ion relative velocities in the laboratory.

The DR process can be described by 2.7, the free electron can be treated in different ways. The first is the electron can be captured into Rydberg states where it does not interact with other electrons in the ion. The second is the electron is captured into the core n-shell and is allowed to interact with the other electrons.

Most of the atomic structure codes that calculate DR rate coefficients employ a central field approximation for the potential for generating the orbital wavefunctions. There are a range of central field potentials as mentioned in 2.4.2, however, this approximation can not accurately account for the many body effects due to the Coulomb repulsion between the electrons which becomes important in low energy resonances. This problem can be addressed by using multi-configuration methods.

The aim of this work was to improve low-temperature DR rate coefficients. A range of calculations have been done for Li-like Oxygen (O^{+5}) and Be-like Oxygen (O^{+4}) recombination, then compared with available experimental and archived data.

6.1 Computation

AUTOSTRUCTURE was applied within ADAS, as it has been discussed in 2.5.3, to calculate the total DR rate coefficients. Since the focus of this work was on the low temperature regime, we started with computing doubly-excite states that are present near the ionization threshold. In order to get accurate energies for these states, pseudostates and large configuration-interaction calculations were applied.

6.1.1 Pseudostates

In theory, an electron that is not bound to the nucleus should be able to have any positive energy. However, due to the fact that the basis sets for computation are finite, only a finite number of positive energy states can be described in the calculation. These are an approximation to the continuum, and unlike the bound states, these states are not physical. These discrete positive energy states are referred to as *"pseudostates"*.

The doubly excited states which are near threshold can interact with continuum states, this configuration-interaction can be included by using the pseudostates. In AUTOSTRUCTURE this method can be used with orthogonal Laguerre pseudo-orbitals.

6.1.2 Large configuration-interaction

In multi-configuration atomic structure calculations the accuracy of the structure can be improved by increasing the number of configurations. A code was developed to generate lists of configurations and produce the input files that AUTOSTRUCTURE can use.

Using the results from both pseudostates and large configuration-interaction methods, the total DR rate coefficients were computed via an ADAS post-processing code. In addition to produce the DR resonances at specific electron energies, the ADAS post-processing code was also used to convolve the Maxwellian DR rate coefficients as a function of electron temperature.

In order to compare the computed results with other experimental and calculated data, the calculated target energies in this work have been shifted to the observed energies in the NIST database (Kramida et al., 2018). The shifting process can be applied in different ways using AUTOSTRUCTURE, two methods were used in this work. The first, the target energies were shifted to the NIST values in the post-processing code where the DR rates were computed. The second, the *ECORIC* flag was used in the default AUTOSTRUCTURE calculation. In this flag, the energy correction will be applied to all target continuum. If the value has been chosen negative, the flag will lower all the target ionization states by that value.

6.2 Results and discussion

The total DR rate coefficients were computed for Li-like and Be-like Oxygen for $2 \rightarrow 2$ core excitations where it can be written as

$$e + O^{+5}(1s^2 2s; 1s^2 2p) \rightarrow \left\{ \begin{array}{l} O^{+4}(1s^2 2snl) \\ O^{+4}(1s^2 2pnl) \end{array} \right\} \rightarrow O^{+4} + h\nu \tag{6.1}$$

for Li-like Oxygen, and

$$e + O^{+4}(1s^2 2s^2; 1s^2 2s2p; 1s^2 2p^2) \rightarrow \left\{ \begin{array}{l} O^{+3}(1s^2 2s^2 nl) \\ O^{+3}(1s^2 2s2pnl) \\ O^{+3}(1s^2 2p^2 nl) \end{array} \right\} \rightarrow O^{+3} + h\nu \tag{6.2}$$

for Be-like Oxygen. The calculations were performed using the Thomas-Fermi-Dirac-Amaldo (TFDA) and Hartree-Fock potential, and all $0 \leq l \leq 7$ and $3 \leq n \leq 1000$ were included.

Table 6.1 and Table 6.2 list some of the excitation energy of O^{+4} and O^{+3}, respectively. In the case of the pseudostates calculation, the pseudostates start from $7s$.

The calculated O^{+5} DR spectrum has been plotted in Figure 6.1, and some of the resonance energies are listed in Table 6.1. The energy region for the spectrum is between 0 and 12 eV where the largest disagreement is between different calculations method in addition to storage ring experiment. The results show the Hartree potential is better than TFDA and pseudo calculation. In the case of Hartree potential, the excitation energies near the threshold being on average 0.05 eV different from the NIST values. However, the TFDA potential and pseudo calculations are on average 0.5 eV and 1.47 eV different from the NIST values, respectively. Also, the Hartree potential resonances differ from the NIST by 0.04 eV on average, while TFDA potential and pseudo calculation resonances differ by 0.10 eV and 0.25 eV, respectively.

The computed DR Maxwellian rate coefficients of O^{+5} as a function of electron temperature for the TFDA and Hartree potential, and pseudo calculation are shown in Figure 6.2. The comparison has been made with the available experimentally derived DR rate coefficients by Böhm et al., 2003 and calculated DR rate coefficients by Colgan et al., 2004, and AUTOSTRUCTURE database (Badnell, 2011a). Although in the case of TFDA potential and pseudostates calculation the results are not accurate enough, the Hartree potential shows good agreement with experiment and archived data. The errors are 0.10 eV for TFDA potential, 0.04 eV for Hartree potential, and 0.25 eV for pseudostates calculation.

Table 6.1: Excitation and DR resonance Energies of Be-like O (O V) in eV, comparing NIST (Kramida et al., 2018) and three AUTOSTRUCTURE calculations. The DR resonance energies are relative to the ionization potential.

ionization energy		113.8990	113.3222	113.8780	112.1743				
		Excitation energy				DR resonance energy			
Configuration	J	NIST	TFDA	Hartree	Pseudo	NIST	TFDA	Hartree	Pseudo
$1s^2 2p6p\ ^1P$	1	115.93676	115.46092	115.87955	114.44730	2.03776	2.13864	2.00148	2.27294
$1s^2 2p6p\ ^3D$	3	116.01983	115.54696	115.95912	114.54545	2.12083	2.22468	2.08105	2.37109
$1s^2 2p6p\ ^3P$	2	116.12645	115.64572	116.06374	114.65622	2.22745	2.32344	2.18567	2.48186
$1s^2 2p6p\ ^1D$	2	116.21547	115.74404	116.16949	114.76674	2.31647	2.42176	2.29142	2.59238
$1s^2 2p7p\ ^3D$	3	118.69144	118.21693	118.62884	–	4.79244	4.89465	4.75077	–
$1s^2 2p7p\ ^3P$	2	118.69144	118.27493	118.6900	–	4.85889	4.95265	4.81190	–
$1s^2 2p7d\ ^3D$	3	118.90246	118.42171	118.82788	–	5.00346	5.09943	4.94981	–

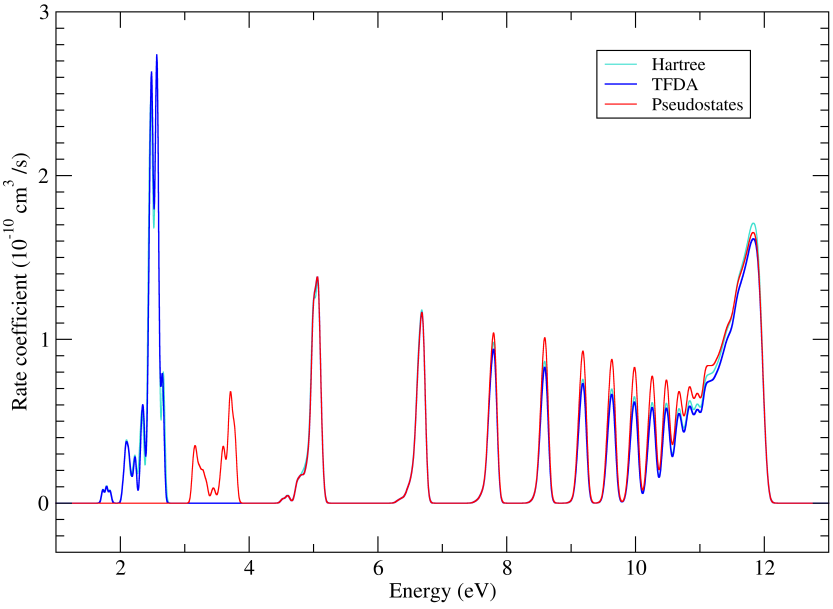

Figure 6.1: The calculated DR spectrum for O VI.

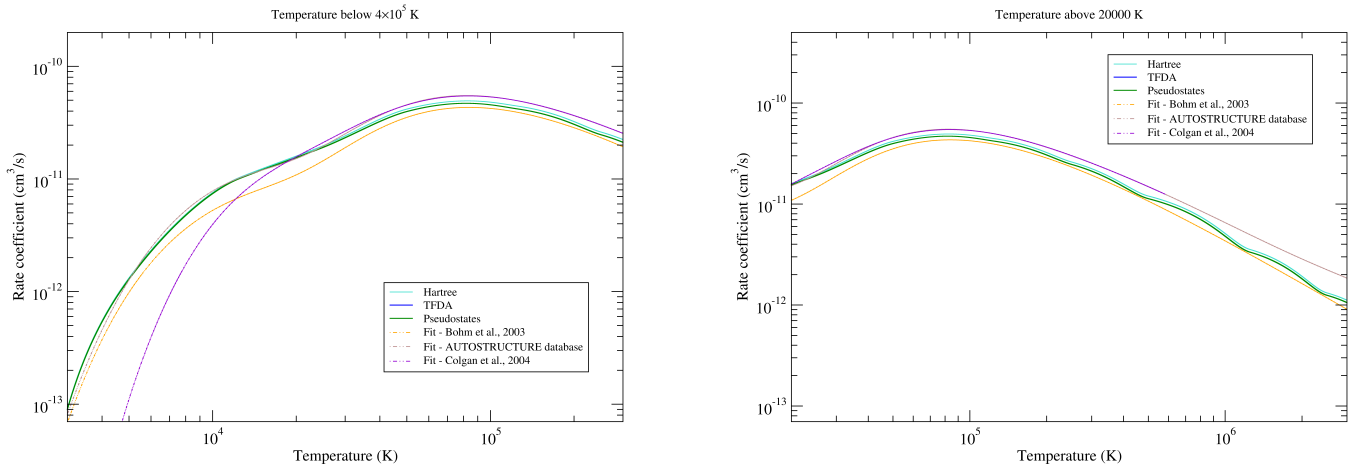

(**a**) (**b**)

Figure 6.2: DR Maxwellian rate coefficients of O VI for temperatures a) below 4×10^5 K and b) for temperatures above 2×10^4 K compared with Böhm et al., 2003 experimental results, Colgan et al., 2004 calculated data, and AUTOSTRUCTURE database (Badnell, 2011a).

The calculated O^{+4} DR spectrum has been shown in Figure 6.3 for the TFDA and Hartree potential, and pseudo calculation. Comparison was made with available experimental data from storage ring measurements (Loch, 2022). A sample of results are shown in Table 6.2, the excitation energies of TFDA and Hartree potential, and pseudo calculation differ from NIST values on average by 0.57 eV, 0.66 eV, and 1.75 eV, respectively. Although the excitation energies with the TFDA and Hartree potential are in better agreement with NIST data compare to pseudo calculation, pseudo calculation results are better in DR resonance energies near the threshold. However, in general the results from all the cases are still not accurate enough compare to NIST, the errors are 0.94 eV for TFDA potential, 1.47 eV for Hartree potential, and 1.05 eV for pseudostates calculation.

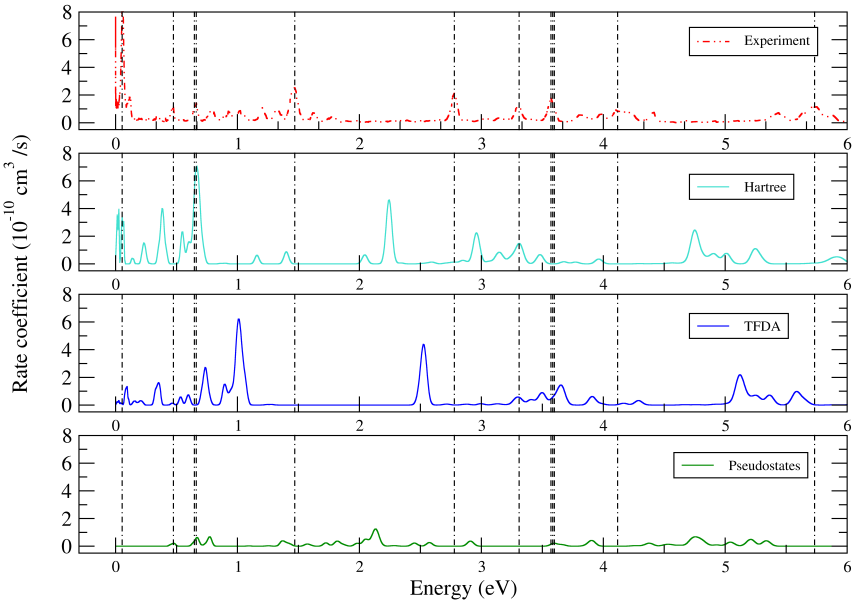

Figure 6.3: The calculated DR spectrum for O V compared to experiment (Loch, 2022).

In the case of Be-like Oxygen recombination, the autoionizing levels are close to ionization threshold, if the captured electron is recombined to these levels the electron-electron correlation between the Rydberg electron and the core electron shells becomes significant. As a consequence, at low energies the atomic structure for these resonances are more challenging to calculate accurately.

Table 6.2: Excitation energies of B-like O (O IV) and DR resonance energies for Be-like O (O V) in eV, comparing NIST (Kramida et al., 2018) and three AUTOSTRUCTURE calculations. The DR resonance energies are relative to the ionization potential.

ionization energy		77.41350	76.90474	76.55909	78.20306				
		Excitation energy				DR resonance energy			
Configuration	J	NIST	TFDA	Hartree	Pseudo	NIST	TFDA	Hartree	Pseudo
$1s^2 2p^2 3p\ ^2F$	7/2	77.4747	78.1646	78.0154	79.0191	0.0612	1.2599	1.4563	0.8160
	5/2	77.4747	78.1598	78.0080	79.0084	0.0612	1.2551	1.4489	0.8053
$1s^2 2s 2p 5p\ ^2P$	3/2	77.9289	77.6450	77.6304	79.3481	0.5154	0.7403	1.0713	1.1450

Continued on next page

Configuration	J	Excitation energy				DR resonance energy			
		NIST	TFDA	Hartree	Pseudo	NIST	TFDA	Hartree	Pseudo
$1s^2 2p^2 3d\ ^2F$	7/2	78.1218	78.7861	79.1599	79.6346	0.7083	1.8814	2.6008	1.4315
	5/2	78.1218	78.7523	79.1267	79.6003	0.7083	1.8476	2.5676	1.3972
$1s^2 2s 2p 5p\ ^2D$	3/2	78.1904	77.8695	77.9130	79.6533	0.7769	0.9648	1.3539	1.4502
	5/2	78.2190	77.8974	77.9406	79.6832	0.8055	0.9927	1.3815	1.4801
$1s^2 2p^2 3p\ ^2D$	3/2	78.3472	78.8697	80.3570	80.6700	0.9337	1.9650	3.7979	2.4669
$1s^2 2p^2 3d\ ^2P$	3/2	78.4108	78.0449	78.4001	79.8058	0.9973	1.1402	1.8410	1.6027
	1/2	78.4320	78.0686	78.4235	79.8178	1.0185	1.1639	1.8644	1.6147
$1s^2 2s 2p 5d\ ^4D$	7/2	78.6285	78.2727	78.2708	80.0748	1.2150	1.3680	1.7117	1.8717
$1s^2 2s 2p 5d\ ^4P$	5/2	78.6708	78.3078	78.3046	80.1154	1.2573	1.4031	1.7455	1.9123
	3/2	78.6831	78.3161	78.3124	80.1262	1.2696	1.4114	1.7533	1.9231
	1/2	78.6869	78.3213	78.3175	80.1323	1.2734	1.4166	1.7584	1.9292
$1s^2 2s 2p 5d\ ^2F$	5/2	78.8611	78.5377	78.5512	80.3787	1.4476	1.6330	1.9921	2.1756
	7/2	78.8828	78.5637	78.5767	80.4083	1.4693	1.6590	2.0176	2.2052
$1s^2 2p^2 3d\ ^4P$	5/2	78.9919	78.5465	78.9484	80.4765	1.5784	1.6418	2.3893	2.2734
	3/2	79.0042	78.5595	78.9610	80.4902	1.5907	1.6548	2.4019	2.2871
	1/2	79.0119	78.5670	78.9683	80.4985	1.5984	1.6623	2.4092	2.2954
$1s^2 2p^2 3d\ ^2G$	7/2	79.8014	81.4036	81.7947	81.9119	2.38790	4.4989	5.2356	3.7088
	9/2	79.8014	81.4055	81.7967	81.9139	2.38790	4.5008	5.2376	3.7108
$1s^2 2p^2 3d\ ^2D$	5/2	80.2003	80.0328	80.5070	82.1581	2.7868	3.1281	3.9479	3.9550
	3/2	80.2003	80.0254	80.5000	82.1594	2.7868	3.1207	3.9409	3.9563
$1s^2 2p^2 3d\ ^2F$	5/2	80.7259	81.6877	82.1689	83.4639	3.3124	4.7830	5.6098	5.2608
	7/2	80.7282	81.6823	82.1588	83.4653	3.3147	4.7776	5.5997	5.2622
$1s^2 2p^2 3d\ ^2D$	5/2	81.0023	81.7201	82.1551	–	3.5888	4.8154	5.5960	–
	3/2	81.0126	81.7127	82.1520	–	3.5991	4.8080	5.5929	–

Continued on next page

Configuration	J	Excitation energy				DR resonance energy			
		NIST	TFDA	Hartree	Pseudo	NIST	TFDA	Hartree	Pseudo
$1s^2 2s 2p 6d\ ^4D$	7/2	81.4069	81.0387	81.0405	82.8717	3.9934	4.1340	4.4814	4.6686
$1s^2 2s 2p 4p\ ^2D$	3/2	81.4260	82.4594	82.3729	83.5804	4.0125	5.5547	5.8138	5.3773
	5/2	81.4312	82.4609	82.3745	83.5904	4.0177	5.5562	5.8154	5.3873
$1s^2 2s 2p 6d\ ^2F$	5/2	81.5160	81.1801	81.1901	83.0026	4.1025	4.2754	4.6310	4.7995
	7/2	81.5453	81.2054	81.2149	83.0313	4.1318	4.3007	4.6558	4.8282
$1s^2 2p^2 3d\ ^2P$	1/2	81.8293	82.3965	82.8653	84.3421	4.4158	5.4918	6.3062	6.1390
	3/2	81.8293	82.4041	82.8732	84.3522	4.4158	5.4994	6.3141	6.1491
$1s^2 2s 2p 4d\ ^2D$	5/2	82.8900	83.6605	83.6388	84.6301	5.4765	6.7558	7.0797	6.4270
	3/2	82.8905	83.6595	83.6376	84.6286	5.4770	6.7548	7.0785	6.4255
$1s^2 2s 2p 7d\ ^4D$	7/2	83.0328	82.6392	82.6402	–	5.6193	5.7345	6.0811	–
	5/2	83.0328	82.6263	82.6276	–	5.6193	5.7216	6.0685	–

In the case of the TFDA and Hartree potential, only the configurations in Eq. 6.1 and Eq. 6.2 were considered in the recombined ions. In pseudostates calculation the same configurations as Eq. 6.1 and Eq. 6.2 were considered but the limit of maximum nl-shell was 8*d* where the pseudo states started from 7*s*.

In multi-configuration atomic structure calculations the number of configurations were increased where beyond the $2 \rightarrow 2$ core excitations, the excitation to other shells were also included. By increasing the number of configurations, more atomic state functions can interact to build more accurate atomic structure near the threshold. However, in the DR rate calculation, all the excitations except the $2 \rightarrow 2$ core excitations were removed since we do not expect to have higher core excitations at low energies.

Figure 6.4 shows two examples of large configuration-interaction calculations compared with experimental data from storage ring measurements (Loch, 2022). In these calculations all the possible configurations up to 8*g* and 10*g* were considered.

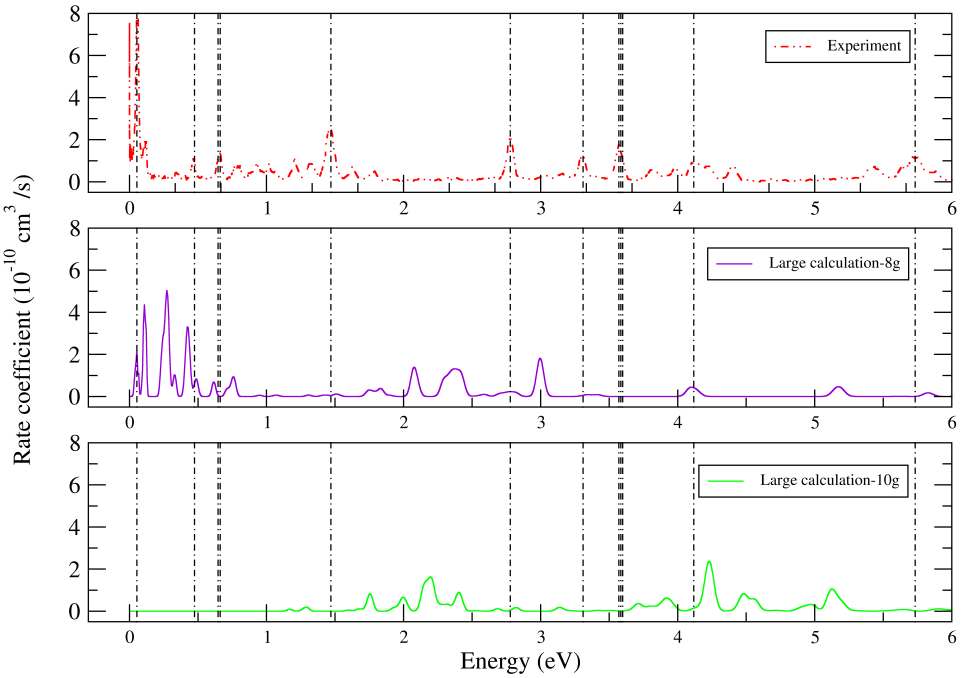

Figure 6.4: The calculated DR spectrum for O V using large configuration-interaction calculations compared to experiment (Loch, 2022).

The Maxwellian rate coefficients from large configuration-interaction calculations, TFDA and Hartree potential, and pseudo calculations were compared with the available experimental and calculated results in Figure 6.5.

As it is expected all the calculations converge at high temperature, However, they differ at low temperature. Although there is a difference, the general pattern has been produced by TFDA and Hartree potential, and large configuration-interaction calculations.

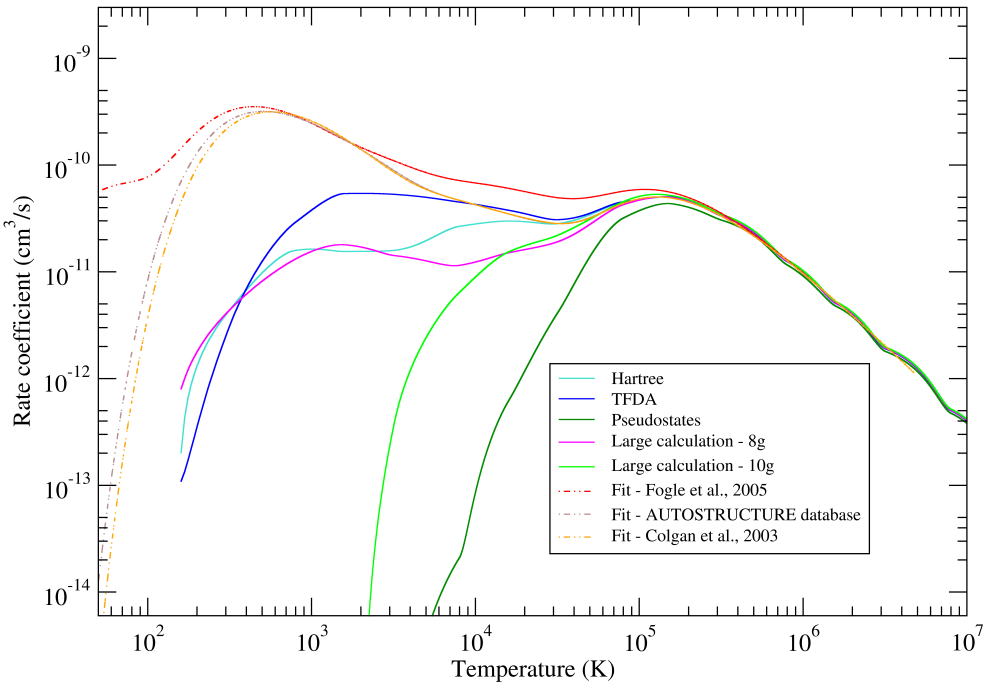

Figure 6.5: DR Maxwellian rate coefficients of O V compared with Fogle et al., 2005 experimental results, Colgan et al., 2003 calculated data and AUTOSTRUCTURE database (Badnell, 2011a).

It has been mentioned in the section 6.1 that two approaches were used to shift the target energies. We found that by shifting the continuum energies, the better resonance may be possible at specific values. Figure 6.6 indicates some of the shifting values and their DR resonances where compared to the storage ring experiments. Also, corresponding DR Maxwellian rate coefficients are shown in Figure 6.7 where comparison made to the available experimental and calculated data.

The reason for getting better resonance in this case is that since the autoionizing states are close to the threshold, some of them may be calculated below the threshold. As a result, there can not be resonances due to those states. By using ECORIC and shifting the continuum energies, getting resonances from some of those states becomes possiible.

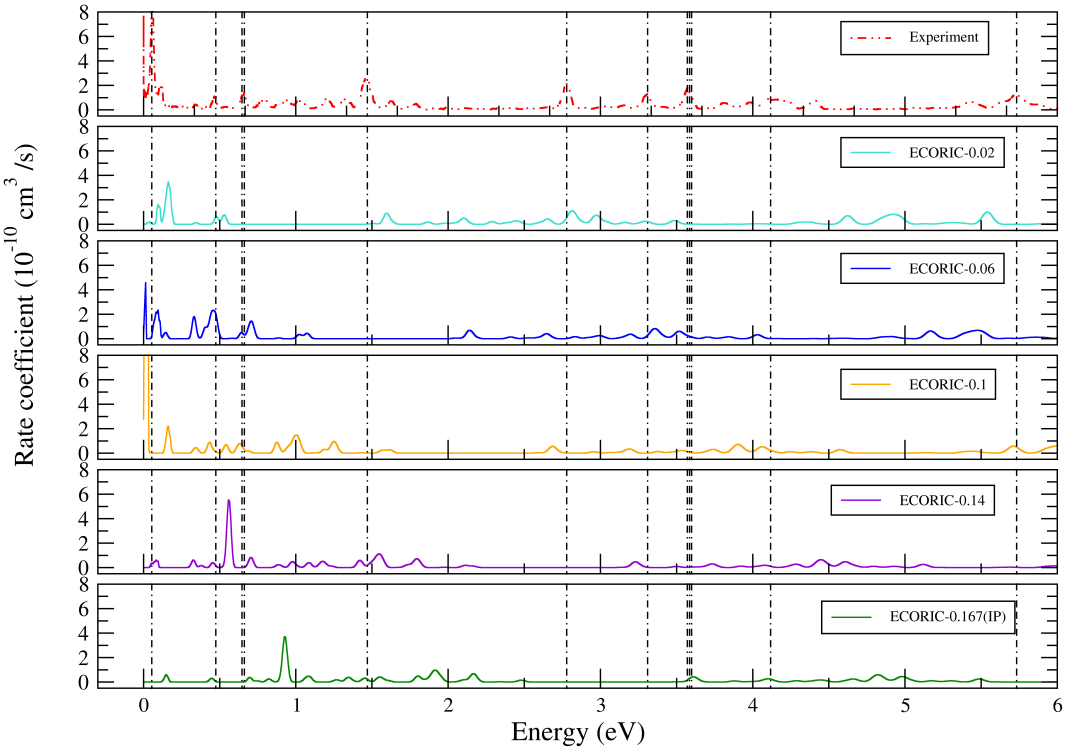

Figure 6.6: The calculated DR spectrum for O V for different ECORIC values.

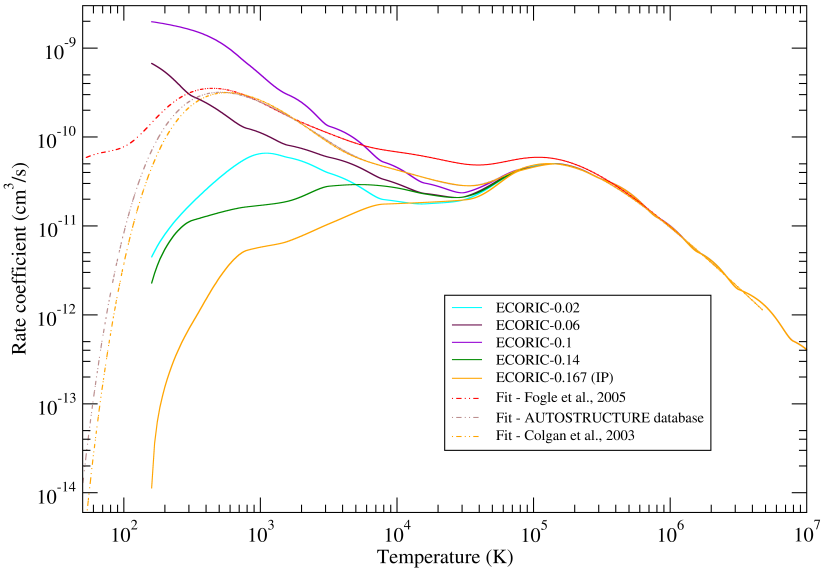

Figure 6.7: DR Maxwellian rate coefficient of O V compared with Fogle et al., 2005 experimental results, Colgan et al., 2003 calculated data and AUTOSTRUCTURE database (Badnell, 2011a).

6.3 Summary

We have computed total DR rate coefficients for Li-like and Be-like Oxygen in low temperature. The calculation were performed using AUTOSTRUCTURE with two approaches: the use of pseudostates and the use of large configuration-interaction calculations.

The present DR rate coefficients for Li-like Oxygen agree well with experiment and other calculations. In Be-like Oxygen, although the data agree with experiment and other calculations in high temperature, we see considerable disagreement at low temperature.

For plotting total DR rate coefficients, we shifted the target energies to the NIST values. However, we found if we shift the recombined ion energies, we may get better result.

Chapter 7

Conclusions, summary, futurework

7.1 Summary and conclusions

This work has extended the atomic datasets mostly for heavy elements which can be applied not only to experiments but also spectral analysis observed from astrophysical objects in the universe.

We have performed new atomic structure calculations for Os I (Z = 76), Ir II (Z = 77), Pt III (Z = 78), Au IV (Z = 79), Hg V (Z = 80), Re I (Z=75), Os II (Z=76), Ir III (Z=77), Pt IV (Z=78), and Au V (Z=79) to construct atomic data for r-process elements. By using two different atomic code packages, GRASP2K and GRASP^0, energy levels and transition probabilities (E1 and M1) for the above ions were obtained and compared to experimental and prior theoretical data, which are sparse in the case of the Re isoelectronic sequence.

The results are used to compute LTE emission spectra and sample expansion opacities typical of binary neutron star merger ejecta conditions. A list of the strongest transitions are given for each ion in the UV for E1 transitions and in the IR for M1 transitions. It is pointed out that the possible identification of r-process elements will be easier in the infrared, especially in the near- to mid-IR in the nebula phase of a kilonova since the M1 lines are far less crowded in this spectral window. Strong M1 lines of Pt IV at 11.291 and 15.872 μm and Pt III at 7.07 μm are suggested as ideal candidates to detect the existence of a r-process element in a kilonova with future MIRI/*JWST* observations.

The calculated data are made available in standard formats for use in the modeling of neutron star mergers at https://www.physast.uga.edu/ugamop/index1.html.

We have obtained a set of results for the photoionization cross section of ground levels of W I, W II, W III, and W IV. The AUTOSTRUCTURE code was employed for the calculation and the results were compared with available experimental measurements and other theoretical calculations. However, the data on Tungsten in the region of our calculation are limited. Considering the complexity in the

calculation PI cross section of the above ions due to open 5d shell, the main features of the PI cross section are reasonably well reproduced. Specifically in the case of W^+ where electron–electron correlation effects are expected to be strong in comparison to other more highly charged tungsten ions.

We have described calculations of dielectronic recombination data for the Li-like and Be-like Oxygen as part of an assembly of a dielectronic recombination database necessary for the modeling of astrophysical plasmas. Specifically, our focus was at low temperature where there are large uncertainties in experiments and different theoretical calculations. The AUTOSTRUCTURE code was used to compute the DR rate. In order to improve atomic structure, two approaches were explored: Large configuration-interaction calculations and pseudostates.

We found that the Li-like Oxygen already has relatively small uncertainties compared to Be-like Oxygen. It might be due to the fact that the Li-like Oxygen is a single-valence electron atom, hence the central potential approximation applied in the AUTOSTRUCTURE works well in this case. Thus, we expect the existing archived DR rates for Li-like ions to be of reasonable accuracy and it may be difficult to improve upon the resonance positions. For temperatures above 3,000 K (approximately 0.25 eV), the uncertainties are all less than 10% and all the approaches converge.

In this case of Be-like Oxygen the uncertainties are larger, with values in the 1,000 - 10,000 K region in the order of 10-100%. This is due to the increased complexity of calculating the doubly excited states accurately. This confirms the importance of improving the DR rates for Be-like ions in existing databases.

7.2 Future work

In the future, because of the complex environment of a neutron star merger ejecta, electron impact excitation should be considered to enable non-LTE spectra effects and magnetic field effects on atomic structure.

More detailed calculation on PI cross sections would require considering all the lowest levels in the configurations which require extensive computational resources. Also, different theoretical approaches considering cases with very large numbers of contributing excited levels could also be applied.

The DR methodology can be applied to all the ions in the Li-like, Be-like, B-like, and C-like isoelectronic sequences. This approach may help to find the suitable configurations to be considered in the DR rate calculation.

Finally, adopting various codes, for example R-matrix packages, for generating more data could result in determining the best approach for computation.

7.3 Contributions of the author

There is an existing publication associated with this work, (Taghadomi et al., 2022), and the paper on the Re isoelectronic sequence discussed in chapter 4 is ready to be published. Future publications will include

publication of the PI cross section of Tungsten ions in chapter 5 and the current available results on DR rate coefficients explained in chapter 6.

Bibliography

Abbott, B. P., Abbott, R., Abbott, T., Acernese, F., Ackley, K., Adams, C., Adams, T., Addesso, P., Adhikari, R., Adya, V., et al. (2017). Gw170817: Observation of gravitational waves from a binary neutron star inspiral. *Physical review letters*, *119*(16), 161101.

Badnell, N. (2011a). Atomic data from autostructure. url:http://http://amdpp.phys.strath.ac.uk/tamoc/DATA/DR/.

Badnell, N. (2011b). Autostructure writeup on the world wide web. url:http://amdpp.phys.strath.ac.uk/autos/ver/WRITEUP.

Badnell, N. (2011c). A breit–pauli distorted wave implementation for autostructure. *Computer Physics Communications*, *182*(7), 1528–1535.

Badnell, N., O'Mullane, M., Summers, H., Altun, Z., Bautista, M., Colgan, J., Gorczyca, T., Mitnik, D., Pindzola, M., & Zatsarinny, O. (2003). Dielectronic recombination data for dynamic finite-density plasmas-i. goals and methodology. *Astronomy & Astrophysics*, *406*(3), 1151–1165.

Ballance, C. P., & McLaughlin, B. M. (2015). Photoionization of the valence shells of the neutral tungsten atom. *Journal of Physics B: Atomic, Molecular and Optical Physics*, *48*(8), 085201.

Barnes, J., Kasen, D., Wu, M.-R., & Martinez-Pinedo, G. (2016). Radioactivity and thermalization in the ejecta of compact object mergers and their impact on kilonova light curves. *The Astrophysical Journal*, *829*(2), 110.

Berger, M., Hubbell, J., Seltzer, J., Chang, J., Coursey, R., Sukumar, D., Zucker, D., & Olsen, K. (2009). Xcom: Photon cross sections database share. *NIST Standard Reference Database 8 (XGAM)*.

Böhm, S., Müller, A., Schippers, S., Shi, W., Eklöw, N., Schuch, R., Danared, H., & Badnell, N. (2003). Experimental o vi dielectronic recombination rate coefficient and its enhancement by external electric fields. *Astronomy & Astrophysics*, *405*(3), 1157–1162.

Burgess, A. (1964). Delectronic recombination and the temperature of the solar corona. *Astrophysical Journal, vol. 139, p. 776-780*, *139*, 776–780.

Burke, P., & Taylor, K. (1975). R-matrix theory of photoionization. application to neon and argon. *Journal of Physics B: Atomic and Molecular Physics*, *8*(16), 2620.

Burke, V., & Grant, I. P. (1967). The effect of relativity on atomic wave functions. *Proceedings of the Physical Society (1958-1967)*, *90*(2), 297.

Cameron, A. G. W. (1957). Nuclear reactions in stars and nucleogenesis. *Publications of the Astronomical Society of the Pacific*, *69*(408), 201–222.

Colgan, J., Pindzola, M., & Badnell, N. (2004). Dielectronic recombination data for dynamic finite-density plasmas-v: The lithium isoelectronic sequence. *Astronomy & Astrophysics*, *417*(3), 1183–1188.

Colgan, J., Pindzola, M., Whiteford, A., & Badnell, N. (2003). Dielectronic recombination data for dynamic finite-density plasmas-iii. the beryllium isoelectronic sequence. *Astronomy & Astrophysics*, *412*(2), 597–601.

Cowan, R. D., & Griffin, D. C. (1976). Approximate relativistic corrections to atomic radial wave functions. *JOSA*, *66*(10), 1010–1014.

Dyall, K. G., & Fægri Jr, K. (2007). *Introduction to relativistic quantum chemistry*. Oxford University Press.

Eastman, R. G., & Pinto, P. A. (1993). Spectrum formation in supernovae-numerical techniques. *The Astrophysical Journal*, *412*, 731–751.

Eissner, W., Jones, M., & Nussbaumer, H. (1974). Techniques for the calculation of atomic structures and radiative data including relativistic corrections. *Computer Physics Communications*, *8*(4), 270–306.

Eissner, W., & Nussbaumer, H. (1969). A programme for calculating atomic structures. *Journal of Physics B: Atomic and Molecular Physics (1968-1987)*, *2*(10), 1028.

Fischer, C. F. (1977). Hartree–fock method for atoms. a numerical approach.

Fivet, V., Quinet, P., Palmeri, P., Biémont, É., & Xu, H. (2007). Transition probabilities and lifetimes for atoms and ions from the sixth row of the periodic table and the database desire. *Journal of electron spectroscopy and related phenomena*, *156*, 250–254.

Fogle, M., Badnell, N., Glans, P., Loch, S., Madzunkov, S., Abdel-Naby, S. A., Pindzola, M., & Schuch, R. (2005). Electron-ion recombination of be-like c, n, and o. *Astronomy & Astrophysics*, *442*(2), 757–766.

Freiburghaus, C., Rosswog, S., & Thielemann, F.-K. (1999). R-process in neutron star mergers. *The Astrophysical Journal*, *525*(2), L121.

Gillanders, J. H., McCann, M., Smartt, S. A. S., Stephen, J., & Ballance, C. P. (2021). Constraints on the presence of platinum and gold in the spectra of the kilonova at2017gfo. *arXiv preprint arXiv:2101.08271*.

Goriely, S., Bauswein, A., & Janka, H.-T. (2011). R-process nucleosynthesis in dynamically ejected matter of neutron star mergers. *The Astrophysical Journal Letters*, *738*(2), L32.

Grant, I. (1970). Relativistic calculation of atomic structures. *Advances in Physics*, *19*(82), 747–811.

Grant, I. (1974). Gauge invariance and relativistic radiative transitions. *Journal of Physics B: Atomic and Molecular Physics (1968-1987)*, *7*(12), 1458.

Grant, I., McKenzie, B., Norrington, P., Mayers, D., & Pyper, N. (1980). An atomic multiconfigurational dirac-fock package. *Computer Physics Communications*, *21*(2), 207–231.

Griem, H. R. (1963). Validity of local thermal equilibrium in plasma spectroscopy. *Physical Review*, *131*(3), 1170.

Grimmett, J., Heger, A., Karakas, A. I., & Müller, B. (2018). Nucleosynthesis in primordial hypernovae. *Monthly Notices of the Royal Astronomical Society*, *479*(1), 495–516.

Hotokezaka, K., Tanaka, M., Kato, D., & Gaigalas, G. (2022). Tungsten versus selenium as a potential source of kilonova nebular emission observed by spitzer. *Monthly Notices of the Royal Astronomical Society: Letters*, *515*(1), L89–L93.

Ichihara, A., & Eichler, J. (2000). Cross sections for radiative recombination and the photoelectric effect in the k, l, and m shells of one-electron systems with $1 \leq z \leq 112$ calculated within an exact relativistic description. *Atomic Data and Nuclear Data Tables*, *74*(1), 1–121.

Jönsson, P., Gaigalas, G., & Bieroń, J. (2013). C froese fischer and ip grant. *Comput. Phys. Commun.*, *184*, 2197.

Jönsson, P., Gaigalas, G., Bieroń, J., Fischer, C. F., & Grant, I. (2013). New version: Grasp2k relativistic atomic structure package. *Computer Physics Communications*, *184*(9), 2197–2203.

Karp, A. H., Lasher, G., Chan, K. L., & Salpeter, E. (1977). The opacity of expanding media-the effect of spectral lines. *The Astrophysical Journal*, *214*, 161–178.

Kasen, D., Badnell, N., & Barnes, J. (2013). Opacities and spectra of the r-process ejecta from neutron star mergers. *The Astrophysical Journal*, *774*(1), 25.

Kato, D., Murakami, I., Tanaka, M., Banerjee, S., Gaigalas, G., Radžiūtė, L., & Rynkun, P. (2021).

Kramida, A., Yu. Ralchenko, J. Reader, & NIST ASD Team. (2018).

Loch, S. (2022).

Mackenzie, B., Grant, I., & Norrington, P. (1980). Program to calculate transverse breit and qed corrections to energy levels in a multiconfiguration dirac-fock environment. *Comput. Phys. Commun.;(Netherlands)*, *21*(2).

Metzger, B., Martínez-Pinedo, G., Darbha, S., Quataert, E., Arcones, A., Kasen, D., Thomas, R., Nugent, P., Panov, I., & Zinner, N. (2010). Electromagnetic counterparts of compact object mergers powered by the radioactive decay of r-process nuclei. *Monthly Notices of the Royal Astronomical Society*, *406*(4), 2650–2662.

Moore, C. E. (1958). *Atomic energy levels as derived from the analyses of optical spectra* (Vol. 3). US Department of Commerce, National Bureau of Standards.

Müller, A., Schippers, S., Hellhund, J., Holste, K., Kilcoyne, A., Phaneuf, R., Ballance, C., & McLaughlin, B. (2015). Single-photon single ionization of w+ ions: Experiment and theory. *Journal of Physics B: Atomic, Molecular and Optical Physics*, *48*(23), 235203.

Nomoto, K., Tominaga, N., Umeda, H., Kobayashi, C., & Maeda, K. (2006). Nucleosynthesis yields of core-collapse supernovae and hypernovae, and galactic chemical evolution. *Nuclear Physics A*, *777*, 424–458.

Osterbrock, D. E., & Ferland, G. J. (2006). Astrophysics of gaseous nebulae and active galactic nuclei, 2nd.

Parpia, F. A., Fischer, C. F., & Grant, I. P. (1996). Grasp92: A package for large-scale relativistic atomic structure calculations. *Computer physics communications*, *94*(2-3), 249–271.

Pognan, Q., Jerkstrand, A., & Grumer, J. (2022). On the validity of steady-state for nebular phase kilonovae. *Monthly Notices of the Royal Astronomical Society*, *510*(3), 3806–3837.

Pradhan, A. K., & Nahar, S. N. (2011). *Atomic astrophysics and spectroscopy*. Cambridge University Press.

Quinet, P., Palmeri, P., Biémont, É., Jorissen, A., Van Eck, S., Svanberg, S., Xu, H., & Plez, B. (2006). Transition probabilities and lifetimes in neutral and singly ionized osmium and the solar osmium abundance. *Astronomy & Astrophysics*, *448*(3), 1207–1216.

Ryabtsev, A., Wyart, J., Joshi, Y., Raassen, A., & Uylings, P. (1993). The transitions (5d8+ 5d76s)-5d76p of pt iii. *Physica Scripta*, *47*(1), 45.

Rybicki, G. B., & Lightman, A. P. (1991). *Radiative processes in astrophysics*. John Wiley & Sons.

Shankar, R. (1994a). The dirac equation. In *Principles of quantum mechanics* (pp. 563–579). Springer.

Shankar, R. (1994b). The hydrogen atom. In *Principles of quantum mechanics* (pp. 353–371). Springer.

Shankar, R. (1994c). Systems with n degreesof freedom. In *Principles of quantum mechanics* (pp. 247–278). Springer.

Sobolev, V. (1960). Moving envelopes of stars, ed. *VV Sobolev*.

Szabo, A., & Ostlund, N. S. (2012). *Modern quantum chemistry: Introduction to advanced electronic structure theory*. Courier Corporation.

Taghadomi, Z. S., Wan, Y., Flowers, A., Stancil, P., McLaughlin, B., Bromley, S., Marler, J., Sosolik, C., & Loch, S. (2022). Relativistic atomic structure of au iv and the os isoelectronic sequence: Opacity data for kilonova ejecta. *Atoms*, *10*(3), 94.

Tanaka, M., Kato, D., Gaigalas, G., & Kawaguchi, K. (2020). Systematic opacity calculations for kilonovae. *Monthly Notices of the Royal Astronomical Society*, *496*(2), 13691392.

Tanvir, N. R., Levan, A., González-Fernández, C., Korobkin, O., Mandel, I., Rosswog, S., Hjorth, J., D'Avanzo, P., Fruchter, A., Fryer, C., et al. (2017). The emergence of a lanthanide-rich kilonova following the merger of two neutron stars. *The Astrophysical Journal Letters*, *848*(2), L27.

Thompson, A. C., Vaughan, D., et al. (2001). *X-ray data booklet* (Vol. 8). Lawrence Berkeley National Laboratory, University of California Berkeley, CA.

Trzhaskovskaya, M., Nikulin, V., & Clark, R. (2008). Radiative recombination and photoionization cross sections for heavy element impurities in plasmas. *Atomic Data and Nuclear Data Tables*, *94*(1), 71–139.

Van Kleef, T. A., & Metsch, B. (1978). Term analysis of singly ionized iridium (ir ii). *Physica B+ C*, *95*(2), 251–265.

Xu, H., Svanberg, S., Quinet, P., Palmeri, P., & Biémont, É. (2007). Improved atomic data for iridium atom (ir i) and ion (ir ii) and the solar content of iridium. *Journal of Quantitative Spectroscopy and Radiative Transfer*, *104*(1), 52–70.